



저작자표시-비영리-변경금지 2.0 대한민국

이용자는 아래의 조건을 따르는 경우에 한하여 자유롭게

- 이 저작물을 복제, 배포, 전송, 전시, 공연 및 방송할 수 있습니다.

다음과 같은 조건을 따라야 합니다:



저작자표시. 귀하는 원저작자를 표시하여야 합니다.



비영리. 귀하는 이 저작물을 영리 목적으로 이용할 수 없습니다.



변경금지. 귀하는 이 저작물을 개작, 변형 또는 가공할 수 없습니다.

- 귀하는, 이 저작물의 재이용이나 배포의 경우, 이 저작물에 적용된 이용허락조건을 명확하게 나타내어야 합니다.
- 저작권자로부터 별도의 허가를 받으면 이러한 조건들은 적용되지 않습니다.

저작권법에 따른 이용자의 권리는 위의 내용에 의하여 영향을 받지 않습니다.

이것은 [이용허락규약\(Legal Code\)](#)을 이해하기 쉽게 요약한 것입니다.

[Disclaimer](#)

공학박사 학위논문

**Selective cleavage of C-O bond in
lignin model compounds to aromatics
over palladium catalyst supported on
ordered mesoporous carbon**

정렬된 구조의 중형기공성 탄소에 담지된
팔라듐 촉매상에서 리그닌 모델화합물의
선택적인 탄소-산소 결합 분해를 통한
방향족 생산

2016년 2월

서울대학교 대학원

화학생물공학부

김 정 권

Abstract

Selective cleavage of C-O bond in lignin model compound to aromatics over palladium catalyst supported on ordered mesoporous carbon

Jeong Kwon Kim

School of Chemical and Biological Engineering

The Graduate School

Seoul National University

With increasing concerns about environmental problems and depletion of fossil fuels, lignocellulosic biomass has gained much attention as an alternative energy resources, because biomass-based sources can reduce the dependence on fossil fuels and the emission of greenhouse gases. Moreover, lignocellulosic biomass, which is based on non-food crops, does not compete with food resources. Lignocellulosic biomass normally consists of cellulose, hemicellulose, and lignin. Many studies on biomass valorization have been focused on transformation of cellulose and hemicellulose. Only 2% of lignin by-products from pulp industries is used for commercial products such as binders in asphalt, cement or polymer. Nevertheless, lignin is regarded as a promising source for sustainable production of fuels and platform chemicals, because lignin is an amorphous polymer comprising complex aromatic

structure. Various aromatic compounds in lignin are mainly linked by C-O and C-C bond such as β -O-4, α -O-4, 4-O-5, β -1, β - β , and 5-5 bonds. The amount of C-O bonds in lignin such as β -O-4 (40-60%), α -O-4 (3-5%), and 4-O-5 (4-7%) is much larger than the amount of C-C bonds in lignin such as β -1 (7-9%), β - β (2-4%), and 5-5 (19-22%). Therefore, selective cleavage of C-O bond in lignin has been considered as a key strategy for the decomposition of lignin to aromatics.

Many attempts have been made on the lignin transformation into useful chemicals such as pyrolysis and catalytic and/or enzymatic depolymerization. Among these methods, catalysis has attracted much attention as a promising process for selective conversion of lignin into value-added chemicals, because the reaction pathways can be controlled by appropriate selection of catalysts. Typical catalysts used for lignin decomposition were as follows. Acid catalysts such as mineral acid, zeolite, and cesium-exchanged heteropolyacids were well known to be efficient catalysts for cleavage of C-O bond in lignin model compounds containing β -O-4, α -O-4, and β -5 bonds. Various metal catalysts have been also investigated as catalysts for decomposition C-O bond in lignin to produce aromatics.

Due to the structural complexity of lignin, dimeric model compounds for representing C-O and C-C bonds in lignin have been studied as a lignin feedstock for depolymerization of lignin. Lignin model compounds, which possess chemical linkages similar to lignin, can provide insight into the decomposition and reaction of lignin. In particular, dimeric lignin model compounds containing C-O bonds such as α -O-4, β -O-4, and β -5 bonds are

generally used as lignin model compounds, because C-O bonds are abundant linkage type in lignin. Among various lignin model compounds, 2,3-dihydrobenzofuran, benzyl phenyl ether, and phenethyl phenyl ether has been used as a lignin model compound for representing β -5, α -O-4, and β -O-4 bond in lignin, respectively.

Porous carbon materials have been used as a catalysts support due to its thermal and mechanical stability. In particular, ordered mesoporous carbon (OMC) can be potentially available as a supporting material because of uniform pore size distribution, efficient mass transfer of reactant molecules, and controllable textural properties. In the selective cleavage of C-O bond in lignin model compounds, furthermore, carbon support can minimize the support effect due to its non-polar and hydrophobic nature. These unique properties make OMC well suited as a potential candidate material for the catalyst support.

In this work, in order to derive high aromatic productivity efficient in the catalytic decomposition of C-O bond in lignin model compounds, ordered mesoporous carbon supported palladium-based catalysts were designed, characterized, and evaluated.

First, in order to provide acid sites to support, ordered mesoporous carbon was prepared by surfactant-templating method, and subsequently, it was sulfonated with concentrated sulfuric acid at different sulfonation temperature (OMC-SO₃H-X, X= 125-225 °C). Palladium catalysts were then supported on OMC-SO₃H-X by an incipient wetness impregnation method for use in the catalytic decomposition of 2,3-dihydrobenzofuran to aromatic compounds. 2,3-Dihydrobenzofuran was used as a lignin model compound for representing β -5 bond in lignin. Sulfur content and acidity of the catalysts showed a volcano-

shaped trend with sulfonation temperature. Conversion of 2,3-dihydrobenzofuran and yield for aromatic compounds increased with increasing acidity of the Pd/OMC-SO₃H-X catalysts. Among the catalysts tested, Pd/OMC-SO₃H-150 with the largest acidity showed the highest conversion and highest yield for aromatics. It is concluded that acidity of catalysts played a crucial role in the determining the catalytic performance in the decomposition of 2,3-dihydrobenzofuran to aromatic compounds.

To enhance the acidity of the catalysts, cesium-exchanged heteropolyacid (Cs_{2.5}H_{0.5}PW₁₂O₄₀) supported on OMC with a variation of Cs_{2.5}H_{0.5}PW₁₂O₄₀ content (XC_{2.5}H_{0.5}PW₁₂O₄₀/OMC, X= 10-30 wt%). Palladium catalyst supported on XC_{2.5}H_{0.5}PW₁₂O₄₀/OMC (Pd/ XC_{2.5}H_{0.5}PW₁₂O₄₀/OMC) were then prepared by an incipient wetness impregnation method, and they were applied to the catalytic decomposition of 2,3-dihydrobenzofuran to aromatics compounds. 2,3-Dihydrobenzofuran was chosen as a lignin model compound for representing β-5 bond in lignin. Acidity of the catalysts showed a volcano-shaped trend with respect to Cs_{2.5}H_{0.5}PW₁₂O₄₀ content. Experimental result revealed that the conversion of 2,3-dihydrobenzofuran and yield for aromatic compounds increased with increasing acidity of the catalysts. Among the catalysts tested, Pd/20Cs_{2.5}H_{0.5}PW₁₂O₄₀/OMC catalyst with the largest acidity showed the highest conversion of 2,3-dihydrobenzofuran and yield for aromatic compounds. Thus, acidity of the catalysts played an important role in the determining the catalytic performance in the decomposition of 2,3-dihydrobenzofuran.

Although bifunctional catalysts, including acid catalyst showed enhanced catalytic performance for cleavage of C-O bond in lignin model

compounds, acidic properties bring about undesired reaction pathways such as Claisen rearrangement or alkylation, which lead to char formation. Noble metal catalyst, especially, palladium catalyst is well known to be an efficient catalyst for cleavage of C-O bond in lignin under mild conditions. Although Pd catalysts show considerable catalytic performance under mild conditions, their intrinsic metal properties lead to the saturated aromatic ring. Base metal catalysts such as Ni, Co, and Fe also used as catalysts in the catalytic decomposition of lignin to aromatics, because their unique properties minimize the ring saturation of aromatic ring. However, several studies have shown that base metal alone was not sufficient to obtain high yield for aromatics under mild conditions. In order to improve aromatic production by selective cleavage of C-O bond in lignin without aromatic ring-saturation, therefore, noble metal-based bimetallic catalysts have been investigated. The bimetallic systems can change the structural and electronic properties of noble metal catalysts, which induces a desired reaction pathway selectively. Therefore, in this work, Pd-based bimetallic catalysts containing Fe metal catalyst were also prepared, characterized, and evaluated selective cleavage C-O bond in lignin model compounds.

Bimetallic Pd-Fe catalyst supported on ordered mesoporous carbon (Pd-Fe/OMC) was prepared by a surfactant-templating method and a subsequent incipient wetness impregnation method. The catalyst was applied to the catalytic cleavage of C-O bond in benzyl phenyl ether to aromatics. For comparison, monometallic Pd/OMC and Fe/OMC catalysts were also investigated. Benzyl phenyl ether was used as a lignin model compound for representing α -O-4 linkage in lignin. The combined effect of palladium and iron

on the physicochemical properties and catalytic activities of Pd-Fe/OMC was investigated. Although Pd/OMC catalyst showed the highest conversion of benzyl phenyl ether, selectivity for aromatics was low due to saturation of aromatic ring. On the other hand, Fe/OMC catalyst showed lower conversion of benzyl phenyl ether than Pd/OMC, but Fe/OMC catalyst showed higher C-O bond cleavage selectivity than Pd/OMC catalyst without saturation of aromatics. Bimetallic Pd-Fe/OMC catalyst showed the highest yield for aromatics. The introduction of Fe into Pd/OMC catalyst resulted in the modification of electronic properties of Pd by electron transfer from Fe to Pd, which led to the enhanced yield for aromatics.

A series of bimetallic Pd-Fe catalysts supported on ordered mesoporous carbon ($\text{Pd}_1\text{-Fe}_x/\text{OMC}$, $X=0, 0.25, 0.7, 1.5, 4$) were characterized and evaluated in order to find optimum Fe/Pd molar ratio for maximum production of aromatics through catalytic decomposition of phenethyl phenyl ether (a model compound for representing β -O-4 bond in lignin). It was found that physicochemical properties of bimetallic catalysts were greatly affected by Fe/Pd molar ratio. In particular, interaction between Pd and Fe resulted in the modification of electronic properties of Pd by electronic transfer from Fe to Pd, which remarkably changed the hydrogen adsorption ability and bimetallic structure. In the catalytic decomposition of phenethyl phenyl ether to aromatics, hydrogen adsorption ability and bimetallic structure of the catalysts were closely related to conversion of phenethyl phenyl ether and selectivity for aromatics, respectively. Conversion of phenethyl phenyl ether decreased with increasing hydrogen adsorption ability, while maximum selectivity for aromatics was obtained when the bimetallic structure of $\text{Pd}_1\text{Fe}_{0.7}$ was formed.

Among the catalysts tested, Pd₁-Fe_{0.7}/OMC catalyst with moderate hydrogen adsorption ability and with bimetallic structure of Pd₁Fe_{0.7} composition showed the best catalytic performance in terms of yield for aromatics.

In summary, ordered mesoporous carbon supported palladium-based bifunctional and bimetallic catalysts prepared and they were applied to the catalytic cleavage of C-O bond in lignin model compounds for production of aromatics. In order to explain catalytic performance of the prepared catalyst in the catalytic decomposition of lignin, several characterization methods such as N₂ adsorption-desorption, TPR, TEM, STEM-EDX, XRD, XPS, NH₃-TPD, H₂-TPD, and XPS analyses conducted. In bifunctional catalysts, it was concluded that acidity of the catalyst played an important factors determining the catalytic performance in the decomposition of lignin model compounds. On the other hand, in bimetallic catalysts, modification of electronic properties of Pd by electron transfer from Fe to Pd, which is led to the enhanced yield for aromatics.

Keywords: Lignin, Aromatics, Selective cleavage, Palladium catalyst, Acidic support, Heteropolyacid, Bimetallic catalysts

Student Number: 2011-21024

Contents

Chapter 1. Introduction	1
1.1. Valorization of lignin	1
1.1.1. Structure of lignin and linkage.....	1
1.2. Strategy for lignin valorization	5
1.3. Catalytic cleavage of C-O bond in lignin.....	8
1.3.1. Acid catalysts.....	8
1.3.2. Transition metal catalysis.....	10
1.3.3. Ordered mesoporous carbon (OMC).....	11
1.3.4. Use of lignin model compounds	12
Chapter 2. Experimental.....	15
2.1. Preparation of catalyst.....	15
2.1.1. Synthesis of ordered mesoporous carbon.....	15
2.1.2. Preparation of sulfonated ordered mesoporous carbon.....	17
2.1.3. Preparation of palladium catalysts supported on sulfonated ordered mesoporous carbon.....	20
2.1.4. Preparation of palladium catalysts supported on cesium-exchanged heteropolyacid-impregnated ordered mesoporous carbon	22
2.1.5. Preparation of bimetallic Pd-Fe supported on ordered mesoporous carbon	25
2.1.6. Preparation of a series of bimetallic Pd-Fe supported on ordered mesoporous carbon with different Fe/Pd molar ratio	27
2.2. Characterizations.....	29
2.2.1. Physicochemical properties	29

2.2.1.	Physicochemical properties	29
2.2.2.	Crystalline structure	29
2.2.3.	Acid properties.....	30
2.2.4.	Reducibility.....	31
2.2.5.	Morphological feature.....	31
2.2.6.	Hydrogen adsorption study	31
2.2.7.	Chemical states of elements.....	32
2.3.	Catalytic decomposition of lignin model compounds	33
2.3.1.	Catalytic decomposition of 2,3-dihydrobenzofuran.....	33
2.3.2.	Selective cleavage of C-O bond in benzyl phenyl ether	36
2.3.3.	Catalytic cleavage of C-O bond in phenethyl phenyl ether	38

Chapter 3. Results and Discussion

3.1.	Characterization and catalytic activity of palladium catalyst supported on sulfonated ordered mesoporous carbon	40
3.1.1.	Formation of palladium catalyst supported on sulfonated ordered mesoporous carbon	40
3.1.2.	Acid properties of palladium catalyst supported on sulfonated ordered mesoporous carbon	45
3.1.3.	Catalytic performance in the decomposition of 2,3-dihydrobenzofuran	48
3.2.	Characterization and catalytic activity of palladium catalyst supported on cesium-exchanged heteropolyacid impregnated ordered mesoporous carbon.....	53
3.2.1.	Formation of palladium catalyst supported on cesium-exchanged heteropolyacid-impregnated ordered mesoporous carbon.....	53
3.2.2.	Acid properties of palladium catalyst supported on cesium-exchanged heteropolyacid-impregnated ordered mesoporous	

carbon.....	58
3.2.3. Catalytic performance in the decomposition of 2,3-dihydrobenzofuran	60
3.3. Characterization and catalytic activity of Pd-Fe bimetallic catalyst supported on ordered mesoporous carbon	65
3.3.1. Formation of mono-and bimetallic catalysts.....	65
3.3.2. Reduction behavior of calcined catalysts.....	73
3.3.3. Catalytic performance in the cleavage of C-O bond in benzyl phenyl ether	76
3.3.4. XPS study of reduced catalysts.....	81
3.3.5. Hydrogen adsorption ability of reduced catalysts.....	83
3.4. Characterization and catalytic activity of Pd-Fe bimetallic catalyst with a variation Fe/Pd molar ratio supported on ordered mesoporous carbon	87
3.4.1. Formation of reduced Pd ₁ -Fe _x /OMC bimetallic catalysts ..	87
3.4.2. Textural properties of reduced Pd ₁ -Fe _x /OMC bimetallic catalysts.....	90
3.4.3. Crystalline structure of reduced Pd ₁ -Fe _x /OMC bimetallic catalysts.....	93
3.4.4. Reduction behavior of calcined Pd ₁ -Fe _x /OMC bimetallic catalysts.....	96
3.4.5. Catalytic performance in the selective cleavage of C-O bond in phenethyl phenyl ether.....	99
3.4.6. Hydrogen adsorption ability of reduced catalysts.....	104
3.4.7. XPS study of reduced catalysts.....	108
Chapter 4. Conclusions	114

Bibliography..... 118

초 록..... 130

List of Tables

Table 1.1	Various linkage of native lignin, lignin model compounds, their abundance and approximate BDE values.....	4
Table 3.1	Surface area, average pore diameter, palladium dispersion, acidity, sulfur content, and catalytic performance of Pd/OMC-SO ₃ H-X (X=125, 150, 175, 200, and 225 °C) in the decomposition of 2,3-dihydrobenzofuran	52
Table 3.2	Surface area, average pore diameter, pore volume, acidity, average palladium particle size, and catalytic performance of Pd/XC _{82.5} H _{0.5} PW ₁₂ O ₄₀ /OMC in the decomposition of 2,3-dihydrobenzofuran	64
Table 3.3	Textural properties of reduced catalysts (Pd/OMC, Pd-Fe/OMC, and Fe/OMC) and ordered mesoporous carbon (OMC).....	72
Table 3.4	Catalytic performance of Pd/OMC, Pd-Fe/OMC, and Fe/OMC in the cleavage of C-O bond in benzyl phenyl ether to aromatics performed at 250 °C and 10 bar for 1 h.....	80
Table 3.5	H ₂ -TPD results of reduced catalysts.....	86
Table 3.6	Textural properties of reduced Pd ₁ -Fe _X /OMC (X= 0, 0.25, 0.7, 1.5, and 4) catalysts.....	92
Table 3.7	Catalytic performance of reduced Pd ₁ -Fe _X /OMC (X= 0, 0.25, 0.7, 1.5, and 4) catalysts in the catalytic decomposition of phenethyl phenyl ether (PPE) performed at 250 °C and 10 bar for 3 h.....	103
Table 3.8	H ₂ -TPD results of reduced Pd ₁ -Fe _X /OMC (X= 0, 0.25, 0.7, 1.5, and 4) catalysts	107
Table 3.9	XPS analyses results of reduced Pd ₁ -Fe _X /OMC (X= 0, 0.25, 0.7, 1.5, and 4) catalysts	111

List of Figures

Fig. 1.1	Schematic structure of a fragment lignocellulose	3
Fig. 1.2	Valorization process of lignocellulosic biomass	7
Fig. 1.3	Mechanism of catalytic cleavage C-O bond in lignin	13
Fig. 1.4	Representative structure of a fragment of lignin and lignin model compounds	14
Fig. 2.1	Schematic procedure for the preparation of ordered mesoporous carbon (OMC).	16
Fig. 2.2	Schematic process for sulfonation of carbon (upper) and procedure for the preparation of sulfonated ordered mesoporous carbon (OMC-SO ₃ H, lower).....	19
Fig. 2.3	The schematic procedures for the preparation of Pd/XC _{S_{2.5}H_{0.5}PW₁₂O₄₀} /OMC (X= 10, 15, 20, 25, and 30 wt%) catalysts	24
Fig. 2.4	Scheme of reaction system	35
Fig. 3.1	TEM images of Pd/OMC-SO ₃ H-X (X= 125, 150, 175, 200, and 225 °C) catalysts	42
Fig. 3.2	Nitrogen adsorption-desorption isotherms of Pd/OMC-SO ₃ H-X (X= 125, 150, 175, 200, and 225 °C) catalysts.....	43
Fig. 3.3	FT-IR spectra of Pd/OMC-SO ₃ H-X (X= 125, 150, 175, 200, and 225 °C) catalysts	44
Fig. 3.4	NH ₃ -TPD profiles of Pd/OMC-SO ₃ H-X (X= 125, 150, 175, 200, and 225 °C) catalysts	46
Fig. 3.5	Correlation between sulfur content and acidity of Pd/OMC-SO ₃ H -X catalysts	47
Fig. 3.6	Scheme for decomposition of 2,3-dihydrobenzofuran	50
Fig. 3.7	Correlation of acidity Pd/OMC-SO ₃ H-X catalysts with conversion of 2,3-dihydrobenzofuran and with total yield for aromatics at 250 °C after 1 h-reaction	51
Fig. 3.8	TEM imagea of Pd/XC _{S_{2.5}H_{0.5}PW₁₂O₄₀} /OMC (X= 10, 15, 20, 25, and 30) catalysts	55
Fig. 3.9	XRD patterns of OMC, C _{S_{2.5}H_{0.5}PW₁₂O₄₀} , and	

	Pd/XC _{S2.5} H _{0.5} PW ₁₂ O ₄₀ /OMC (X= 10, 15, 20, 25, and 30wt.%) catalysts	56
Fig. 3.10	Nitrogen adsorption-desorption isotherms of Pd/XC _{S2.5} H _{0.5} PW ₁₂ O ₄₀ /OMC (X= 10, 15, 20, 25, and 30) catalysts.	57
Fig. 3.11	NH ₃ -TPD profiles of Pd/XC _{S2.5} H _{0.5} PW ₁₂ O ₄₀ /OMC (X= 10, 15, 20, 25, and 30 wt%)	59
Fig. 3.12	Scheme for decomposition of 2,3-dihydrobenzofuran	62
Fig. 3.13	Correlation between acidity of Pd/XC _{S2.5} H _{0.5} PW ₁₂ O ₄₀ /OMC catalysts with conversion of 2,3-dihydrobenzofuran and with total yield for aromatics at 250 °C after 1 h-reaction	63
Fig. 3.14	Nitrogen adsorption-desorption isotherms of reduced catalysts (Pd/OMC, Fe/OMC, and Pd-Fe/OMC) and ordered mesoporous carbon support (OMC)	68
Fig. 3.15	XRD patterns of reduced catalysts (Pd/OMC, Fe/OMC, and Pd-Fe/OMC).....	69
Fig. 3.16	TEM images and particle size distributions of reduced catalysts (Pd/OMC, Fe/OMC, and Pd-Fe/OMC) and ordered mesoporous carbon support (OMC)	70
Fig. 3.17	STEM image ((a)) and EDX mapping images ((b), (c), and (d)) of Pd-Fe/OMC catalyst obtained by mapping on palladium and iron	71
Fig. 3.18	TPR profiles of calcined catalysts (Pd/OMC, Fe/OMC, and Pd-Fe/OMC)	75
Fig. 3.19	Reaction pathways for cleavage of α-O-4 bond in benzyl phenyl ether.....	78
Fig. 3.20	Catalytic performance of reduced catalysts (Pd/OMC, Fe/OMC, and Pd-Fe/OMC) in the selective cleavage of C-O bond in benzyl phenyl ether at 250 °C 10 bar (H ₂) after 1 h-after.....	79
Fig. 3.21	XPS spectra of (a) Pd 3d and (b) Fe 2 P _{3/2} levels in the reduced catalysts (Pd/OMC, Fe/OMC, and Pd-Fe/OMC)	82
Fig. 3.22	H ₂ -TPD profiles of reduced catalysts (Pd/OMC, Fe/OMC, and Pd-Fe/OMC) and ordered mesoporous carbon (OMC).....	85
Fig. 3.23	TEM images of reduced Pd ₁ -Fe _X /OMC (X= 0, 0.25, 0.7, 1.5, and	

	4) catalysts	88
Fig. 3.24	STEM and EDX mapping images of Pd ₁ -Fe _X /OMC (X=0.25, 0.7, and 4) catalysts.....	89
Fig. 3.25	Nitrogen adsorption-desorption isotherms of reduced Pd ₁ -Fe _X /OMC (X= 0, 0.25, 0.7, 1.5, and 4) catalysts.....	91
Fig. 3.26	XRD patterns of (a) reduced Pd ₁ -Fe _X /OMC catalysts and (b) enlarged Pd (111) diffraction peaks for Pd ₁ -Fe _X /OMC catalysts	95
Fig. 3.27	TPR profiles of calcined Pd ₁ -Fe _X /OMC (X= 0, 0.25, 0.7, 1.5, and 4) catalysts.....	98
Fig. 3.28	Reaction pathways for decomposition of phenethyl phenyl ether.....	101
Fig. 3.29	Catalytic performance of Pd ₁ -Fe _X /OMC (X= 0, 0.25, 0.7, 1.5, and 4) catalysts in the decomposition of phenethyl phenyl ether, plotted as a function of Fe/Pd molar ratio (X). Reaction conditions: temperature= 250 °C, pressure= 10 bar (H ₂), and time= 3 h... ..	102
Fig. 3.30	H ₂ -TPD profiles of reduced Pd ₁ -Fe _X /OMC (X= 0, 0.25, 0.7, 1.5, and 4) catalysts.....	106
Fig. 3.31	XPS spectra of (a) Pd 3d and (b) Fe 2P _{3/2} levels in the reduced Pd ₁ -Fe _X /OMC (X= 0, 0.25, 0.7, 1.5, and 4) catalysts.....	112
Fig. 3.32	Schemes of the proposed model for the promotion C-O group in bimetallic Pd ₁ -Fe _X /OMC (X= 0, 0.7, and 4) catalysts.....	113

Chapter 1. Introduction

1.1. Valorization of lignin

1.1.1. Structure of lignin and linkage

With increasing concerns about environmental problems and depletion of fossil fuels, lignocellulosic biomass has gained much attention as an alternative energy resource, because biofuels derived from biomass can reduce the dependence on fossil fuels and the emission of greenhouse gases [1-3]. Among the biomass resources, lignocellulosic biomass has gained growing interest as the most promising feedstock for biofuels production, because lignocellulosic biomass does not compete for land use with food crops unlike first-generation biomass resources [4-6]. Lignocellulosic biomass is typically composed of three major components such as cellulose, hemicellulose, and lignin as shown in Fig. 1.1.1 [6]. Lignin acts as an essential resin to strengthen lignocellulose matrices by filling the spaces between cellulose and hemicellulose, leading to structural integrity to plants [5,6]. As shown in Fig. 1.1, lignin is one of the richest aromatic sources in nature because lignin is a three-dimensional amorphous polymer comprising complex aromatic structure [5]. Therefore, decomposition of lignin is regarded as an advantageous technology for production of valuable chemicals.

It has been reported that only 2% of lignin by-products from pulp industries is used for commercial products such as binders in asphalt, cement or polymer [5]. Nevertheless, lignin is regarded as a promising source for sustainable

production of fuels and platform chemicals, because lignin is an amorphous polymer produced by polymerization of monomeric aromatic compounds such as coumaryl alcohol, coniferyl alcohol, and sinapyl alcohol [6]. Aromatic compounds in lignin are mainly linked by C-O and C-C bonds such as β -O-4, α -O-4, β -5, β -1, β - β , and 5-5 bonds, as presented in Table 1.1. The compositions of inner linkages in the lignin are varied with the lignocellulosic feedstocks. As presented in Table 1.1, the amount of C-O bonds in lignin such as β -O-4 (40-60%), α -O-4 (3-5%), and β -5 (6-12%) is much larger than the amount of C-C bonds in lignin such as β -1 (7-9%), β - β (2-4%), and 5-5 (19-22%) [6]. Table 1.1 also shows the approximate bond dissociation energies (BDE) in typical softwood and hard wood in lignin. As shown in Table 1.1, C-O bond containing models such as β -O-4, α -O-4, and retained more low BDE compared to those of C-C bond containing model compounds including as β -1, β - β , and 5-5. Judging from abundance and BDE results, therefore, it is concluded that selective cleavage of C-O bond in lignin is a key strategy for the decomposition of lignin to aromatics.

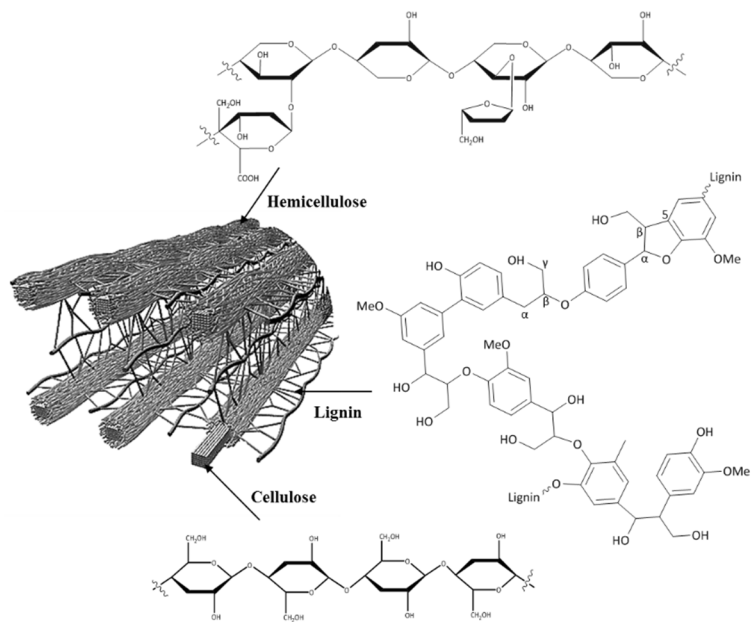
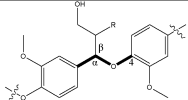
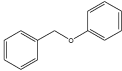
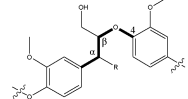
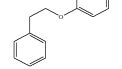
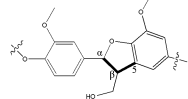
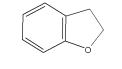
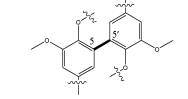
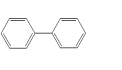
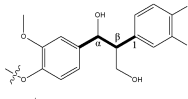
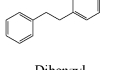
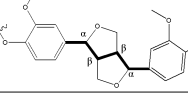
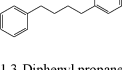


Fig. 1.1. Schematic structure of a fragment lignocellulose

Table 1.1. Various linkage of native lignin, lignin model compounds, their abundance and approximate BDE values^[6]

Linkage	Structure	Lignin model compounds	Abundance (%)			Approximate BDE (KJ mol ⁻¹)
			Spruce wood	Beech Wood	Birch Wood	
α -O-4		 Benzyl phenyl ether	11-16	28-32	6-8	215
β -O-4		 Phenethyl phenyl ether	39-50	32-37	60	290
β -5		 2,3-Dihydrobenzofuran	6-12	8	6	530
5-5		 Dibenzyl	9-11	2	4-5	490
β -1		 Dibenzyl	2	16	7	280
β - β		 1,3-Diphenyl propane	2-4	6.4	3	NA

NA: Not available

1.2. Strategy for lignin valorization

Many attempts have been made on the lignin transformation into useful chemicals such as pyrolysis and catalytic and/or enzymatic depolymerization [6-8]. Fig. 1.2.1 shows the representative strategies for lignin valorization. In the first step, lignocellulosic biomass degraded and separated into its components such as cellulose, hemicellulose, and lignin by pretreatment methods in order to open up the rigid structure [7]. Following the pretreatment, pretreated-lignin is susceptible to chemical transformation to form value-added chemicals.

As shown in Fig. 1.2, valorization strategies of lignin fall into three categories. One of the easiest ways is thermal power generation by direct combustion of lignin or after gasification [9-11]. In fact, the majority of lignin are burned as the low value fuel. Another valorization is lignin reduction method through pyrolysis or gasification [9-11]. In this method, typical reactions involved the removal of the functional groups in lignin subunits to formed less functionalities for monomeric compounds or aromatics such as benzene, toluene, or phenols. These platform chemicals are then convert to fuel applications or used bulk or fine chemicals using catalytic upgrading method [6,7]. Although thermal cracking method has several advantages including easier handling and flexibility of use of raw materials, this method showed a broad product distribution and required harsh reaction conditions. For effective valuable chemicals from decomposition of lignin, therefore, it is necessary to find an selective conversion process that can give high activity and selectivity under mild conditions. Alternatively, direct catalytic lignin depolymerization process has attracted much

attention as a promising process for valorization of lignin, because the reaction pathways can be controlled by appropriate selection of catalysts [12-14]. This strategy is best suited for the production of value-added chemical from lignin valorization with a greater degree of functionalization or convert directly to target fine chemicals.

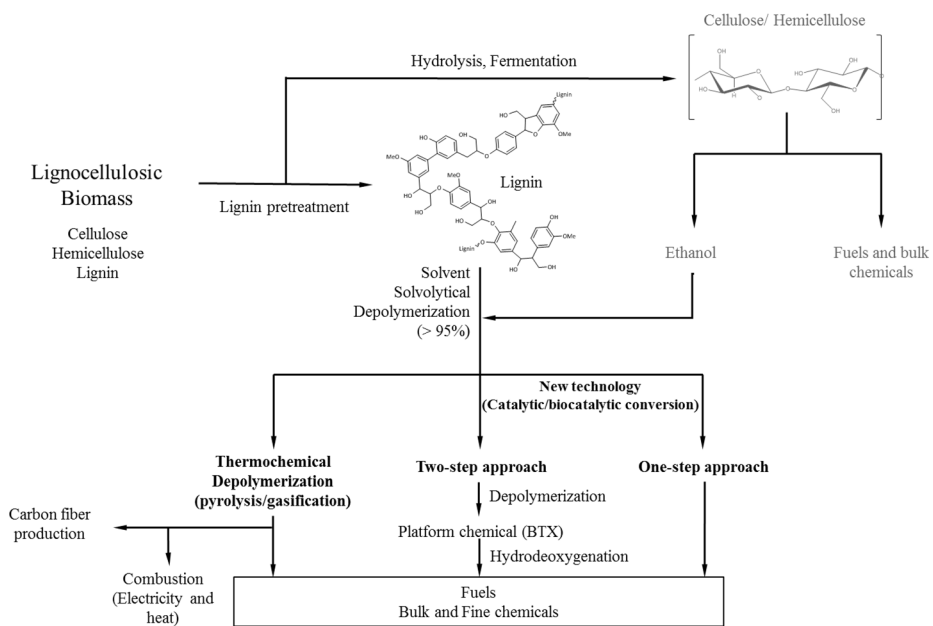


Fig. 1.2. Valorization process of lignocellulosic biomass.

1.3. Catalytic cleavage of C-O bond in lignin

1.3.1. Acid catalysts

As mentioned in previous section (section 1.2), catalysis is regarded as a key technology for valorization of lignin, because the catalytic decomposition of lignin enable selective conversion of lignin into useful chemicals. Acid catalysts such as mineral acid and heteropolyacid are known to be effective cleavage C-O bond by nucleophilic substitution reaction as shown in Fig 1.3 [15-16]. Strong acid protonates the oxygen group in aryl ether. The anion of the acid catalysts attacks the carbon in an S_N2 reaction to give the alcohol products [17,18].

Conventional mineral acids such as hydrochloric acid, sulfuric acid, and hydrofluoric acid have been widely used as acid catalysts for industrial chemical process [18]. Although these mineral acids showed considerable performance under mild conditions, these mineral acids involved many drawbacks in an environmental point of view, because their corrosive and homogeneous properties cause corrosion of reaction system and disposable problem. Therefore, heterogeneous acid catalysts have been gained much attention as recyclable, easily separable, and environmental benign catalyst that can give high catalytic activity and stable performance under mild reaction conditions.

It is well known that surface functional groups on the surface of carbon materials played an important role in sulfonating carbon material with surface modification agent [19]. Fuming method using sulfuric acid has been employed for sulfonation of carbon [20-23]. Sulfonation temperature [20], sulfonation time

[21], and sulfuric acid concentration [22-23] are important factors determining degree of sulfonation. Thus, it is expected that sulfonation of carbon materials with different acid and physicochemical properties will show a different ability in the cleavage of C-O bond in lignin model compound to aromatics.

Heteropolyacid (HPA) have attracted considerable attention as a promising acid catalyst in several homogeneous and heterogeneous reactions [24,25] including hydration of propylene [26], Friedel-Craft reaction [27], MTBE synthesis [29], and DNBE synthesis [30]. Heteropolyacids (HPAs) are inorganic acids. Acid strength of HPAs is stronger than that of conventional solid acids. HPA salts with K^+ , Cs^+ , and NH_4^+ cations have high surface area and porous structure by forming a tertiary structure. It is known that surface acidity of cation-exchanged insoluble HPAs is different depending on cation content [31,32]. For example, surface acidity of $Cs_XH_{3.0-X}PW_{12}O_{40}$ ($X=2.0-3.0$) shows a volcano-shaped trend with respect to cesium content within $X=2.0-3.0$, and shows maximum value when X is 2.5.

1.3.2. Transition metal catalysis

Noble metal catalysts such as Pt, Pd, and Rh have been also used for the selective cleavage of C-O bond lignin under mild conditions [6,33,34]. Catalytic decomposition of lignin through hydrogenation (including hydrogenolysis) on noble metal sites occurs via following steps; (1) gas phase hydrogen is dissociatively adsorbed and activated on the surface of metal sites, and (2) adsorbed hydrogen on the surface of metal sites reacts with oxygen groups of reactant or C=C bond in lignin, leading to the cleavage of C-O or C=C bond in reactant, respectively as shown in Fig 1.3. Although these catalysts showed considerable performance under mild conditions, their intrinsic metal properties lead to the saturation of aromatic rings [34-36]. Base metal catalysts such as Ni, Co, Fe are also used as catalysts in the catalytic decomposition of lignin to aromatics, because their unique properties minimize the saturation of aromatic ring [35,36]. However, several studies have shown that base metal alone was not sufficient to obtain high yield for aromatics under mild conditions [34-36].

Recently, bimetallic catalyst have attracted considerable attention because they showed different properties from the corresponding monometallic catalysts, resulting in the in the improved catalytic activity with different product distribution [38-40] For example, it has been reported that the addition of noble metals such as Ru, Rh, Pd, and Au to Ni-based catalyst improved the catalytic activity in the hydrogenolysis of lignin [39,40].

1.3.3. Ordered mesoporous carbon (OMC)

Carbon materials have been much attention as catalyst support, electrochemical storage and capacitor, water and air purification, and gas separation due to its porous nature. The use in such diverse application of porous carbons result from their superior physical and chemical properties such as high specific surface area, large pore volume, and good thermal and mechanical stability [41,42]. Porous carbon materials can be classified according to their pore diameters as microporous (pore size <2 nm), mesoporous (2-50 nm), and macropores (>50 nm). Several researches on liquid-phase catalytic reactions, the use of mesoporous carbon materials such as ordered mesoporous carbon and CMK series gave better catalytic activities than microporous activated carbon for which mass transfer limitations were operating. Therefore, ordered mesoporous carbon (OMC) can be potentially available as a supporting material because of uniform pore size distribution, efficient mass transfer of reactant molecules, and controllable textural properties [43-46]. In the selective cleavage of C-O bond in phenethyl phenyl ether, furthermore, carbon support can minimize the support effect due to its non-polar and hydrophobic nature [42]. These unique properties make OMC well suited as a potential candidate material for catalyst support.

1.3.4. Use of lignin model compounds

Fig. 1.4 shows the representative structure of a fragment of lignin and lignin model compounds. Due to the structural complexity of lignin, dimeric model compounds for representing C-O and C-C bonds in lignin have been studied as a lignin feedstock for depolymerization of lignin [6]. Lignin model compounds, which possess chemical linkages similar to lignin, can provide insight into the decomposition and reaction of lignin. In particular, dimeric lignin model compounds containing C-O bonds such as α -O-4, β -O-4, and β -5 bonds are generally used as lignin model compounds, because C-O bonds are abundant linkage type in lignin [6]. Among various lignin model compounds, benzyl phenyl ether, phenethyl phenyl ether, and 2,3-dihydrobenzofuran have been widely employed as lignin model compounds for representing α -O-4, β -O-4, and β -5 bonds in lignin, respectively.

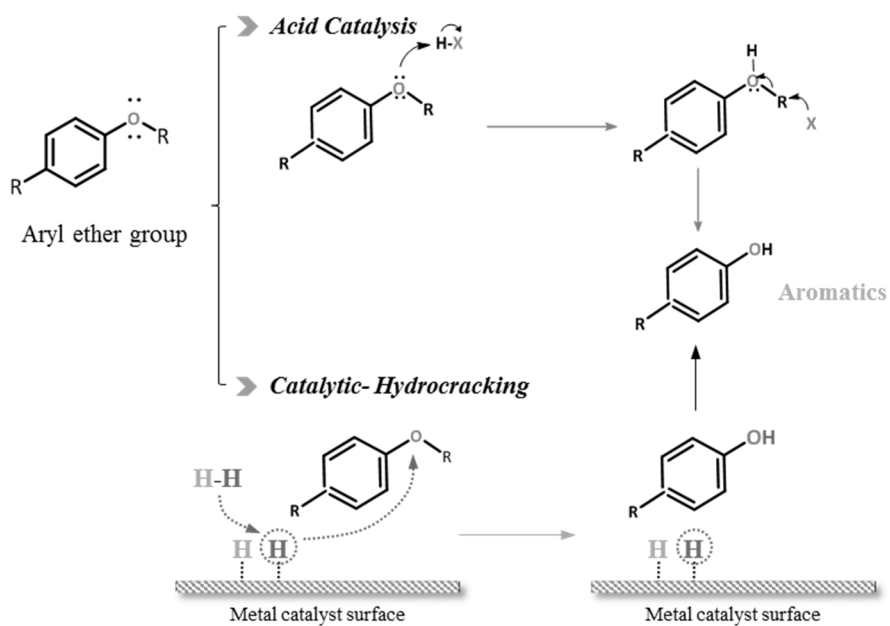


Fig. 1.3 Mechanism of catalytic cleavage C-O bond in lignin.

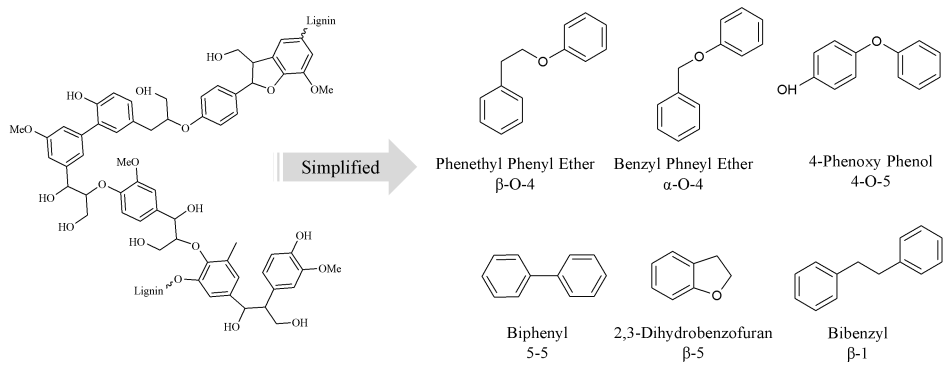


Fig. 1.4. Representative structure of a fragment of lignin and lignin model compounds.

Chapter 2. Experimental

2.1. Preparation of catalyst

2.1.1 Synthesis of ordered mesoporous carbon

The schematic procedures for the preparation of ordered mesoporous carbon (OMC) was prepared as presented in Fig. 2.1. Ordered mesoporous carbon was prepared by surfactant-templated method according to the method in literatures [45,46]. P123 (tri-block copolymer surfactant, 14.8 g, Sigma-Aldrich) was dissolved in 2M HCl solution (360 mL) at 40 °C for 6 h under stirring. After a carbon precursor (sucrose, 6.4 g, TCI) and a 5.5 mL of H₂SO₄ solution were added into the solution for stirring for 1 h. After the carbon precursor were completely dissolved, 27.3 mL of silica precursor (TEOS, 27.3 mL, Sigma-Aldrich) was slowly added into the solution. The resulting solution stirred at 40 °C for 24 h, and it was then kept at 100 °C for 24 h without stirring to induce self-assembly of micelle structure. The resultant was dried at 100 °C for 72 h, and then 160 °C for another 6 h. The color of the sample turned dark brown or nearly black. The obtained composite solid was then carbonized at 800 °C for 4 h at a heating rate of 10 °C/min in a nitrogen stream (100 mL/min). The solid product was further treated with 10 wt% HF solution for 24 h to remove the silica template, and then it was filtered and dried. The resulting ordered mesoporous carbon was denoted as OMC.

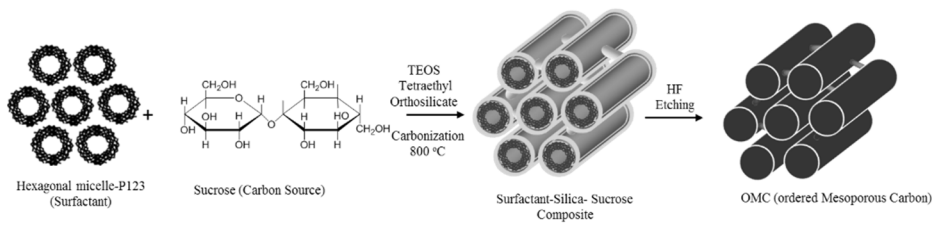


Fig. 2.1. Schematic procedure for the preparation of ordered mesoporous carbon (OMC).

2.1.2. Preparation of sulfonated ordered mesoporous carbon

Fig. 2.2 shows the schematic procedure for the preparation of sulfonated ordered mesoporous carbon. The ordered mesoporous carbon (OMC) was prepared by surfactant templating method as described in section 2.1.1. Briefly, P123 (tri-block copolymer surfactant, 14.8 g, Sigma-Aldrich) was dissolved in 2M HCl solution (360 mL) at 40 °C for 6 h under stirring. After a carbon precursor (sucrose, 6.4 g, TCI) and a 5.5 mL of H₂SO₄ solution were added into the solution for stirring for 1 h. After the carbon precursor were completely dissolved, 27.3 mL of silica precursor (TEOS, 27.3 mL, Sigma-Aldrich) was slowly added into the solution. The resulting solution stirred at 40 °C for 24 h, and it was then kept at 100 °C for 24 h without stirring to induce self-assembly of micelle structure. The resultant was dried at 100 °C for 72 h, and then 160 °C for another 6 h. The color of the sample turned dark brown or nearly black. In order to stabilize the porous structure toward the liquid-phase sulfonation treatment, the sucrose/silica composite was then heated at 600 °C for 4 h under nitrogen to obtain carbon/silica composites. Sulfonation was carried out in a Teflon-lined autoclave, where 1 g of carbon/silica composites powder was immersed in 15 ml of concentrated sulfuric acid (H₂SO₄, Sigma-Aldrich, 98%) at different sulfonation temperature (X = 125, 150, 175, 200, and 225 °C) for 15 h. The sulfonated carbon/silica composites was rigorously washed with boiling water to remove any physically adsorbed species until free of sulfate ions. The solid product was further treated with 10 wt% HF solution for 24 h to remove the silica template, and then it was filtered and dried. The template-free carbon

products, denoted as OMC-SO₃H-X (X denotes the sulfonation temperature) thus obtained was filtered, washed with deionized water and acetone, and dried.

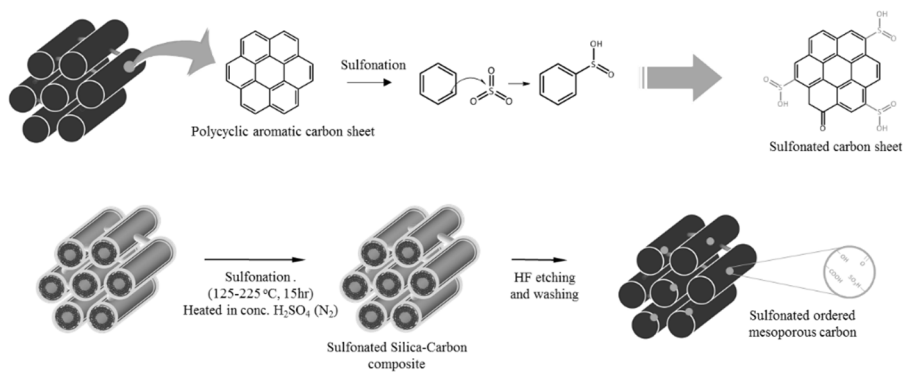


Fig. 2.2. Schematic process for sulfonation of carbon (upper) and procedure for the preparation of sulfonated ordered mesoporous carbon (OMC-SO₃H, lower).

2.1.3. Preparation of palladium catalysts supported on sulfonated ordered mesoporous carbon (Pd/OMC-SO₃H)

The schematic procedures for the preparation of ordered mesoporous carbon (OMC) was prepared as presented in Fig. 2.3. Ordered mesoporous carbon was prepared by surfactant-templated method according to the method in literatures [45,46]. P123 (tri-block copolymer surfactant, 14.8 g, Sigma-Aldrich) was dissolved in 2M HCl solution (360 mL) at 40 °C for 6 h under stirring. After a carbon precursor (sucrose, 6.4 g, TCI) and a 5.5 mL of H₂SO₄ solution were added into the solution for stirring for 1 h. After the carbon precursor were completely dissolved, 27.3 mL of silica precursor (TEOS, 27.3 mL, Sigma-Aldrich) was slowly added into the solution. The resultant solution stirred at 40 °C for 24 h, and it was then kept at 100 °C for 24 h without stirring to induce self-assembly of micelle structure. The resultant was dried at 100 °C for 72 h, and then 160 °C for another 6 h. The color of the sample turned dark brown or nearly black. The obtained composite solid was then carbonized at 800 °C for 4 h at a heating rate of 10 °C/min in a nitrogen stream (100 mL/min). The solid product was further treated with 10 wt% HF solution for 24 h to remove the silica template, and then it was filtered and dried. The resulting ordered mesoporous carbon was denoted as OMC.

Sulfonated ordered mesoporous carbon (OMC-SO₃H-X) was prepared through sulfonation of silica-carbon carbon composite at different temperature (X= 125, 150, 175, 200, and 225 °C). 1 g of silica-carbon composite and 10 mL of concentration H₂SO₄ (98%) were charged into a Teflon-lined autoclave. After

stirring the mixture at different temperature for 15 h under nitrogen stream (20 ml/min), the solid was filtered and washed with hot distilled water several times to remove physically adsorbed sulfate ions. The solid was further treated with 5 wt% HF solution to remove silica template. The resulting solid was filtered and dried to obtain OMC-SO₃H-X (X=125, 150, 175, 200, and 225 °C).

5 wt% of palladium catalyst was supported on OMC-SO₃H-X by an incipient wetness impregnation method. Palladium chloride (PdCl₂, Sigma-Aldrich) was dissolved in acetone containing 0.1 M HCl solution, and it was then introduced into the pores of OMC-SO₃H-X. The supported catalyst was dried overnight at 50 °C and calcined at 250 °C for 3 h. The supported catalyst was then reduced with a mixed stream of hydrogen (2.5 ml/min) and nitrogen (47.5 ml/min) at 250 °C for 6 h prior to the catalytic reaction. The prepared catalysts were denoted as Pd/OMC-SO₃H-X (X=125, 150, 175, 200, and 225 °C), where X represented sulfonation temperature in Celsius.

2.1.4. Palladium catalysts supported on Cs_{2.5}H_{0.5}PW₁₂O₄₀-impregnated ordered mesoporous carbon with a variation of Cs_{2.5}H_{0.5}PW₁₂O₄₀ content (Pd/XCs_{2.5}H_{0.5}PW₁₂O₄₀/OMC, X= 10, 15, 20, 25, and 30 wt%)

Ordered mesoporous carbon was prepared by surfactant-templated method according to the method. P123 (tri-block copolymer surfactant, 14.8 g, Sigma-Aldrich) was dissolved in 2M HCl solution (360 mL) at 40 °C for 6 h under stirring. After a carbon precursor (sucrose, 6.4 g, TCI) and a 5.5 mL of H₂SO₄ solution were added into the solution for stirring for 1 h. After the carbon precursor were completely dissolved, 27.3 mL of silica precursor (TEOS, 27.3 mL, Sigma-Aldrich) was slowly added into the solution. The resultant solution stirred at 40 °C for 24 h, and it was then kept at 100 °C for 24 h without stirring to induce self-assembly of micelle structure. The resultant was dried at 100 °C for 72 h, and then 160 °C for another 6 h. The color of the sample turned dark brown or nearly black. The obtained composite solid was then carbonized at 800 °C for 4 h at a heating rate of 10 °C/min in a nitrogen stream (100 mL/min). The solid product was further treated with 10 wt% HF solution for 24 h to remove the silica template, and then it was filtered and dried. The resulting ordered mesoporous carbon was denoted as OMC.

In order to provide acid sites to OMC, cesium-exchanged Cs_{2.5}H_{0.5}PW₁₂O₄₀ heteropolyacid was impregnated on OMC with a variation of Cs_{2.5}H_{0.5}PW₁₂O₄₀ content (XCs_{2.5}H_{0.5}PW₁₂O₄₀/OMC, X= 10, 15, 20, 25, and 30 wt%). A known amount of H₃PW₁₂O₄₀ (Sigma-Aldrich) was impregnated onto

0.5 g of OMC ($\text{XH}_3\text{PW}_{12}\text{O}_{40}/\text{OMC}$, X= 10, 15, 20, 25, and 30 wt%) by an incipient wetness impregnation method, and it was dried overnight at 80 °C. A known amount of cesium chloride (CsCl, Sigma-Aldrich) was dissolved in 10 ml of distilled water. 0.5 g of $\text{XH}_3\text{PW}_{12}\text{O}_{40}/\text{OMC}$ was then dispersed into the solution containing cesium chloride, and the mixture was stirred for 12 h. After filtering and washing a solid product with distilled water, the solid was dried overnight 80 °C. The solid was finally calcined at 300 °C for 3 h to obtain $\text{XC}_{\text{S}_{2.5}}\text{H}_{0.5}\text{PW}_{12}\text{O}_{40}/\text{OMC}$.

5 wt% of palladium was supported on $\text{XC}_{\text{S}_{2.5}}\text{H}_{0.5}\text{PW}_{12}\text{O}_{40}/\text{OMC}$ (X= 10, 15, 20, 25, and 30 wt%) by an incipient wetness impregnation method. Palladium chloride (PdCl_2 , Sigma-Aldrich) was dissolved in acetone containing 0.1 M HCl solution, and it was then introduced into the pores of $\text{XC}_{\text{S}_{2.5}}\text{H}_{0.5}\text{PW}_{12}\text{O}_{40}/\text{OMC}$. The supported catalyst was dried overnight at 60 °C and calcined at 300 °C for 3 h. The supported catalyst was then reduced with a mixed stream of hydrogen (2.5 ml/min) and nitrogen (47.5 ml/min) at 250 °C for 6 h prior to the catalytic reaction. The schematic procedures for the preparation of $\text{Pd}/\text{XC}_{\text{S}_{2.5}}\text{H}_{0.5}\text{PW}_{12}\text{O}_{40}/\text{OMC}$ (X= 10, 15, 20, 25, and 30 wt%) catalyst were presented in Fig. 2.2.

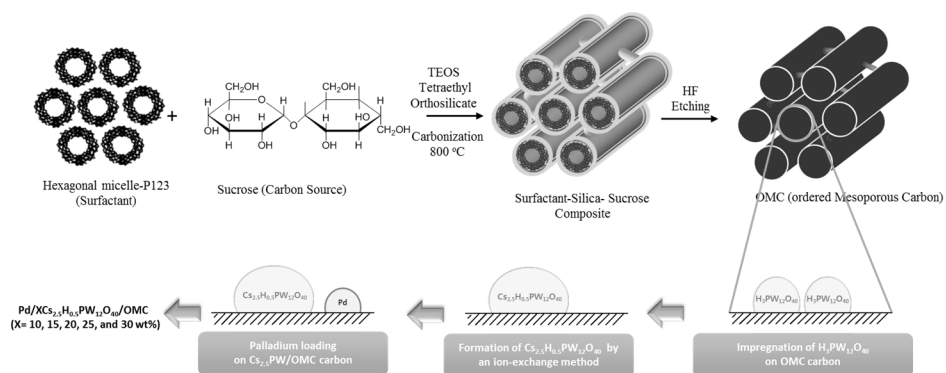


Fig. 2.3. The schematic procedures for the preparation of Pd/ $XCs_{2.5}H_{0.5}PW_{12}O_{40}$ /OMC ($X= 10, 15, 20, 25,$ and 30 wt%) catalysts.

2.1.5. Preparation of bimetallic Pd-Fe supported on ordered mesoporous carbon (Pd-Fe/OMC)

Bimetallic Pd-Fe catalyst supported on ordered mesoporous carbon (OMC) was prepared by a surfactant-templating method and a subsequent incipient wetness impregnation method (Pd-Fe/OMC). Ordered mesoporous carbon was prepared by surfactant-templated method according to the method. P123 (triblock copolymer surfactant, 14.8 g, Sigma-Aldrich) was dissolved in 2M HCl solution (360 mL) at 40 °C for 6 h under stirring. After a carbon precursor (sucrose, 6.4 g, TCI) and a 5.5 mL of H₂SO₄ solution were added into the solution for stirring for 1 h. After the carbon precursor were completely dissolved, 27.3 mL of silica precursor (TEOS, 27.3 mL, Sigma-Aldrich) was slowly added into the solution. The resulting solution stirred at 40 °C for 24 h, and it was then kept at 100 °C for 24 h without stirring to induce self-assembly of micelle structure. The resultant was dried at 100 °C for 72 h, and then 160 °C for another 6 h. The color of the sample turned dark brown or nearly black. The obtained composite solid was then carbonized at 800 °C for 4 h at a heating rate of 10 °C/min in a nitrogen stream (100 mL/min). The solid product was further treated with 10 wt% HF solution for 24 h to remove the silica template, and then it was filtered and dried. The resulting ordered mesoporous carbon was denoted as OMC.

For co-impregnation of palladium and iron metals onto OMC, palladium chloride (PdCl₂, Sigma-Aldrich) and iron nitrate (Fe(NO₃)₃, Junsei) were dissolved in acetone containing 0.1 M HCl. The precursor solution was then

introduced into the pores of OMC by an incipient wetness impregnation method. The supported catalyst was dried at 50 °C overnight and calcined at 450 °C for 3 h in a nitrogen stream. The resulting catalyst was denoted as Pd–Fe/OMC. Palladium and iron loadings in the catalyst were fixed at 5 wt%, respectively (total metal loading = 10 wt% and Pd:Fe ratio = 1:1).

For comparison, monometallic Pd and Fe catalysts supported on ordered mesoporous carbon (denoted as Pd/OMC and Fe/OMC, respectively) were also prepared by an incipient wetness impregnation method according to the similar method described above. The supported catalysts were calcined at 250 °C for Pd/OMC and at 570 °C for Fe/OMC for 3 h in a nitrogen stream. The metal loading in the monometallic catalysts was fixed at 10 wt%.

2.1.6. Preparation of a series of bimetallic Pd-Fe supported on ordered mesoporous carbon (Pd-Fe/OMC)

A series of Pd-Fe bimetallic catalysts supported on ordered mesoporous carbon were prepared by a surfactant-templating method and a subsequent incipient wetness impregnation method. Ordered mesoporous carbon was prepared according to the method reported in the literature [28]. PEO-PPO-PEO tri-block copolymer (P123, Sigma-Aldrich) was dissolved in 1.5 M HCl solution at 40 °C for 3 h. Sucrose (carbon precursor, TCI) and H₂SO₄ solution were then added into the solution for 1 h under stirring. After tetraethoxysilane (TEOS, Sigma-Aldrich) was slowly added into the solution, the resulting mixture was stirred at 40 °C for 24 h and then it was maintained at 100 °C for 20 h under static condition for self-assembly of micelle structure. The resultant was dried at 100 °C for 48 h, and it was carbonized at 800 °C for 4 h to obtain a silica-carbon composite. The silica-carbon composite was treated with 10 wt% HF solution to remove silica template, and it was finally filtered and dried. The resulting ordered mesoporous carbon was denoted as OMC.

For co-impregnation of palladium and iron metals onto OMC, palladium chloride (PdCl₂, Sigma-Aldrich) and iron nitrate (Fe(NO₃)₃, Junsei) were dissolved in acetone containing 0.1 M HCl. During this process, Pd:Fe molar ratio was adjusted to be 1:0, 0.8:0.2, 0.6:0.4, 0.4:0.6, and 0.2:0.8, while the total loading of two metals was fixed at 0.5 mol% in all samples to maintain the same number of active sites. The precursor solution was then introduced into the pores of OMC by an incipient wetness impregnation method. After drying the

impregnated catalyst at 50 °C overnight, it was calcined at 450 °C for 3 h in a nitrogen stream. The supported catalyst was then reduced with a mixed stream of hydrogen (2.5 mL/min) and nitrogen (47.5 mL/min) at 450 °C for 4 h prior to the catalytic reaction. The prepared catalysts were denoted as Pd₁-Fe_X/OMC (X= 0, 0.25, 0.7, 1.5, and 4), where X represented the Fe/Pd molar ratio.

2.2. Characterizations

2.2.1. Physicochemical properties

Chemical compositions of calcined catalyst were measured by inductively coupled plasma-atomic emission spectrometry (ICP-AES) analyses (Shimadzu, CIPS-7500).

Nitrogen adsorption-desorption measurements were conducted to investigate textural properties of the reduced catalysts using an ASAP-2010 (Micromeritics) instrument. Surface area of the reduced catalysts was measured by Brunaur-Emmett-Teller (BET) method [47]. Pore volume and average pore diameter were determined by the Barrett-Joyner-Halenda (BJH) method applied to the desorption branch of the N₂ isotherm [48]. Before the measurements, the catalysts were degassed at 120 °C for 4 h by vacuum pump for removal of moisture and other adsorbed gases on the surface of samples.

2.2.2. Crystalline structure

X-ray diffraction (XRD) analyses were performed using D-MAX-2500-PC (Rigaku) diffractometer operated at 40 kV and 100 mA to examine crystalline characteristics of reduced catalysts. Diffraction data were collected under Cu-K α radiation ($\lambda = 1.514 \text{ \AA}$) with a scan rate 10 °/min. For the XRD of reduced catalyst, each calcined catalyst was reduced with of 5% H₂ (2 mL/min) and N₂ flow (20 mL/min) at each reduction temperature for 4 h. The crystalline size can

be determined from the broadening of corresponding X-ray spectral peaks by Scherrer equation as following (2.1);

$$\tau = \frac{K\lambda}{\beta \cdot \cos\theta} \quad (2.1)$$

Where, τ is the mean crystalline size of ordered domains, K is scherrer's constant, λ is the wavelength of the X-ray radiation (Cu-K α = 1.54 Å), and β is the line width at half-maximum height, after subtraction of equipment broadening.

2.2.3. Acid properties

NH₃-TPD measurement was carried out in order to measure the acidity of the catalysts. Each catalyst (20 mg) was charged into a tubular quartz reactor of the TPD apparatus. The catalyst was preheated at 200 °C for 1 h under a flow of He (20 ml/min) to remove any physisorbed organic molecules. Ammonia (20 ml/min) was then pulsed into the reactor every minute at room temperature under a flow of He (5 ml/min), until the acid sites were saturated with ammonia. Physisorbed ammonia was removed by evacuating the catalyst sample at 100 °C for 1 h. Furnace temperature was increased from room temperature to 800 °C at a heating rate of 5 °C/min under a flow of He (10 ml/min). The desorbed ammonia was detected using a GC-MSD (Agilent, MSD-6890 N GC).

2.2.4. Reducibility

Temperature-programmed reduction (TPR) analyses of the calcined catalysts were conducted in a flow reactor system equipped with a thermal conductivity detector (TCD). 10 mg of each catalyst was reduced with a mixed stream of 5% H₂ (2 mL/min) and N₂ flow (20 mL/min) at temperatures ranging from room temperature to 700 °C with a heating rate of 10 °C/min.

2.2.5. Morphological feature

Pore structure, pore size, and particle size distribution of the catalysts were examined by HR-TEM (JEM-3100, JEOL) analyses with operate at 200 kV to examine morphological features of reduced catalysts. In order to confirm detailed dispersion of metal species, STEM analyses (JEM-2100F, JEOL) were conducted with energy dispersed X-ray spectroscopy (EDX) mapping.

For the TEM and STEM-EDX analyses of reduced catalysts, ex-situ reduction with a mixed stream of 5% H₂ (2 mL/min) and N₂ flow (20 mL/min) was preliminarily conducted before the analyses.

2.2.6. Hydrogen adsorption study

H₂ temperature-programmed desorption (H₂-TPD) analyses of the reduced catalysts were conducted using a BELCAT-B instrument (BEL Japan). 10 mg of each calcined catalyst was preliminarily reduced at 450 °C for 4 h under 5% H₂/Ar flow (50 mL/min), and then it was purged with Ar flow (50 mL/min) for

10 min. After cooling the reduced catalyst to room temperature under Ar flow (50 mL/min), 5% H₂/Ar mixed gas (50 mL/min) was injected for 60 min at 250 °C. The sample was purged under Ar flow (50 mL/min) to remove physisorbed hydrogen, and subsequently, furnace temperature was increased from room temperature to 700 °C at a heating rate of 5 °C/min under Ar flow (50 mL/min). The desorbed hydrogen was detected using a TCD (thermal conductivity detector).

2.2.6. Chemical states of elements

X-ray photoelectron spectroscopy (XPS) analyses (ThermoVG, Sigma probe) were carried out to measure binding energies of metallic palladium and iron in the reduced catalysts. For the XPS analyses, each calcined catalyst was reduced using an ex-situ reduction system at 450 °C for 4 h under 5% H₂/Ar flow (50 mL/min), and the catalyst was then transported to glass jar with sample holder in argon atmosphere glove box to minimize air exposure. After outgassing the glass jar in a vacuum oven, the sample holder was transferred to the XPS chamber as quickly as possible. All the XPS spectra were calibrated using C 1s peak (284.5 eV) as a reference.

2.3. Catalytic decomposition of lignin model compounds

2.3.1. Catalytic decomposition of 2,3-dihydrobenzofuran to aromatics

Catalytic performance of the catalysts in the decomposition of 2,3-dihydrobenzofuran was tested in a stainless steel autoclave reactor (25 ml) under nitrogen atmosphere as shown in Fig 2.4. Tetralin (Sigma-Aldrich) was used as a solvent for 2,3-dihydrobenzofuran (Sigma-Aldrich) and as a hydrogen donor in the decomposition of 2,3-dihydrobenzofuran. 50 mg of each catalyst and a mixture of 2,3-dihydrobenzofuran (1 ml), tetralin (15 ml), and hexadecane (1 ml, an internal standard) were charged into the reactor at room temperature. The reactor was purged with nitrogen several times in order to remove air. The reactor was then heated to reaction temperature (250 °C). The reaction was carried out for 1 h at nitrogen pressure of 30 bar in order to prevent vaporization of reaction mixture. After 1 h-reaction, reaction products were sampled and analyzed using a gas chromatograph (Younglin, YL6100 GC-FID) equipped with a capillary column (Agilent, DB-5MS, 60 m × 0.320 mm). Conversion of 2,3-dihydrobenzofuran and selectivity for product (phenol, ethylbenzene or 2-ethylphenol) were calculated according to the following equations on the basis of mole balance. Yield for product (phenol, ethylbenzene or 2-ethylphenol) was calculated by multiplying conversion of 2,3-dihydrobenzofuran and corresponding product selectivity.

Conversion of 2,3-dihydrobenzofuran

$$= \frac{\text{moles of 2,3 - dihydrobenzofuran reacted}}{\text{moles of 2,3 - dihydrobenzofuran supplied}}$$

(2.2)

Selectivity for aromatics (phenol, ethylbenzene or 2-ethylphenol)

$$= \frac{\text{moles of phenol, ethylbenzene or 2 - ethylphenol formed}}{\text{moles of 2,3 - dihydrobenzofuran reacted}}$$

(2.3)

Yield for aromatics

$$= (\text{Conversion of 2,3-dihydrobenzofuran}) \times (\text{Selectivity for aromatics})$$

(2.4)

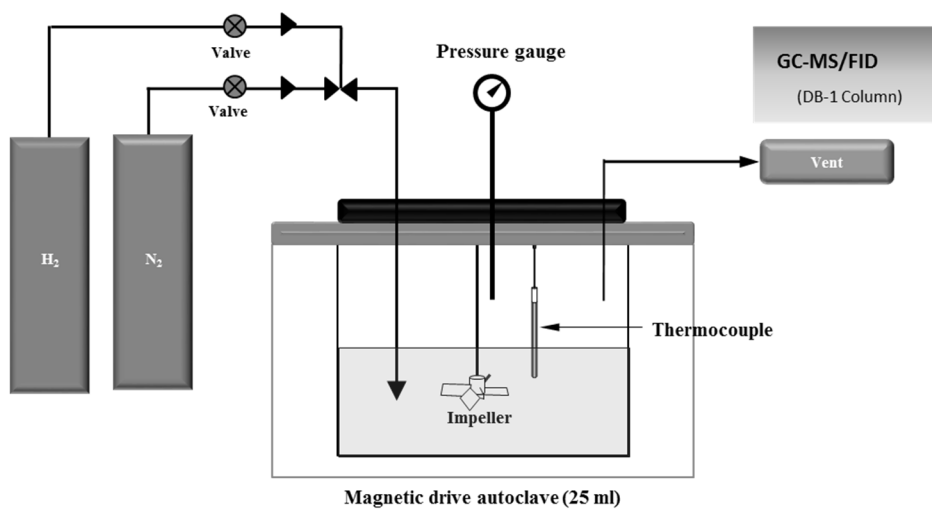


Fig. 2.4. Scheme of reaction system.

2.3.2. Selective cleavage of C-O bond in benzyl phenyl ether

Catalytic cleavage of C-O bond in benzyl phenyl ether to aromatics was carried out in a stainless steel autoclave reactor (25 ml) under hydrogen atmosphere. 9 ml of hexadecane (Sigma-Aldrich, as a solvent), 0.5 g of benzyl phenyl ether (TCI, as a reactant), and 50 mg of reduced catalyst were charged into the reactor at room temperature. The reactor was purged with nitrogen several times in order to remove air. The catalytic reaction was performed at 250 °C and 10 bar (H₂) for 1 h with agitation speed of 250 rpm. After the reaction, the reactor was cooled to room temperature and depressurized. Reaction products were analyzed with a gas chromatograph (Younglin, YL 6100 GC-FID) equipped with DB-1 column and flame ionization detector (FID). Conversion of benzyl phenyl ether and selectivity for aromatic product (toluene, phenol, or ethylbenzene) were calculated according to the following equations on the basis of mole balance. Yield for aromatic product (toluene, phenol, or ethylbenzene) was calculated by multiplying conversion of benzyl phenyl ether and corresponding product selectivity.

Conversion of benzyl phenyl ether

$$= \frac{\text{moles of benzyl phenyl ether reacted}}{\text{moles of benzyl phenyl ether supplied}}$$

(2.5)

Selectivity for aromatic product

$$= \frac{\text{moles of toluene, phenol, or ethylbenzene formed}}{\text{moles of benzyl phenyl ether reacted}} \quad (2.6)$$

Yield for aromatic product

$$= (\text{Conversion of benzyl phenyl ether}) \times (\text{Selectivity for aromatic}) \quad (2.7)$$

2.3.3. Catalytic cleavage of C-O bond in phenethyl phenyl ether

Catalytic decomposition of phenethyl phenyl ether (PPE) to aromatics was carried out in a stainless steel autoclave reactor (25 mL) under hydrogen atmosphere. 50 mg of reduced catalyst, 0.25 g of phenethyl phenyl ether (Frinton Laboratory, a reactant), and 9 mL of hexadecane (Sigma-Aldrich, a solvent) were charged into the reactor at room temperature. The reactor was purged with nitrogen several times in order to remove air. The catalytic reaction was performed at 250 °C and 10 bar (H₂) for 3 h with agitation speed of 250 rpm. After the reaction, reaction products were analyzed using a gas chromatograph (Younglin, YL6100) equipped with a DB-1 column and a flame ionization detector (FID). Conversion of phenethyl phenyl ether and selectivity for aromatic product (benzene, phenol, or ethylbenzene) were calculated according to the following equations on the basis of mole balance. Yield for aromatic product (benzene, phenol, or ethylbenzene) was calculated by multiplying conversion of phenethyl phenyl ether and corresponding product selectivity.

Conversion of phenethyl phenyl ether

$$= \frac{\text{moles of phenethyl phenyl ether reacted}}{\text{moles of phenethyl phenyl ether supplied}} \quad (2.8)$$

Selectivity for aromatic product

$$= \frac{\text{moles of benzene, phenol, or ethylbenzene formed}}{\text{moles of phenethyl phenyl ether reacted}}$$

(2.9)

Yield for aromatic product

= (Conversion of phenethyl phenyl ether) × (Selectivity for aromatic)

(2.10)

Chapter 3. Result and Discussion

3.1. Characterization and catalytic activity of palladium catalyst supported on sulfonated ordered mesoporous carbon

3.1.1. Formation of palladium catalysts supported on sulfonated ordered mesoporous carbon

Fig. 3.1 shows the HR-TEM images of Pd/OMC-SO₃H-X (X=125, 150, 175, 200, and 225 °C) catalysts. Pore structure and pore size of Pd/OMC-SO₃H-X catalysts were almost identical to those of OMC. Pd/OMC-SO₃H-X catalysts exhibited an ordered porous structure, indicating that pore structure of OMC was still maintained even after sulfonation of OMC and loading of palladium. Small particles of palladium species with an average size of ca. 4 nm were observed in the TEM images of the catalysts, indicating that palladium species were finely dispersed on the surface of OMC. Palladium dispersion of the catalysts measured by CO chemisorption is summarized in Table 3.1. Palladium dispersion of Pd/OMC-SO₃H-X catalysts was in the range of 14.8-17.3% with no great difference.

Fig. 3.2 shows the nitrogen adsorption-desorption isotherms of Pd/OMC-SO₃H-X (X=125, 150, 175, 200, and 225 °C) catalysts. All the samples showed type-IV isotherms with type-H3 hysteresis loop. This indicates that pore structure

of OMC was still maintained even after sulfonation and palladium loading, as also evidenced by HR-TEM images (Fig. 3.1). Surface area and average pore diameter of the catalysts are summarized in Table 3.1. Surface area of Pd/OMC-SO₃H-X increased with increasing sulfonation temperature. However, average pore diameter of the catalysts was almost identical, suggesting that Pd/OMC-SO₃H-X catalysts still retained pore characteristics of OMC.

Fig. 3.3 shows the FT-IR spectra of Pd/OMC-SO₃H-X (X=125, 150, 175, 200, and 225 °C) catalysts. The formation of -SO₃H group on the catalyst could be identified by IR bands appearing at 950-1400 cm⁻¹. IR bands at 1051, 1168 cm⁻¹ (asymmetry SO₂ stretching in SO₃H), and 1375 cm⁻¹ (O=S=O symmetric stretching) were clearly observed in the FT-IR spectra, indicating that -SO₃H group was formed on the surface of OMC after sulfonation of OMC [49,50]. It is interesting to note that a new band at 1750 cm⁻¹ was observed in the spectra of Pd/OMC-SO₃H-X (X= 200 and 225 °C), which corresponded to C=O stretching vibration associated with -COO- group. This was attributed to partial oxidation of carbon sheet by concentrated H₂SO₄ at high temperature, resulting in oxidation of aliphatic hydrocarbon on carbon sheet to carboxyl group [21]. IR band at 1245 cm⁻¹ and 891 cm⁻¹ was due to poly-aromatics of C-H stretching vibration associated with phenolic group [49,50].

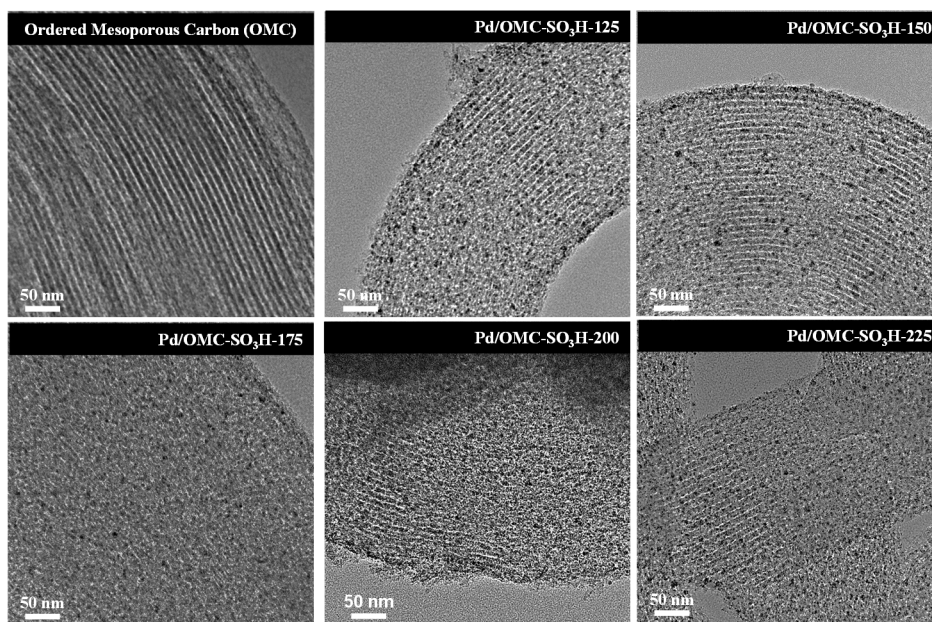


Fig. 3.1. TEM images of Pd/OMC-SO₃H-X (X= 125, 150, 175, 200, and 225 °C) catalysts.

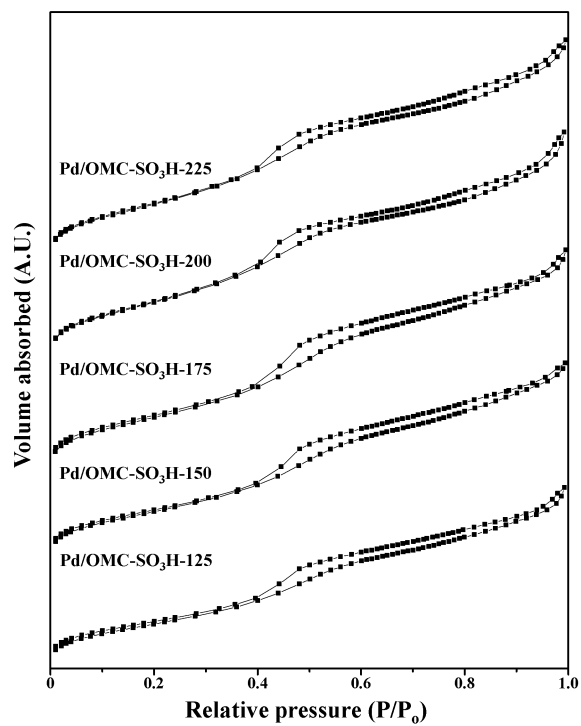


Fig. 3.2. Nitrogen adsorption-desorption isotherms of Pd/OMC-SO₃H-X (X= 125, 150, 175, 200, and 225 °C) catalysts.

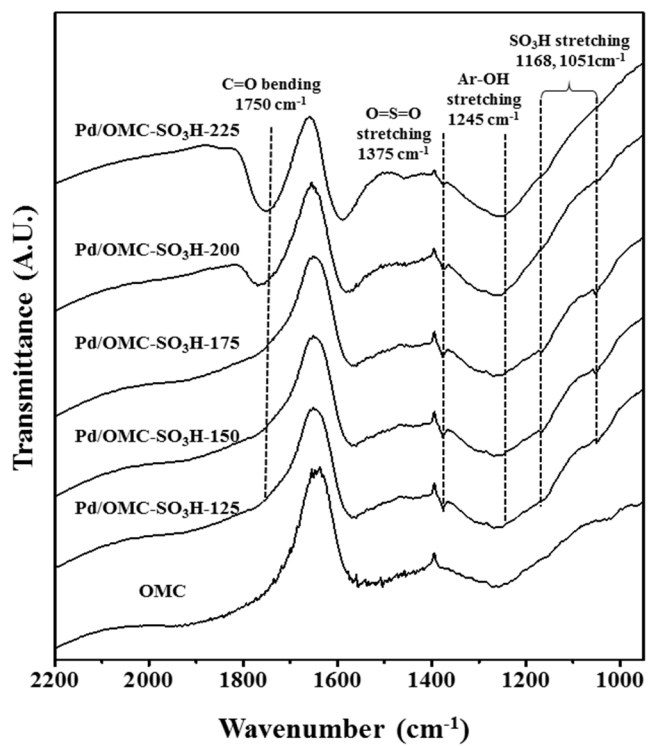


Fig. 3.3. FT-IR spectra of Pd/OMC-SO₃H-X (X= 125, 150, 175, 200, and 225 °C) catalysts.

3.1.2. Acid properties of palladium catalysts supported on sulfonated ordered mesoporous carbon

Fig. 3.4 shows the NH₃-TPD profiles of Pd/OMC-SO₃H-X catalysts. Acidity of Pd/OMC-SO₃H-X catalysts determined from NH₃-TPD peak area is summarized in Table 3.1. Interestingly, acidity of Pd/OMC-SO₃H-X showed a volcano-shaped trend with respect to sulfonation temperature within the range of 57.9-128.4 μmol-NH₃/g. Among the catalysts tested, Pd/OMC-SO₃H-150 showed the largest acidity.

CHNS analyses were conducted to determine sulfur content of Pd/OMC-SO₃H-X catalysts, as listed in Table 3.1. Sulfur content of the catalysts exhibited a volcano-shaped trend with respect to sulfonation temperature within the range of 0.14-1.16 wt%. Among the catalysts, Pd/OMC-SO₃H-150 catalysts showed the highest sulfur content.

Fig. 3.5 shows the correlation between sulfur content and acidity of Pd/OMC-SO₃H-X catalysts. The correlation showed that acidity of Pd/OMC-SO₃H-X catalysts increased with increasing sulfur content of the catalysts. Among the catalysts examined, Pd/OMC-SO₃H-150 with the highest sulfur content (1.16 wt%) showed the largest acidity (128.4 μmol-NH₃/g).

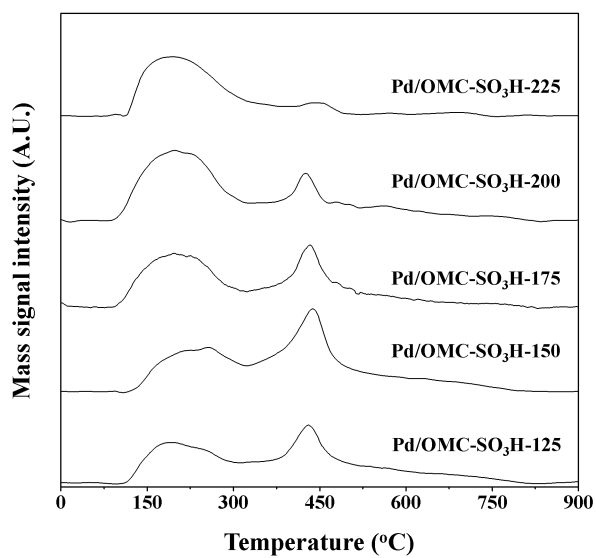


Fig. 3.4. NH₃-TPD profiles of Pd/OMC-SO₃H-X (X= 125, 150, 175, 200, and 225 °C) catalysts.

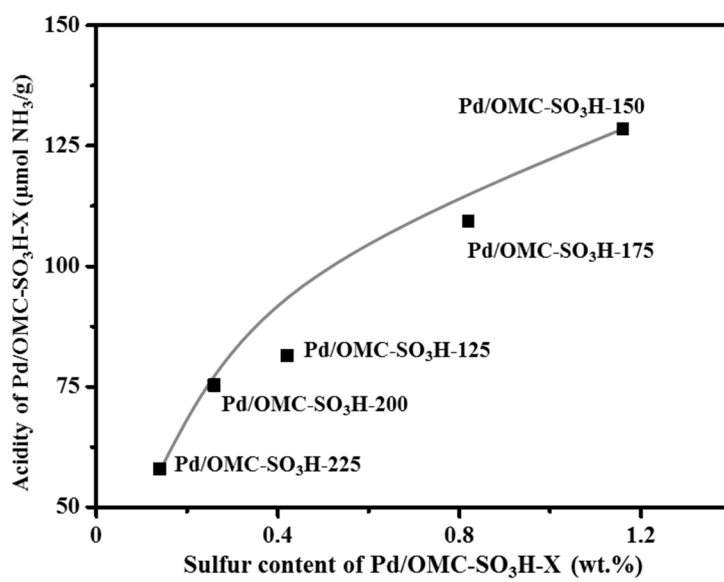


Fig. 3.5. Correlation between sulfur content and acidity of Pd/OMC-SO₃H-X catalysts.

3.1.3. Catalytic performance in the decomposition of 2,3-dihydrobenzofuran

Fig. 3.6 shows the scheme for decomposition of 2,3-dihydrobenzofuran to aromatic compounds over Pd/OMC-SO₃H-X catalysts. According to the literature [6,51,52], octahydrobenzofuran is produced by hydrogenation of 2,3-dihydrobenzofuran. Octahydrobenzofuran is then converted to ethylcyclohexanol (an intermediate), and it is further converted to ethylcyclohexane. 2-Ethylphenol is also produced by the cleavage of dihydrofuran ring in 2,3-dihydrobenzofuran. As a result of decomposition of 2,3-dihydrobenzofuran over Pd/OMC-SO₃H-X catalysts, aromatic compounds such as ethylcyclohexane and 2-ethylphenol were mainly produced. Small amounts of light hydrocarbons (C₂-C₈) and alcohols were produced as by-products in the reaction.

Catalytic performance of Pd/OMC-SO₃H-X in the decomposition of 2,3-dihydrobenzofuran performed at 250 °C and 30 bar for 1 h is listed in Table 3.1. Conversion of 2,3-dihydrobenzofuran over Pd/OMC-SO₃H-X (X=125, 150, 175, 200, and 225 °C) showed a volcano-shaped trend with respect to sulfonation temperature within the range of 45.1-56.3%. The same trend was also observed for total selectivity for aromatics (27.7-49.7%) with respect to sulfonation temperature. As a consequence, total yield for aromatics (15.1-30.1%) showed a volcano-shaped trend with respect to sulfonation temperature. Among the catalysts tested, Pd/OMC-SO₃H-150 catalyst showed the best catalytic performance in terms of conversion of 2,3-dihydrobenzofuran (56.3%), total

selectivity for aromatics (49.7%).

Fig. 3.7 shows the correlations of acidity of Pd/OMC-SO₃H-X catalysts with conversion of 2,3-dihydrobenzofuran and with total yield for aromatics at 250 °C after 1 h-reaction. Acidity and catalytic performance data were taken from Table 3.1. Conversion of 2,3-dihydrobenzofuran and total yield for aromatics increased with increasing acidity of the catalysts. Among the catalysts tested, Pd/OMC-SO₃H-150 catalyst with the largest acidity showed the highest conversion of 2,3-dihydrobenzofuran and the highest total yield for aromatics. Thus, acidity of Pd/OMC-SO₃H-X catalysts served as an important factor determining the catalytic performance in the decomposition of 2,3-dihydrobenzofuran.

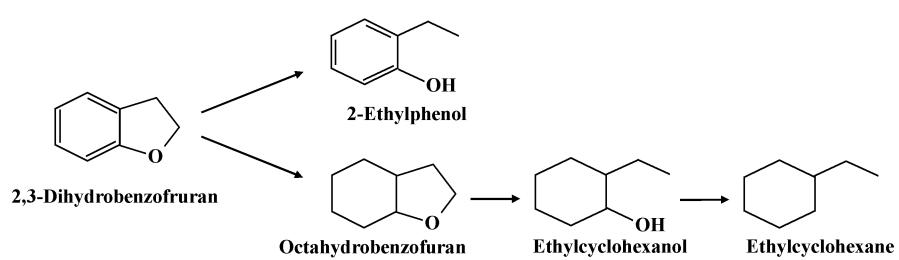


Fig. 3.6. Scheme for decomposition of 2,3-dihydrobenzofuran.

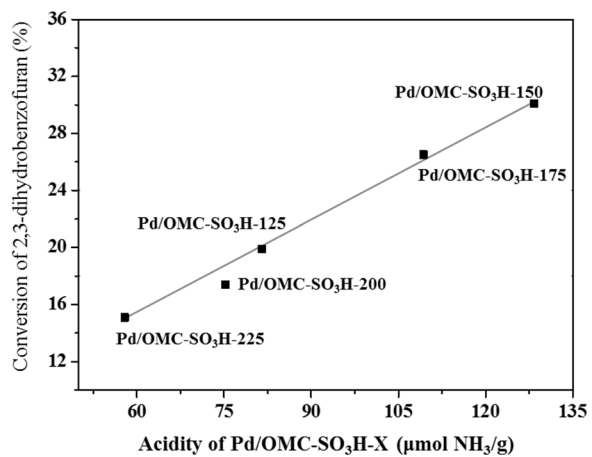
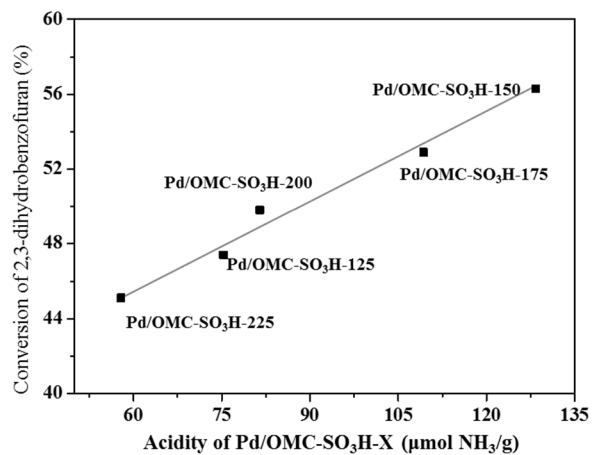


Fig. 3.7. Correlation of acidity Pd/OMC-SO₃H-X catalysts with conversion of 2,3-dihydrobenzofuran and with total yield for aromatics at 250 °C after 1 h-reaction.

Table 3.1

Surface area, average pore diameter, palladium dispersion, acidity, sulfur content, and catalytic performance of Pd/OMC-SO₃H-X (X=125, 150, 175, 200, and 225 °C) in the decomposition of 2,3-dihydrobenzofuran

	Catalyst				
	X in Pd/OMC-SO ₃ H-X				
	X=125	X=150	X=175	X=200	X=225
<i>S</i> _{BET} (m ² /g) ^a	496.9	536.1	572.0	603.7	627.7
Average pore diameter (nm) ^b	4.2	4.2	4.1	4.0	3.9
Pd dispersion (%) ^c	14.8	16.3	17.3	16.4	15.1
Acidity (μmol-NH ₃ /g) ^d	81.5	128.4	109.3	75.3	57.9
Sulfur content (wt%) ^e	0.42	1.16	0.82	0.26	0.14
Conversion of 2,3-dihydrobenzofuran(%) ^f	49.8	56.3	52.9	47.4	45.1
Total selectivity for aromatics (%) ^f	39.9	49.7	44.8	28.9	27.7
2-Ethylphenol (%)	35.3	49.7	44.8	28.9	27.7
Phenol	2.6	1.1	2.8	5.3	2.2
Ethylbenzene	1.9	2.7	2.5	2.5	3.5
Total yield for aromatics (%) ^f	19.8	30.1	26.5	17.4	15.1
2-Ethylphenol (%)	17.6	28	23.7	13.7	12.5
Phenol	1.3	0.6	1.5	2.5	1.0
Ethylbenzene	0.95	1.5	1.3	1.2	1.6

^a Calculated by BET (Barret-Joyner-Hallender) equation

^b BJH (Barret-Joyner-Hallender) desorption average pore diameter

^c Calculated by assuming CO/P_{datom}=1

^d Calculated by peak area of NH₃-TPD profile

^e Determined by CHNS analysis

^f Calculated according to the equations (2.2), (2.3), and (2.4)

3.2. Characterization and catalytic activity of palladium catalyst supported on cesium-exchanged heteropolyacid impregnated ordered mesoporous carbon with variation of $\text{Cs}_{2.5}\text{H}_{0.5}\text{PW}_{12}\text{O}_{40}$ content

3.2.1. Formation of palladium catalyst supported on cesium-exchanged heteropolyacid-impregnated ordered mesoporous carbon

Fig. 3.8 shows the TEM images of Pd/XC $\text{Cs}_{2.5}\text{H}_{0.5}\text{PW}_{12}\text{O}_{40}$ /OMC (X=10, 15, 20, 25, and 30 wt%) catalysts. Pore structure and pore size of Pd/XC $\text{Cs}_{2.5}\text{H}_{0.5}\text{PW}_{12}\text{O}_{40}$ /OMC catalysts were almost identical to those of OMC. Pd/XC $\text{Cs}_{2.5}\text{H}_{0.5}\text{PW}_{12}\text{O}_{40}$ /OMC catalysts exhibited an ordered porous structure, indicating that pore structure of OMC was still maintained even after the loading of $\text{Cs}_{2.5}\text{H}_{0.5}\text{PW}_{12}\text{O}_{40}$ and palladium. It should be noted that Pd/XC $\text{Cs}_{2.5}\text{H}_{0.5}\text{PW}_{12}\text{O}_{40}$ /OMC (X=10, 15, and 20 wt%) catalysts retained no $\text{Cs}_{2.5}\text{H}_{0.5}\text{PW}_{12}\text{O}_{40}$ agglomerates, while Pd/XC $\text{Cs}_{2.5}\text{H}_{0.5}\text{PW}_{12}\text{O}_{40}$ /OMC (X=25 and 30 wt%) catalysts showed $\text{Cs}_{2.5}\text{H}_{0.5}\text{PW}_{12}\text{O}_{40}$ agglomerates.

Fig. 3.9 shows the XRD patterns of OMC, $\text{Cs}_{2.5}\text{H}_{0.5}\text{PW}_{12}\text{O}_{40}$, and Pd/XC $\text{Cs}_{2.5}\text{H}_{0.5}\text{PW}_{12}\text{O}_{40}$ /OMC (X=10, 15, 20, 25, and 30 wt%) catalysts. OMC showed no diffraction peaks due to its amorphous nature [46]. Diffraction peaks for $\text{Cs}_{2.5}\text{H}_{0.5}\text{PW}_{12}\text{O}_{40}$ were not observed in the Pd/XC $\text{Cs}_{2.5}\text{H}_{0.5}\text{PW}_{12}\text{O}_{40}$ /OMC (X= 10, 15, and 20 wt%) catalysts due to fine dispersion of $\text{Cs}_{2.5}\text{H}_{0.5}\text{PW}_{12}\text{O}_{40}$ onto OMC. However, Pd/XC $\text{Cs}_{2.5}\text{H}_{0.5}\text{PW}_{12}\text{O}_{40}$ /OMC (X= 25 and 30 wt%) catalysts exhibited diffraction peaks for $\text{Cs}_{2.5}\text{H}_{0.5}\text{PW}_{12}\text{O}_{40}$, and peak intensities increased

with increasing $\text{Cs}_{2.5}\text{H}_{0.5}\text{PW}_{12}\text{O}_{40}$ content. These results were well consistent with TEM results of $\text{Pd}/\text{XC}_{\text{S}_{2.5}\text{H}_{0.5}\text{PW}_{12}\text{O}_{40}}/\text{OMC}$ (Fig. 3.8). Successful impregnation of palladium metal on $\text{XC}_{\text{S}_{2.5}\text{H}_{0.5}\text{PW}_{12}\text{O}_{40}}/\text{OMC}$ ($X=10-30$ wt%) was also confirmed by XRD patterns (Fig. 3.9). Average palladium particle size of the catalysts calculated by the Debye-Scherrer equation was in the range of 8.1-8.6 nm, as listed in Table 3.2.

Textural properties of OMC and $\text{Pd}/\text{XC}_{\text{S}_{2.5}\text{H}_{0.5}\text{PW}_{12}\text{O}_{40}}/\text{OMC}$ ($X=10, 20,$ and 30 wt%) catalysts were examined by nitrogen adsorption-desorption isotherm measurements as shown in Fig 3.10. All the samples showed type-IV isotherm with type-3 hysteresis loop. This indicates that pore structure of OMC was still maintained even after the loading of $\text{Cs}_{2.5}\text{H}_{0.5}\text{PW}_{12}\text{O}_{40}$ and palladium onto OMC, as also evidenced by TEM images (Fig. 3.8). Detailed textural properties of $\text{Pd}/\text{XC}_{\text{S}_{2.5}\text{H}_{0.5}\text{PW}_{12}\text{O}_{40}}/\text{OMC}$ ($X=10-30$ wt%) catalysts are summarized in Table 3.2. Surface area and pore volume of $\text{Pd}/\text{XC}_{\text{S}_{2.5}\text{H}_{0.5}\text{PW}_{12}\text{O}_{40}}/\text{OMC}$ ($X=10-30$ wt%) catalysts monotonically decreased with increasing $\text{Cs}_{2.5}\text{H}_{0.5}\text{PW}_{12}\text{O}_{40}$ content. This was attributed to formation of $\text{Cs}_{2.5}\text{H}_{0.5}\text{PW}_{12}\text{O}_{40}$ aggregates in the pore of OMC, resulting in partial blockage of OMC pore [53,54]. However, average pore diameter of $\text{Pd}/\text{XC}_{\text{S}_{2.5}\text{H}_{0.5}\text{PW}_{12}\text{O}_{40}}/\text{OMC}$ ($X=10-30$ wt%) catalysts was almost identical, suggesting that $\text{Pd}/\text{XC}_{\text{S}_{2.5}\text{H}_{0.5}\text{PW}_{12}\text{O}_{40}}/\text{OMC}$ catalysts still retained pore characteristics of OMC.

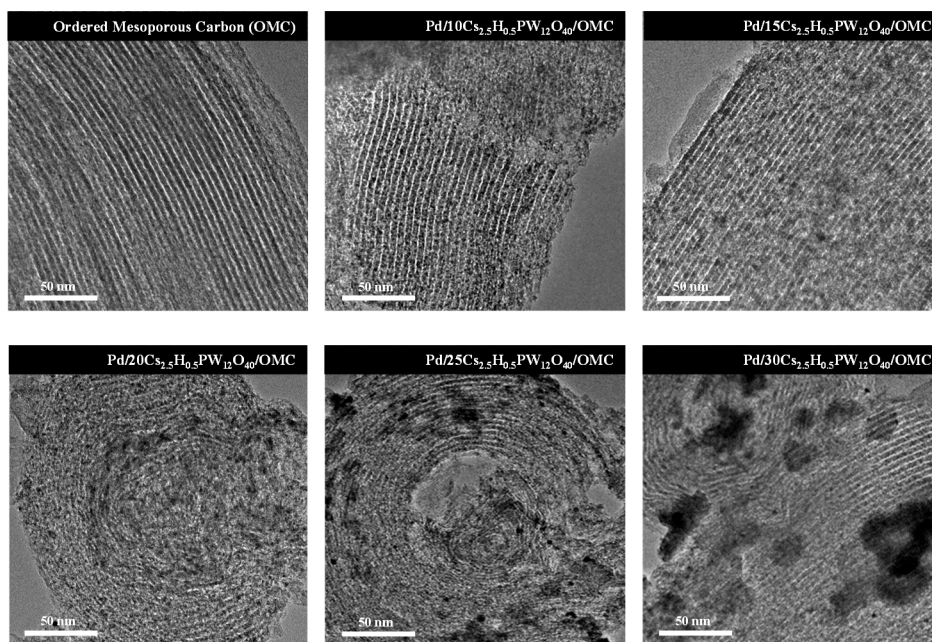


Fig. 3.8. TEM imagea of Pd/XCs_{2.5}H_{0.5}PW₁₂O₄₀/OMC (X= 10, 15, 20, 25, and 30) catalysts.

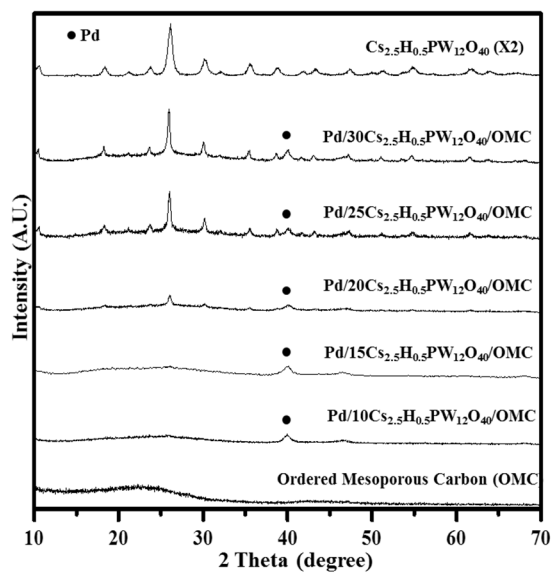


Fig. 3.9. XRD patterns of OMC, $\text{Cs}_{2.5}\text{H}_{0.5}\text{PW}_{12}\text{O}_{40}$, and $\text{Pd}/\text{XC}_{2.5}\text{H}_{0.5}\text{PW}_{12}\text{O}_{40}/\text{OMC}$ ($X= 10, 15, 20, 25,$ and $30\text{wt.}\%$) catalysts.

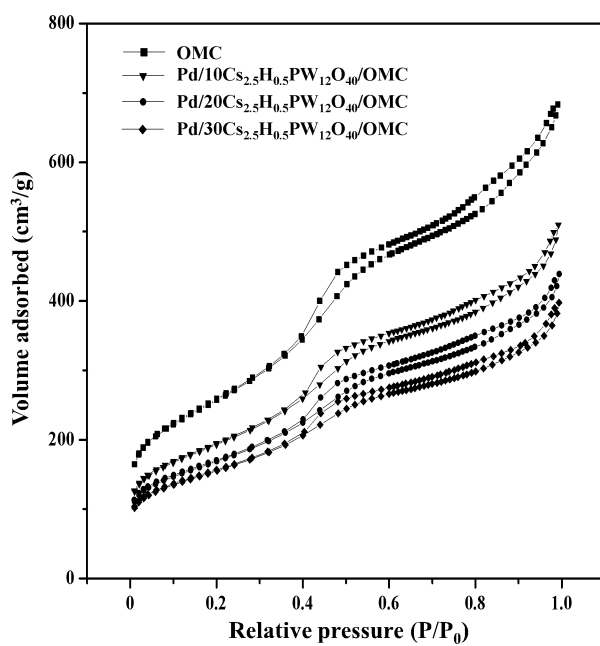


Fig. 3.10. Nitrogen adsorption-desorption isotherms of Pd/XCs_{2.5}H_{0.5}PW₁₂O₄₀/OMC (X= 10, 15, 20, 25, and 30) catalysts.

3.2.2. Acid properties of palladium catalysts supported on cesium-exchanged heteropolyacid impregnated ordered mesoporous carbon

Fig. 3.11 shows the NH_3 -TPD profiles of $\text{Pd}/\text{XC}_{\text{S}_{2.5}\text{H}_{0.5}\text{PW}_{12}\text{O}_{40}}/\text{OMC}$ catalysts. Acidity of $\text{Pd}/\text{XC}_{\text{S}_{2.5}\text{H}_{0.5}\text{PW}_{12}\text{O}_{40}}/\text{OMC}$ catalysts determined from NH_3 -TPD peak area is listed in Table 3.2. It is well known that $\text{C}_{\text{S}_{2.5}\text{H}_{0.5}\text{PW}_{12}\text{O}_{40}}$ catalyst retains only Brönsted acid site [32]. Therefore, acidity of $\text{Pd}/\text{XC}_{\text{S}_{2.5}\text{H}_{0.5}\text{PW}_{12}\text{O}_{40}}/\text{OMC}$ catalysts measured by NH_3 -TPD represents the amount of Brönsted acid sites provided by $\text{C}_{\text{S}_{2.5}\text{H}_{0.5}\text{PW}_{12}\text{O}_{40}}$. It is noteworthy that acidity of the catalysts showed a volcano-shaped trend with respect to $\text{C}_{\text{S}_{2.5}\text{H}_{0.5}\text{PW}_{12}\text{O}_{40}}$ content within the range of 158-235 $\mu\text{mol-NH}_3/\text{g}$. Among the catalysts, $\text{Pd}/20\text{C}_{\text{S}_{2.5}\text{H}_{0.5}\text{PW}_{12}\text{O}_{40}}/\text{OMC}$ showed the largest acidity due to fine dispersion of $\text{C}_{\text{S}_{2.5}\text{H}_{0.5}\text{PW}_{12}\text{O}_{40}}$ onto OMC, as evidenced by TEM (Fig. 3.8) and XRD (Fig. 3.9) results.

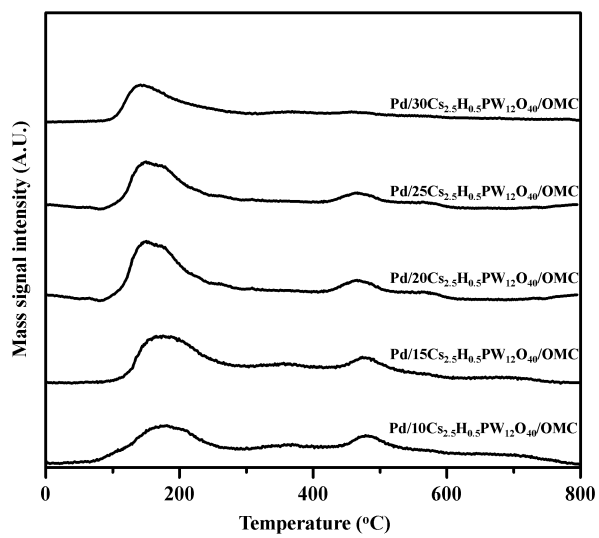


Fig. 3.11. NH₃-TPD profiles of Pd/XCs_{2.5}H_{0.5}PW₁₂O₄₀/OMC (X= 10, 15, 20, 25, and 30 wt%).

3.2.3. Catalytic performance in the decomposition of 2,3-dihydrobenzofuran

Fig. 3.12 shows the scheme for cleavage of β -5 bond in 2,3-dihydrobenzofuran. According to the literature [51,52], 2,3-dihydrobenzofuran is converted to octahydrobenzofuran through hydrogenation. Octahydrobenzofuran is then converted to ethylcyclohexanol as an intermediate, and it is further converted to ethylcyclohexane. 2-Ethylphenol is also produced by the cleavage of dihydrofuran ring in 2,3-dihydrobenzofuran [52]. In our catalytic reaction, 2-ethylphenol and ethylcyclohexane were mainly produced by the decomposition of 2,3-dihydrobenzofuran over Pd/XC_{S_{2.5}H_{0.5}PW₁₂O₄₀}/OMC. Small amounts of light hydrocarbons (C₂-C₈) and alcohols were produced as by-products in the reaction.

Catalytic performance of Pd/XC_{S_{2.5}H_{0.5}PW₁₂O₄₀}/OMC in the decomposition of 2,3-dihydrobenzofuran performed at 250 °C and 30 bar for 1 h is listed in Table 3.2. It was observed that conversion of 2,3-dihydrobenzofuran and total selectivity for aromatics over Pd/XC_{S_{2.5}H_{0.5}PW₁₂O₄₀}/OMC (X=10-30 wt%) showed volcano-shaped trends with respect to C_{S_{2.5}H_{0.5}PW₁₂O₄₀} content within the range of 69.4-87.5% and 60.7-76.9%, respectively. The same trend was also observed for total yield for aromatics (60.7-76.9%) with respect to C_{S_{2.5}H_{0.5}PW₁₂O₄₀} content. Among the catalysts tested, Pd/20C_{S_{2.5}H_{0.5}PW₁₂O₄₀}/OMC catalyst showed the best catalytic performance in terms of conversion of 2,3-dihydrobenzofuran (87.5%), total selectivity for aromatics (76.9%), and total yield for aromatics (67.3%).

Fig. 3.13 shows the correlations of acidity of Pd/XC_{S2.5}H_{0.5}PW₁₂O₄₀/OMC catalysts with conversion of 2,3-dihydrobenzofuran and with total yield for aromatics at 250 °C after 1 h-reaction. Acidity and catalytic performance data were taken from Table 1. Conversion of 2,3-dihydrobenzofuran and total yield for aromatics increased with increasing acidity of the catalysts. Among the catalysts tested, Pd/20C_{S2.5}H_{0.5}PW₁₂O₄₀/OMC catalyst with the largest acidity showed the highest conversion of 2,3-dihydrobenzofuran and the highest total yield for aromatics. Therefore, it is concluded that acidity of Pd/XC_{S2.5}H_{0.5}PW₁₂O₄₀/OMC catalysts served as an important factor determining the catalytic performance in the decomposition of 2,3-dihydrobenzofuran.

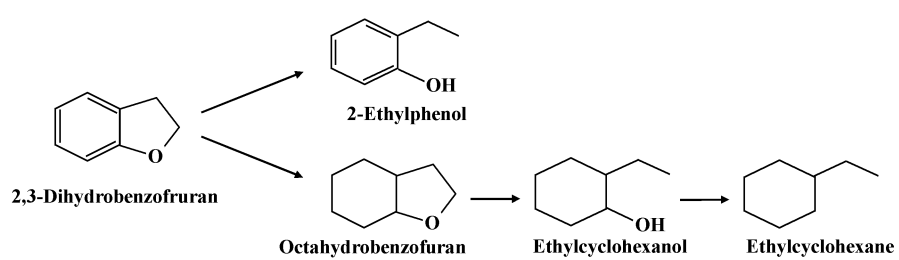


Fig. 3.12. Scheme for decomposition of 2,3-dihydrobenzofuran.

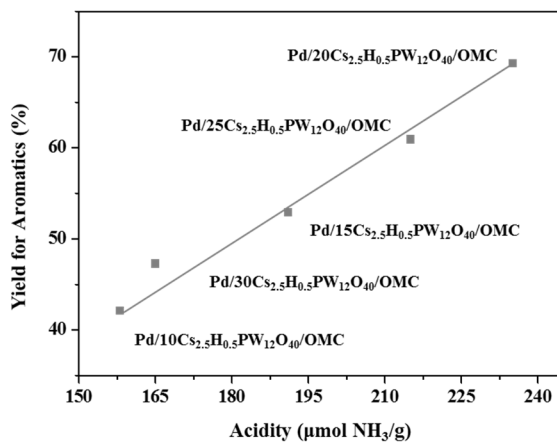
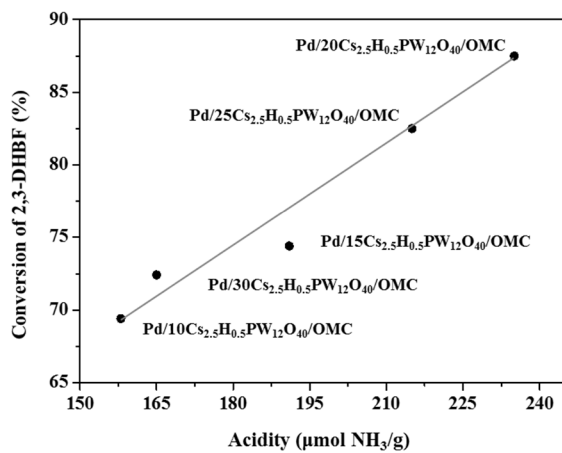


Fig. 3.13. Correlation between acidity of Pd/XCs_{2.5}H_{0.5}PW₁₂O₄₀/OMC catalysts with conversion of 2,3-dihydrobenzofuran and with total yield for aromatics at 250 °C after 1 h-reaction.

Table 3.2

Surface area, average pore diameter, pore volume, acidity, average palladium particle size, and catalytic performance of Pd/XCs_{2.5}H_{0.5}PW₁₂O₄₀/OMC in the decomposition of 2,3-dihydrobenzofuran

	Catalyst				
	Pd/XCs _{2.5} H _{0.5} PW ₁₂ O ₄₀ /OMC				
	X=10	X=15	X=20	X=25	X=30
S_{BET} (m ² /g) ^a	779.4	683.9	613.8	559.4	469.3
Average pore diameter (nm) ^b	4.2	4.1	4.1	4.2	4.0
Pore volume (cm ³ /g) ^c	0.82	0.77	0.63	0.57	0.45
Acidity (μmol-NH ₃ /g) ^d	158	191	235	215	165
Particle size of Pd ^e (nm)	8.1	8.1	8.4	8.6	8.5
Conversion of 2,3-dihydrobenzofuran(%) ^f	69.4	74.4	87.5	82.5	72.4
Total selectivity for aromatics (%) ^f	60.7	71.1	76.9	72.7	65.4
2-Ethylphenol (%)	56.5	68.3	74.5	66.9	61.5
Phenol	2.4	0.8	3.2	4.7	1.4
Ethylbenzene	1.7	2.0	1.5	2.2	2.3
Total yield for aromatics (%) ^f	42.1	52.9	67.3	60.0	47.3
2-Ethylphenol (%)	39.2	50.8	65.2	55.2	44.5
Phenol	1.7	0.6	2.8	3.9	1.0
Ethylbenzene	1.2	1.5	1.3	1.8	1.7

^a Calculated by BET (Barret-Joyner-Hallender) equation

^b BJH (Barret-Joyner-Hallender) desorption average pore diameter

^c BJH (Barret-Joyner-Hallender) desorption pore volume

^d Calculated by peak area of NH₃-TPD profile

^e Calculated by the Debye-scherrer equation

^f Calculated according to the equations (2.5), (2.6), and (2.7)

3.3. Characterization and catalytic activity of Pd-Fe bimetallic catalyst supported on ordered mesoporous carbon

3.3.1. Formation of monometallic Pd/OMC, Fe/OMC and bimetallic Pd-Fe/OMC catalysts

Textural properties of reduced catalysts (Pd/OMC, Fe/OMC, and Pd-Fe/OMC) were examined by nitrogen adsorption-desorption isotherm measurements as shown in Fig. 3.14. For comparison, isotherm of ordered mesoporous carbon support (OMC) is also presented in Fig. 3.14. All the catalysts exhibited type-IV isotherms with type-H3 hysteresis loops, indicating the existence of well-developed mesoporous structure [46,54]. Detailed textural properties of the catalysts are summarized in Table 3.3. As expected, surface area and pore volume of the catalysts were lower than those of support due to metal loading. However, average pore diameter of the catalysts was almost identical to that of support, suggesting that all the catalysts still retained unique pore characteristics of OMC. Metal loadings of the catalysts determined by ICP-AES analyses are also listed in Table 3.3. Actual palladium and iron loadings in the catalysts were in good agreement with the designed values.

Crystalline structures of reduced catalysts (Pd/OMC, Pd-Fe/OMC, and Fe/OMC) were examined by XRD measurements as shown in Fig. 3.15. All the reduced catalysts showed the characteristic diffraction peak at $2\theta = 23.5^\circ$, which was attributed to graphitic nature of carbon support (Fig. 3.15 (a)) [56-57]. The reduced Pd/OMC catalyst showed diffraction peaks at 40.1° , 46.6° , and 68.3°

corresponding to metallic palladium (Fig. 3.15 (a)) [57]. Similarly, the reduced Fe/OMC catalyst showed diffraction peaks at 43.8° and 65.1° , corresponding to metallic iron (Fig. 3.15 (a)) [58,59]. The bimetallic Pd-Fe/OMC catalyst showed the combined diffraction peaks of monometallic catalysts (Pd/OMC and Fe/OMC). Interestingly, a close examination reveals that the characteristic diffraction peak for palladium in the Pd-Fe/OMC catalyst slightly shifted to higher angle compared to that in the Pd/OMC catalyst (Fig 3.15 (b)). This is because iron atoms were partially incorporated into the lattice of palladium to form a Pd-Fe miscible phase; the rest of iron was presented as metallic iron (Fig. 3.15 (c)) [59-61]. In order to examine the dispersion of palladium and iron supported on ordered mesoporous carbon, particle sizes of palladium and iron were calculated from XRD as listed in Table 3.3. Average particle sizes of Pd in the Pd/OMC and Pd-Fe/OMC catalysts were 8.8 nm and 12.4 nm, respectively. On the other hand, average particle sizes of Fe in the Pd-Fe/OMC and Fe/OMC catalysts were 23.9 nm and 26.5 nm, respectively.

Fig. 3.16 shows the HR-TEM images and particle size distributions of reduced catalysts (Pd/OMC, Pd-Fe/OMC, and Fe/OMC) and carbon support (OMC). All the catalysts exhibited an ordered porous structure with large pores in the range of 4-6 nm, indicating that pore structure of OMC was still maintained even after the loading of palladium and iron. Pd/OMC catalyst showed a narrow particle size distribution with an average diameter of ca. 8 nm, indicating that Pd metal particles were uniformly distributed. On the other hand, Fe particles in the Fe/OMC catalyst showed a broad particle size distribution; small particles in the range of 5-10 nm and large particles in the range of 20-30 nm were observed.

Similar to Fe/OMC catalyst, Pd-Fe/OMC catalyst also showed a broad distribution of particle size; small particles in the range of 4-8 nm and large particles in the range of 20-30 nm were observed. This result was well consistent with metal particle size determined by XRD analyses (Fig. 3.15). However, it was difficult to identify each metal component in the bimetallic Pd-Fe/OMC catalyst by TEM image.

In order to confirm the dispersion of metallic Pd and Fe in the Pd-Fe/OMC catalyst, STEM-EDX analyses were conducted. Fig. 3.17 shows the STEM image (Fig. 3.17 (a)) and EDX mapping images (Fig. 3.17 (b), (c), and (d)) of Pd-Fe/OMC catalyst. Metallic palladium and iron were indistinguishable in the STEM image (Fig. 3.17 (a)). On the other hand, a homogeneous distribution of Pd (red dot) and Fe (green dot) elements was clearly observed in the EDX mapping image (Fig. 3.17 (b)). Interestingly, a portion of Fe species was well dispersed on the surface of OMC support, while some Fe species interacted with Pd domain (Fig. 3.17 (c) and (d)). On the basis of XRD and EDX mapping results, it is believed that a Pd-Fe miscible phase was formed in the bimetallic Pd-Fe/OMC catalyst, which was responsible for strong interaction between palladium and iron species.

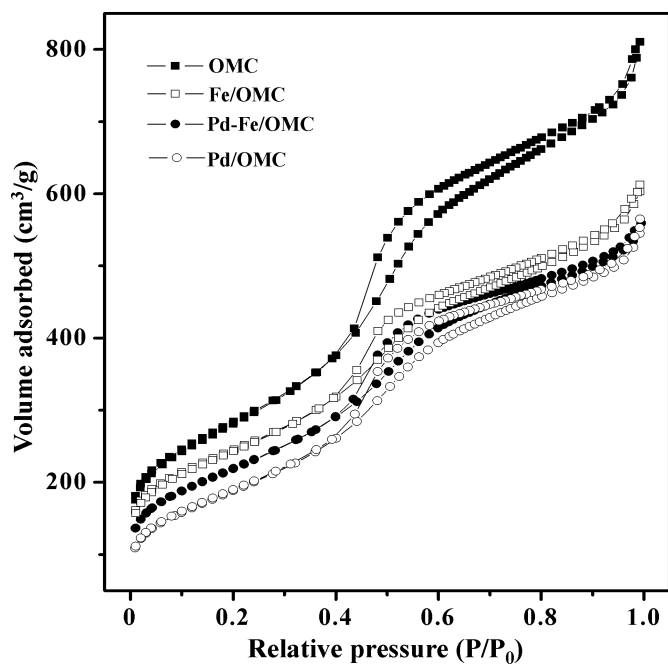


Fig. 3.14. Nitrogen adsorption-desorption isotherms of reduced catalysts (Pd/OMC, Fe/OMC, and Pd-Fe/OMC) and ordered mesoporous carbon support (OMC).

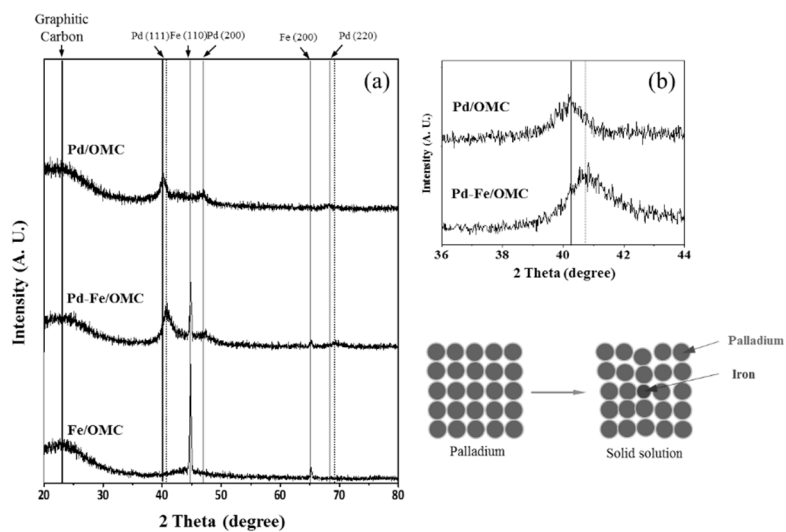


Fig. 3.15. XRD patterns of reduced catalysts (Pd/OMC, Fe/OMC, and Pd-Fe/OMC)

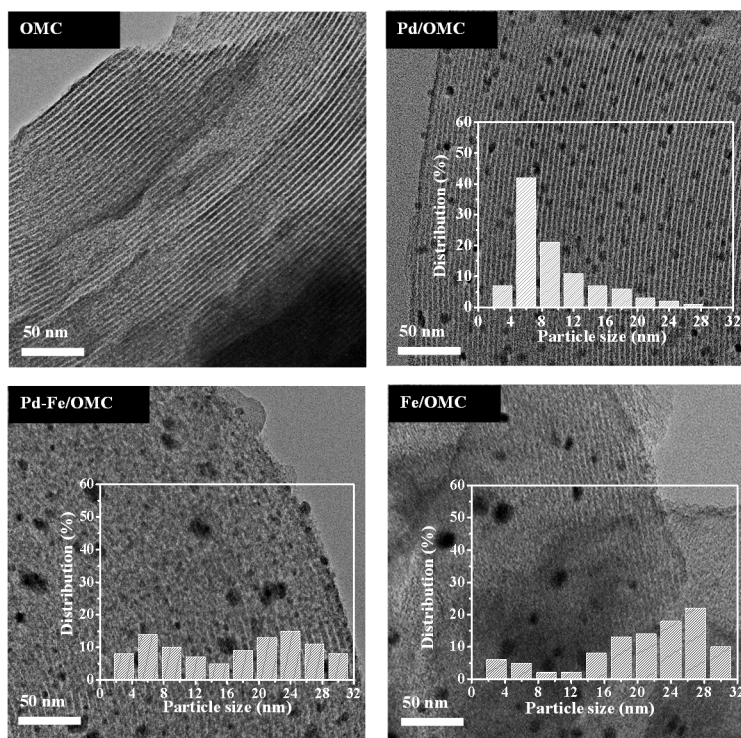


Fig. 3.16. TEM images and particle size distributions of reduced catalysts (Pd/OMC, Fe/OMC, and Pd-Fe/OMC) and ordered mesoporous carbon support (OMC)

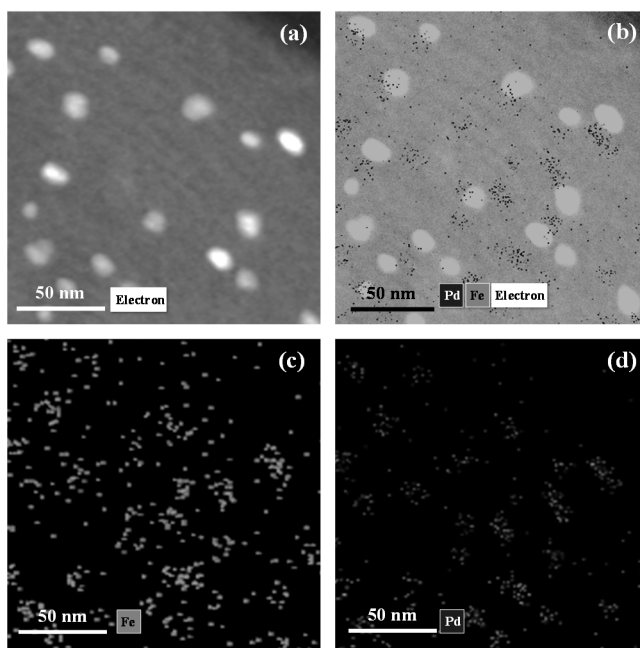


Fig. 3.17. STEM image ((a)) and EDX mapping images ((b), (c), and (d)) of Pd-Fe/OMC catalyst obtained by mapping on palladium and iron.

Table 3.3

Textural properties of reduced catalysts (Pd/OMC, Pd-Fe/OMC, and Fe/OMC) and ordered mesoporous carbon (OMC)

Sample	Metal	Surface area (m ² /g) ^b	Pore volume (cm ³ /g) ^c	Pore diameter (nm) ^d	Average	
	content				particle size	
	(wt%) ^a				(nm) ^e	
	Pd : Fe				Pd	Fe
OMC	-	1150.29	1.28	4.01	-	-
Pd/OMC	9.8 : 0	732.14	0.88	3.93	7.8	-
Pd-Fe/OMC	4.9 : 4.5	778.08	0.91	3.99	12.4	23.9
Fe/OMC	0 : 9.5	784.27	0.89	3.94	-	26.5

^a Determined by ICP-AES measurement

^b Calculated by BET (Brunauer-Emmett-Teller) equation

^c BJH (Barrett-Joyner-Hallender) desorption average pore diameter

^d Average pore diameter

^e Calculated by Debye-Scherrer equation

3.3.2. Reduction behavior of calcined catalysts

TPR measurements were carried out to investigate the reduction behavior of Pd/OMC, Pd-Fe/OMC, and Fe/OMC catalysts as shown in Fig. 3.18. TPR profile of Pd/OMC catalyst showed a negative peak at 60 °C and two positive peaks at 172 °C and 591 °C. The negative peak at 60 °C was related to hydrogen release attributed to the decomposition of palladium hydride (PdH_x) [62]. The peaks at 172 °C was attributed to the reduction of PdO to metallic Pd, while the peak at 591 °C was due to the gasification of carbon support [62,63]. On the other hand, TPR profiles of Fe/OMC and Pd-Fe/OMC catalysts showed broad reduction peaks. For precise investigation, TPR profiles of Fe/OMC and Pd-Fe/OMC catalysts were deconvoluted in terms of hydrogen consumption temperature. As shown in Fig. 3.18, Fe/OMC catalyst showed three deconvoluted reduction peaks. The reduction peak at 335 °C was attributed to the reduction of Fe_2O_3 to metallic Fe_3O_4 [45,64]. The reduction peak at 496 °C was due to the reduction of Fe_3O_4 to FeO, whereas the peak at 561 °C was associated with the reduction of FeO to metallic Fe [43,64]. The bimetallic Pd-Fe/OMC catalyst exhibited three reduction peaks at different temperature window compared to Fe/OMC catalyst. It is well known that the interaction between two metal species can affect the reducibility of the other metal [65]. In the aspect of Pd atoms in the Pd-Fe/OMC catalyst, the introduction of iron atoms inhibits the reduction of palladium metal oxide due to close interaction between palladium and iron. Thus, TPR profile of Pd-Fe/OMC catalyst shifts to higher temperature with broadness compared to that of Pd/OMC catalyst. On the other hand, bimetallic catalyst

containing noble metal enables facile reduction of other transition metal oxide due to hydrogen transfer from their reduced species [45,66]. In the aspect of Fe atoms, therefore, the presence of Pd in the bimetallic Pd-Fe/OMC catalyst increases reducibility of Fe species [67]. Thus, it can be inferred that activated hydrogen on the reduced Pd surface was transferred to Fe surface during the reduction process, promoting its reduction at low temperature. It is noteworthy that hydrogen desorption peak associated with palladium hydride (PdH_x) disappeared in the Pd-Fe/OMC catalyst, suggesting that the formation of palladium hydride was inhibited by the addition of Fe. This might be because the strong interaction between Pd and Fe formed a bimetallic phase throughout the catalyst surface, as reported in the literatures [45,60,61]. From this result, it is inferred that the interaction between Pd and Fe changed the reducibility of both metal species in the Pd-Fe/OMC catalyst, which might strongly affect the catalytic behavior.

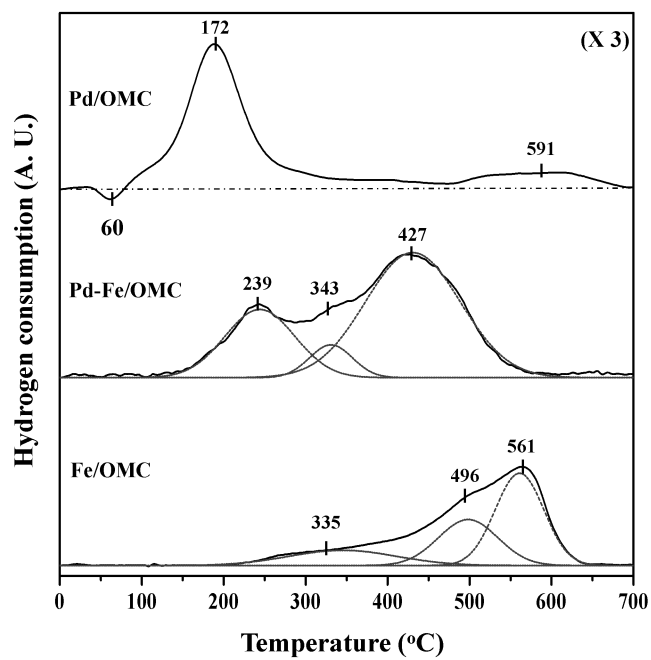


Fig. 3.18. TPR profiles of calcined catalysts (Pd/OMC, Fe/OMC, and Pd-Fe/OMC).

3.3.3. Catalytic performance in the cleavage of C-O bond in benzyl phenyl ether

Fig. 3.19 shows the reaction pathways for decomposition of benzyl phenyl ether. According to the literatures [6,68], catalytic decomposition of benzyl phenyl ether follows consecutive reaction pathways. Aromatic compounds are formed by the cleavage of C-O bond in benzyl phenyl ether. These aromatic compounds are further converted to the aromatic ring-saturated products by hydrogenation of aromatic ring. As shown in Fig. 3.19, aromatic compounds such as toluene, phenol, and ethylbenzene were mainly produced by the cleavage of C-O bond in benzyl phenyl ether. Aromatic ring-saturated products such as methylcyclohexane and ethylcyclohexane were also produced by the hydrogenation of aromatic ring. In our catalytic reaction, benzylphenol, light hydrocarbons (C₁-C₃), and alcohols were produced as by-products.

Catalytic performance of Pd/OMC, Pd-Fe/OMC, and Fe/OMC in the cleavage of C-O bond in benzyl phenyl ether to aromatics performed at 250 oC and 10 bar for 1 h is shown in Fig. 3.20 and listed in Table 3.4. Pd/OMC catalyst showed the highest conversion of benzyl phenyl ether (93.0%) and the highest selectivity for aromatic ring-saturated products (47.1%) such as methylcyclohexane and ethylcyclohexane. On the other hand, both Fe/OMC and Pd-Fe/OMC catalysts showed very low activity toward hydrogenation of aromatic ring in the reaction. Selectivity for aromatics over both catalysts (Pd-Fe/OMC and Fe/OMC) was higher than 70%, while conversion of benzyl phenyl ether over Pd-Fe/OMC catalyst (88.5%) was much higher than that over Fe/OMC

catalyst (50.1%). As a consequence, yield for aromatics increased in the order of Pd/OMC (36.2%) < Fe/OMC (37.2%) < Pd-Fe/OMC (74.3%). The above results indicate that the bimetallic Pd-Fe/OMC catalyst was more efficient in the selective cleavage of C-O bond in benzyl phenyl ether to aromatics than the monometallic catalysts (Pd/OMC and Fe/OMC).

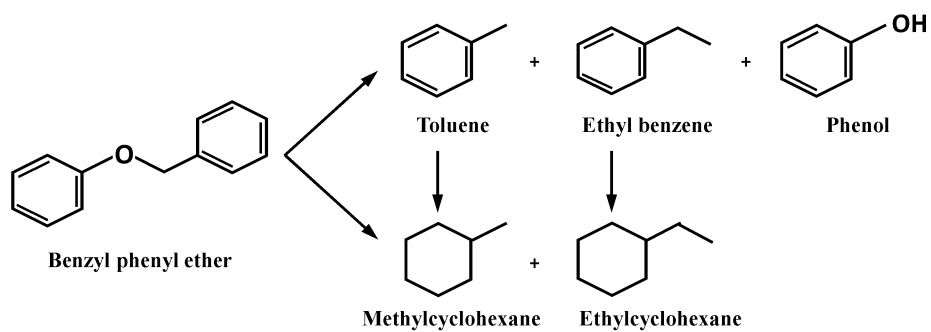


Fig. 3.19. Reaction pathways for cleavage of α -O-4 bond in benzyl phenyl ether.

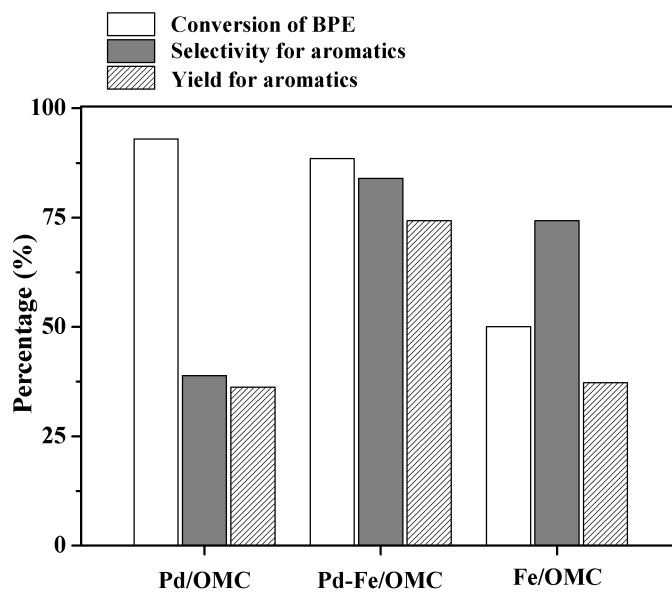


Fig. 3.20. Catalytic performance of reduced catalysts (Pd/OMC, Fe/OMC, and Pd-Fe/OMC) in the selective cleavage of C-O bond in benzyl phenyl ether at 250 °C 10 bar (H₂) after 1 h-after.

Table 3.4

Catalytic performance of Pd/OMC, Pd-Fe/OMC, and Fe/OMC in the cleavage of C-O bond in benzyl phenyl ether to aromatics performed at 250 °C and 10 bar for 1 h

Catalyst	Conversion of benzyl phenyl ether (%)	Selectivity (%)						Yield for aromatics (%)
		Aromatics			Total	Aromatic	By-	
		Toluene	Phenol	Ethylbenzene	selectivity for aromatics	ring- saturated products		
Pd/OMC	93.0	17.3	0.7	20.9	38.9	47.1	14.0	36.2
Pd- Fe/OMC	88.5	45.1	36.3	2.6	84.0	4.6	11.4	74.3
Fe/OMC	50.1	49.3	23.5	1.5	74.3	0.2	25.5	37.2

3.3.4. XPS study of reduced catalysts

XPS analyses were further performed to elucidate interaction between reduced metal species in the bimetallic catalyst. Fig. 3.21 shows the XPS spectra of Pd 3d (Fig. 3.21 (a)) and Fe 2p_{3/2} (Fig. 3.21 (b)) levels of the reduced catalysts (Pd/OMC, Pd-Fe/OMC, and Fe/OMC). XPS analyses of Pd/OMC catalyst showed peaks of Pd 3d_{5/2} (solid line) and Pd 3d_{3/2} (dashed line) at 335.4 eV and 340.9 eV, respectively, which corresponded to the characteristic peaks of metallic Pd (Fig. 3.21 (a)) [60,61]. Fe/OMC catalyst showed a peak of Fe 2p_{3/2} at 707.4 eV, which corresponded to the characteristic peak of metallic Fe (Fig. 3.21 (b)) [69]. Interestingly, the binding energies for Pd 3d level in the Pd-Fe/OMC catalyst (334.4 eV and 339.7 eV for 3d_{5/2} and Pd 3d_{3/2}, respectively) were smaller than those in the Pd/OMC catalyst (Fig. 3.21 (a)). On the other hand, the binding energy of Fe 2p_{3/2} in the Pd-Fe/OMC (708.2 eV) was higher than that in the Fe/OMC catalyst (Fig. 3.21 (b)). The change of electronic property was attributed to different electronegativity of palladium and iron metal (1.8 and 2.2 for Fe and Pd, respectively), indicating that Fe atom might easily lose its electron to Pd atom [70,71]. From this result, it is clear that the electronic property of Pd atoms was modified by Fe atoms in the Pd-Fe/OMC catalyst. Therefore, it is expected that the increase in electron density around palladium particles would promote adsorption and activation of C-O bond in benzyl phenyl ether, suppressing the hydrogenation of C=C bond in aromatics and enhancing the selectivity for aromatics in the reaction.

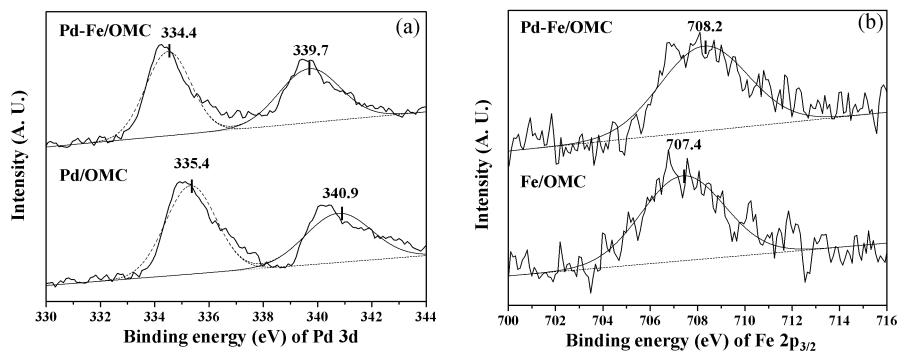


Fig. 3.21. XPS spectra of (a) Pd 3d and (b) Fe 2 P_{3/2} levels in the reduced catalysts (Pd/OMC, Fe/OMC, and Pd-Fe/OMC).

3.3.5. Hydrogen adsorption ability of reduced catalysts

As far as C-O bond cleavage in lignin model compounds over supported metal catalysts is concerned, it has been accepted that hydrogen is adsorbed and activated on the surface of metal sites. Adsorbed hydrogen on the surface of metal reacts with oxygen groups of reactant, leading to the cleavage of C-O bond in the reactant [72,73]. Therefore, the ability of hydrogen adsorption on the metal sites plays an important role in the reaction. Thus, H₂-TPD measurements were carried out in order to investigate the ability of hydrogen adsorption of the catalysts.

Fig. 3.22 shows the H₂-TPD profiles of reduced catalysts (Pd/OMC, Pd-Fe/OMC, and Fe/OMC). For comparison, H₂-TPD profile of OMC is also presented. H₂-TPD profile of OMC support exhibited a broad desorption peak at 634 °C, which was attributed to the gasification of carbon support [74]. As shown in Fig. 3.22, TPD profiles for all catalysts could be deconvoluted into two peaks. However, the peak appearing above 600 °C was due to hydrogen spillover to carbon support [74,75]. Therefore, the amount of desorbed hydrogen in the range of 200-600 °C was only considered for quantification. The amount of desorbed hydrogen calculated from the deconvoluted H₂-TPD profiles of the catalysts is summarized in Table 3.5. The amount of hydrogen desorbed from the reduced catalysts increased in the order of Fe/OMC < Pd-Fe/OMC < Pd/OMC, indicating that Pd/OMC catalyst retained the largest amount of hydrogen binding sites. However, the Pd/OMC catalyst tended to saturate benzene ring, leading to the formation of aromatic ring-saturated products. This is because activated hydrogen species on Pd surface are so active that they are not only able to cleave

C-O bond in benzyl phenyl ether but also able to hydrogenate C=C bond in aromatics [39,76]. On the other hand, Fe/OMC catalyst showed low conversion of benzyl phenyl ether, because the amount of activated hydrogen species on Fe surface was too small. Therefore, moderate hydrogen adsorption ability was required for effective production of aromatics by selective cleavage of C-O bond in benzyl phenyl ether. For this reason, Pd-Fe/OMC catalyst served as an efficient catalyst in the selective cleavage of C-O bond to aromatics.

On the basis of results described above, the interaction between Pd and Fe was found to occur through electron transfer from Fe atom to Pd atom. In the case of bimetallic Pd-Fe/OMC catalyst, the electron-deficient iron atoms (partially positive charged, δ^+) on the Pd-Fe surface act as adsorption sites for C-O group in benzyl phenyl ether via donation of electrons from one of the unshared electron pairs of the oxygen atom. The adsorbed activated hydrogen on nearby Pd then reacts with the adsorbed oxy-intermediate species, leading to the cleavage of C-O bond in benzyl phenyl ether [77,78]. On the other hand, high electron density of Pd atom on the Pd-Fe surface (partially negative charged, δ^-) decreases ability of hydrogen adsorption, resulting in the suppressed rate of hydrogenation of C=C bond in aromatics [77,78]. Thus, the synergistic electronic effect derived from interaction between Pd and Fe enables selective cleavage of C-O bond in benzyl phenyl ether to aromatics by suppressing the saturation of aromatic ring. In summary, the enhanced catalytic activity of Pd-Fe/OMC catalyst in the selective cleavage of C-O bond in benzyl phenyl ether was attributed to the modified electronic properties derived from interaction between Pd and Fe.

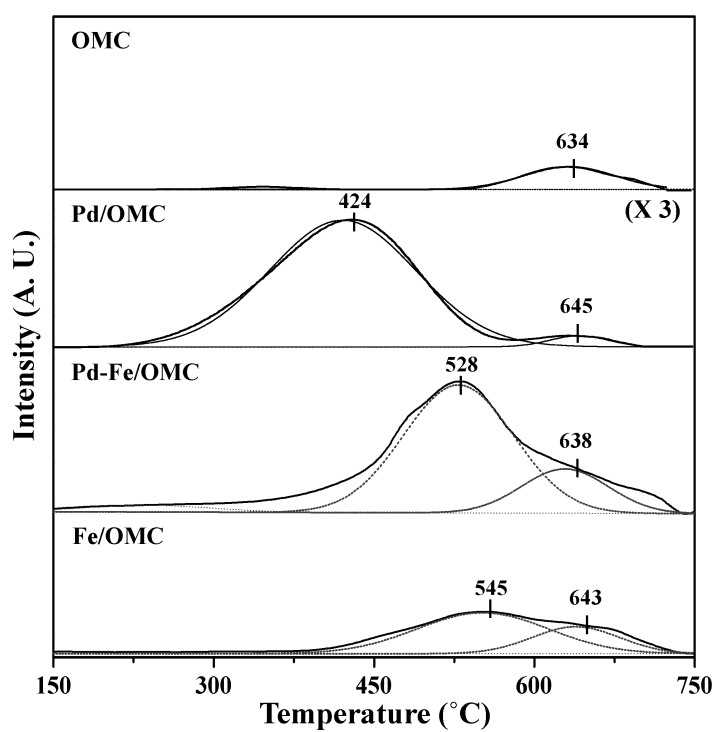


Fig. 3.22. H₂-TPD profiles of reduced catalysts (Pd/OMC, Fe/OMC, and Pd-Fe/OMC) and ordered mesoporous carbon (OMC)

Table 3.5

H₂-TPD results of reduced catalysts^a

Sample	Amount of desorbed hydrogen ($\mu\text{mol-H}_2/\text{g-cat.}$) ^a
OMC	1.2
Pd/OMC	221.1
Pd-Fe/OMC	74.8
Fe/OMC	24.8

^a Calculated from peak area of H₂-TPD profiles in Fig. 3.22

3.4. Characterization and catalytic activity of Pd-Fe bimetallic catalyst with a variation Fe/Pd molar ratio supported on ordered mesoporous carbon

3.4.1. Formation of reduced Pd₁-Fe_x/OMC bimetallic catalysts

Fig. 3.23 shows the HR-TEM images of the reduced Pd₁-Fe_x/OMC (X= 0, 0.25, 0.7, 1.5, and 4) catalysts. All the catalysts had an ordered mesoporous carbon structure with pores in the range of 4-6 nm, and they retained well-dispersed metal particles. Small metal particles with an average size of ca. 4 nm were observed in the TEM images of the catalysts, indicating that metal species were uniformly dispersed in the channels or on the walls of OMC. There was no noticeable difference in metal particle size of Pd₁-Fe_x/OMC (X= 0, 0.25, 0.7, 1.5, and 4) catalysts.

In order to see the distribution of palladium and iron species, STEM-EDX analyses were conducted. Fig. 3.24 shows the STEM and EDX mapping images of Pd₁-Fe_x/OMC (X= 0.25, 0.7, and 4) catalysts. It is noteworthy that particles of palladium and iron species were homogeneously distributed in the bimetallic Pd-Fe_x/OMC catalysts. Moreover, population density of Fe increased with increasing Fe/Pd molar ratio. On the other hand, aggregation of Fe was observed when a large amount of Fe was added in the Pd-Fe_x/OMC catalyst (Pd₁-Fe₄/OMC). Therefore, it is inferred that a Pd-Fe miscible phase was partially formed in the bimetallic catalysts; the rest of iron was presented as metallic iron.

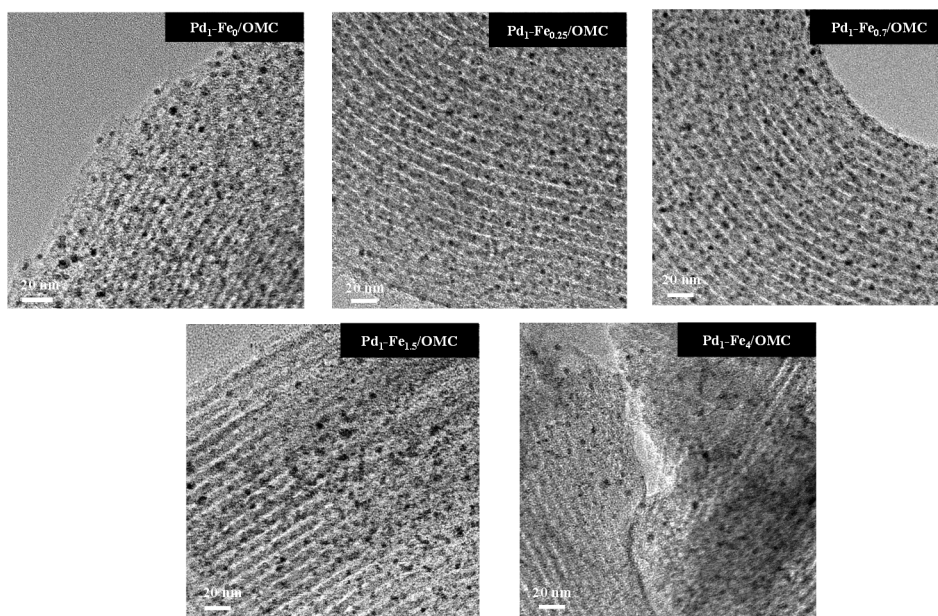


Fig. 3.23. TEM images of reduced $\text{Pd}_1\text{-Fe}_X/\text{OMC}$ ($X=0, 0.25, 0.7, 1.5,$ and 4) catalysts.

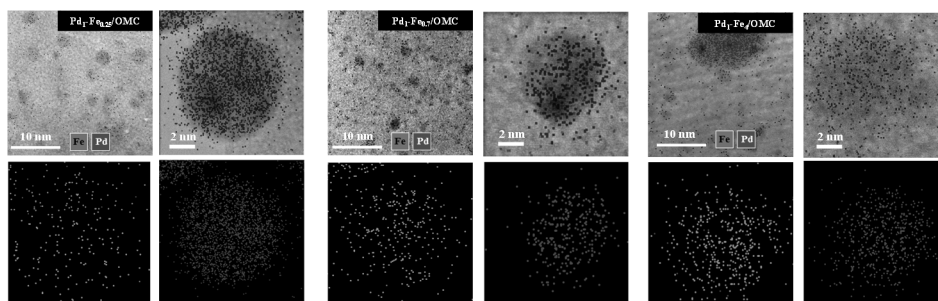


Fig. 3.24. STEM and EDX mapping images of Pd₁-Fe_x/OMC (X=0.25, 0.7, and 4) catalysts.

3.4.2. Textural properties of reduced Pd₁-Fe_x/OMC bimetallic catalysts

Fig. 3.25 shows the nitrogen adsorption-desorption isotherms of the reduced Pd₁-Fe_x/OMC (X= 0, 0.25, 0.7, 1.5, and 4) catalysts. All the catalysts exhibited type-IV isotherms with well-defined type-H3 hysteresis loops, indicating the formation of well-developed mesoporous structure [43,79]. Detailed textural properties of the reduced catalysts are summarized in Table 3.6. All the catalysts retained high surface area (> 732 m²/g), large pore volume (> 0.88 cm³/g), and large average pore diameter (> 4.0 nm). Surface area and pore volume of the catalysts slightly increased with increasing Fe/Pd molar ratio. This trend can be understood by the fact that the atomic radius of palladium (145 pm) is larger than that of iron (126 pm), which means that pore blockage by palladium is more severe than that by iron. However, average pore diameter of the catalysts was almost identical, suggesting that all the catalysts still retained pore characteristics of OMC. Chemical compositions of the reduced catalysts determined by ICP-AES analyses are also listed in Table 3.6. Actual Pd:Fe molar ratios of the catalysts were in good agreement with the designed values.

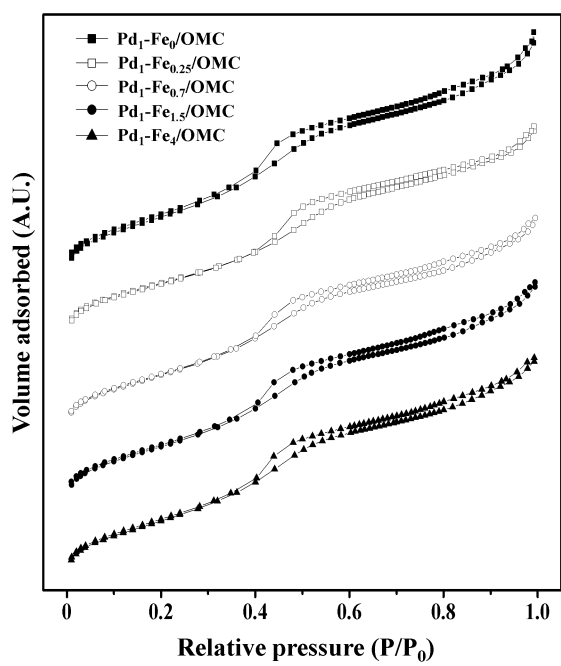


Fig. 3.25. Nitrogen adsorption-desorption isotherms of reduced Pd₁-Fe_X/OMC (X= 0, 0.25, 0.7, 1.5, and 4) catalysts.

Table 3.6

Textural properties of reduced Pd₁-Fe_X/OMC (X= 0, 0.25, 0.7, 1.5, and 4) catalysts

Catalyst	Pd : Fe molar ratio ^a	Surface area (m ² /g) ^b	Pore volume (cm ³ /g) ^c	Pore diameter (nm) ^d
Pd ₁ -Fe ₀ /OMC	-	832	0.88	4.1
Pd ₁ -Fe _{0.25} /OMC	0.21 : 0.79	850	0.90	4.2
Pd ₁ -Fe _{0.7} /OMC	0.40 : 0.60	862	0.91	4.0
Pd ₁ -Fe _{1.5} /OMC	0.61 : 0.39	872	0.92	4.1
Pd ₁ -Fe ₄ /OMC	0.81 : 0.19	882	0.94	4.3

^a Determined by ICP-AES measurement

^b Calculated by the BET equation

^c Total pore volume at P/P₀ = 0.99

^d Average pore diameter

3.4.3. Crystalline structure of reduced Pd₁-Fe_x/OMC bimetallic catalysts

Crystalline phases of the reduced catalysts were examined by XRD measurements as shown in Fig. 3.26. All the catalysts showed a characteristic diffraction peak for graphitic carbon at $2\theta = 23.5^\circ$ [56]. The reduced Pd₁-Fe₀/OMC catalyst showed diffraction peaks at 40.1° , 46.6° , and 68.3° , corresponding to metallic palladium (closed circle in Fig. 3.26 (a)) [80,81]. Fig. 3.26 (b) shows the enlarged Pd (111) XRD patterns of Pd₁-Fe_x/OMC (X= 0, 0.25, 0.7, 1.5, and 4) catalysts. It was found that the characteristic diffraction peaks for palladium slightly but consistently shifted to higher angle in the Pd₁-Fe_x/OMC (X= 0, 0.25, 0.7, 1.5, and 4) catalysts with increasing Fe/Pd molar ratio. The Pd (111) peaks for Pd₁-Fe_x/OMC (X= 0, 0.25, 0.7, 1.5, and 4) catalysts appeared at 40.1° , 40.2° , 40.4° , 40.6° , and 40.7° , respectively (Fig. 3.26 (b)). This consistent shift is an evidence for the formation of miscible phase between Pd and Fe through incorporation Fe atom into the lattice of Pd, as reported in the literatures [80,81]. On the other hand, diffraction peaks for metallic iron was not observed in the Pd₁-Fe_x/OMC (X= 0.25 and 0.7) catalysts due to its small crystalline size or low concentration (opened circle in Fig. 3.26 (a) and (b)) [82,83]. However, Pd₁-Fe_x/OMC (X= 1.5 and 4) catalysts exhibited a diffraction peak for metallic iron (opened circle in Fig. 3.26 (a) and (b)), and the peak intensity increased with increasing iron content. This is because both Pd₁-Fe_{1.5}/OMC and Pd₁-Fe₄/OMC catalysts had Fe enriched-surface by segregating Fe on the Pd-Fe surface, especially for the catalyst with higher Fe content (Fe/Pd \geq 1.5) [40,84]. From

XRD results, it was revealed that bimetallic phase of Pd₁-Fe_x/OMC catalysts were greatly affected by the Fe/Pd molar ratio.

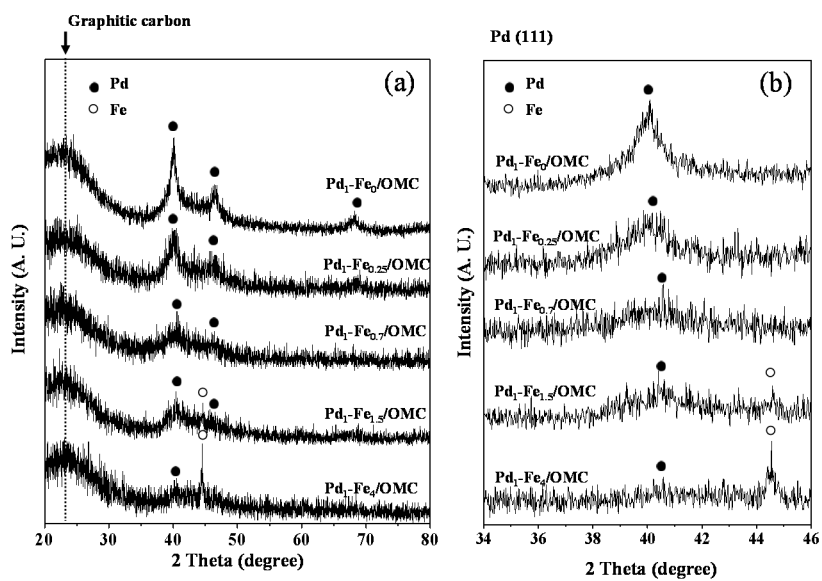


Fig. 3.26. XRD patterns of (a) reduced Pd₁-Fe_X/OMC catalysts and (b) enlarged Pd (111) diffraction peaks for Pd₁-Fe_X/OMC catalysts.

3.4.4. Reduction behavior calcined Pd₁-Fe_x/OMC catalysts

It is known that H₂-TPR measurement is a powerful tool for examining reduction behavior and interaction between two metal species of the catalyst. Fig. 3.27 shows the TPR profiles of the calcined Pd₁-Fe_x/OMC (X= 0, 0.25, 0.7, 1.5, and 4) catalysts. TPR profile of Pd₁-Fe₀/OMC catalyst showed a negative peak at 60 °C and a positive peak at 170 °C; the former was attributed to the decomposition of palladium hydride phase (PdH_x) [84-86], while the latter was attributed to the reduction of palladium species [84-86]. Interestingly, the reduction behaviors of Pd₁-Fe_x/OMC (X= 0.25, 0.7, 1.5, and 4) catalysts were quite different depending on Fe/Pd molar ratio. For precise investigation, TPR profiles of Pd₁-Fe_x/OMC (X= 0.25, 0.7, 1.5, and 4) catalysts were deconvoluted. As shown in Fig. 3.27, bimetallic Pd₁-Fe_x/OMC (X= 0.25, 0.7, 1.5, and 4) catalysts showed three deconvoluted reduction peaks. As shown in Fig. 3.18, reduction of Fe catalyst supported on ordered mesoporous carbon (Fe/OMC) occurred through three steps. Fe₂O₃ was reduced to Fe₃O₄ (335 °C) in the first step. The second step involved the reduction of Fe₃O₄ to FeO (496 °C), which was subsequently reduced to metallic Fe (596 °C). As shown in Fig. 3.27, Pd₁-Fe_x/OMC (X= 0.25, 0.7, 1.5, and 4) catalysts also showed three distinct peaks, but the peaks moved toward low temperature compared to those of Fe/OMC catalyst. It is well known that reducibility of bimetallic catalyst was strongly affected by the interaction between two metal species [86,87]. In particular, bimetallic catalysts containing noble metal facilitate the reduction of other transition metal due to hydrogen transfer from their reduced species [87,88].

Therefore, it can be inferred that activated hydrogen on the reduced palladium species was transferred to unreduced Fe species during the reduction process, which promoted the reduction of Fe species. In addition, the negative peak corresponding to palladium hydride (PdH_x) disappeared upon addition of Fe, indicating that iron species suppressed the formation of PdH_x phases due to the strong interaction between metal species [85]. With increasing Fe content ($\text{Fe/Pd} \geq 1.5$), furthermore, intensity of reduction peak above 350 °C was remarkably increased. This might be because a fraction of Fe remained as metallic species on the carbon support, as evidenced by XRD results. Thus, it is expected that Pd and Fe fractions were co-reduced by partially forming a Pd-Fe bimetallic phase. From XRD and TPR results, it can be inferred that bimetallic phase could be controlled by changing Fe/Pd ratio, which might strongly affect the catalytic performance.

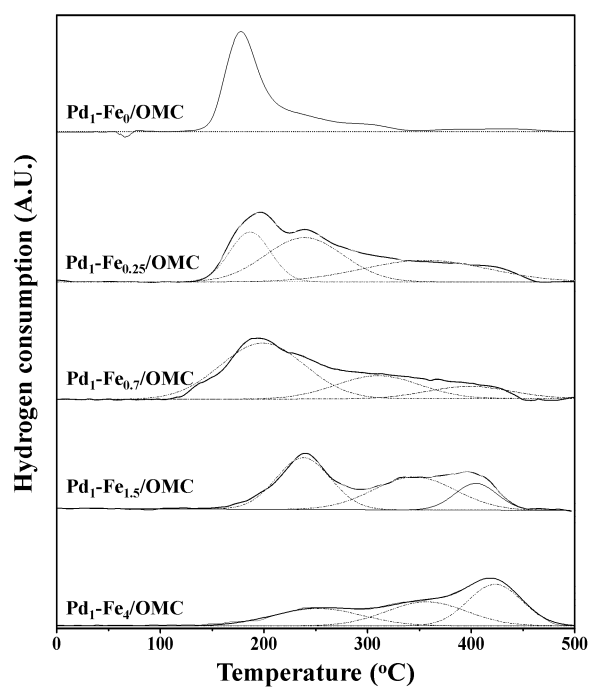


Fig. 3.27. TPR profiles of calcined Pd₁-Fe_X/OMC (X= 0, 0.25, 0.7, 1.5, and 4) catalysts.

3.4.5. Catalytic performance in the selective cleavage of C-O bond in phenethyl phenyl ether

Fig. 3.28 shows the reaction pathways for decomposition of phenethyl phenyl ether (PPE). According to the literatures [89,90], the cleavage of β -O-4 linkage follows parallel-consecutive reaction pathways. Aromatic compounds are produced by the cleavage of C_{β} -O bond in phenethyl phenyl ether, and consecutive hydrogenation of aromatic ring leads to the formation of aromatic ring-saturated products. On the other hand, hydrogenation of aromatic ring in phenethyl phenyl ether occurs prior to C_{β} -O bond cleavage, which also produces aromatic ring-saturated products. In our catalytic reaction, aromatic compounds such as benzene, phenol, and ethylbenzene were produced by the cleavage of C-O bond in phenethyl phenyl ether. Aromatic ring-saturated products including cyclohexane derivatives (cyclohexane, cyclohexanol, and ethylcyclohexane) and fully hydrogenated PPE were also produced by the hydrogenation of aromatic rings. Light hydrocarbon (C_1 - C_3) and phenylethyl benzene were produced as by-products.

Catalytic performance of the reduced Pd_1-Fe_X/OMC ($X= 0, 0.25, 0.7, 1.5,$ and 4) catalysts in the decomposition of phenethyl phenyl ether performed at 250°C and 10 bar for 3 h is summarized in Table 3.7. In the absence of catalyst, conversion of phenethyl phenyl ether was very low although selectivity for aromatics was high, resulting in low yield for aromatics. This result indicates that catalytic decomposition of phenethyl phenyl ether does not proceed in the absence of catalyst because C-O and C-C bonds are thermally stable. All the

catalysts showed an enhanced conversion of phenethyl phenyl ether compared to the case of no catalyst. Pd₁-Fe₀/OMC catalyst was very active for hydrogenation of aromatic ring in phenethyl phenyl ether, leading to the formation of aromatic ring-saturated products. On the other hand, bimetallic catalysts showed the relatively low activity toward hydrogenation of aromatic ring. Catalytic performance of Pd₁-Fe_x/OMC (X= 0, 0.25, 0.7, 1.5, and 4) catalysts was strongly influenced by Fe/Pd molar ratio. In order to visualize the effect of Fe/Pd molar ratio on the catalytic performance of bimetallic Pd₁-Fe_x/OMC (X= 0, 0.25, 0.7, 1.5, and 4) catalysts, conversion of phenethyl phenyl ether, selectivity for aromatics, and yield for aromatics were plotted as a function of Fe/Pd molar ratio (X) as shown in Fig. 3.29. Conversion of phenethyl phenyl ether decreased with increasing Fe/Pd molar ratio. On the other hand, selectivity for aromatics increased with increasing Fe/Pd molar ratio up to 0.7 (Fe/Pd < 0.7), but it was almost constant at high Fe/Pd molar ratio (Fe/Pd ≥ 0.7). The compensation between conversion of phenethyl phenyl ether and selectivity for aromatics led to a volcano-shaped curve of aromatic yield with respect to Fe/Pd molar ratio. Thus, an optimal Fe/Pd molar ratio was required for achieving maximum catalytic performance toward aromatic production. Among the catalysts tested, Pd₁-Fe_{0.7}/OMC catalyst showed the highest yield for aromatics.

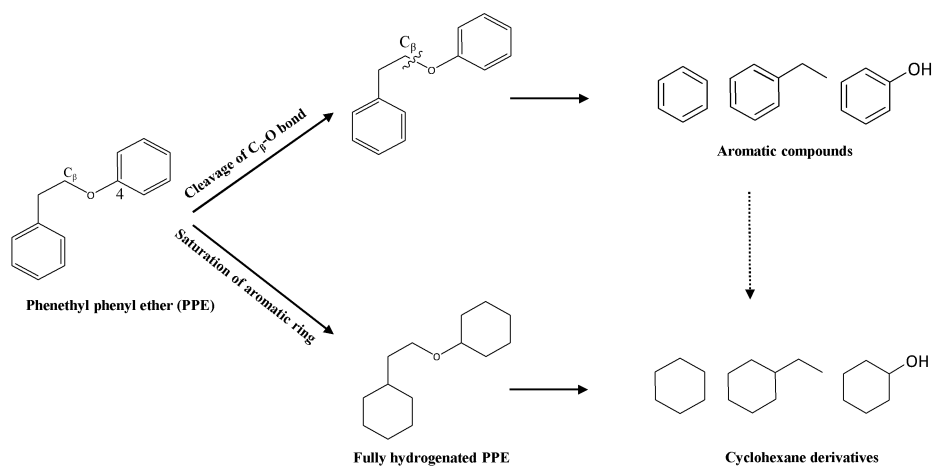


Fig. 3.28. Reaction pathways for decomposition of phenethyl phenyl ether.

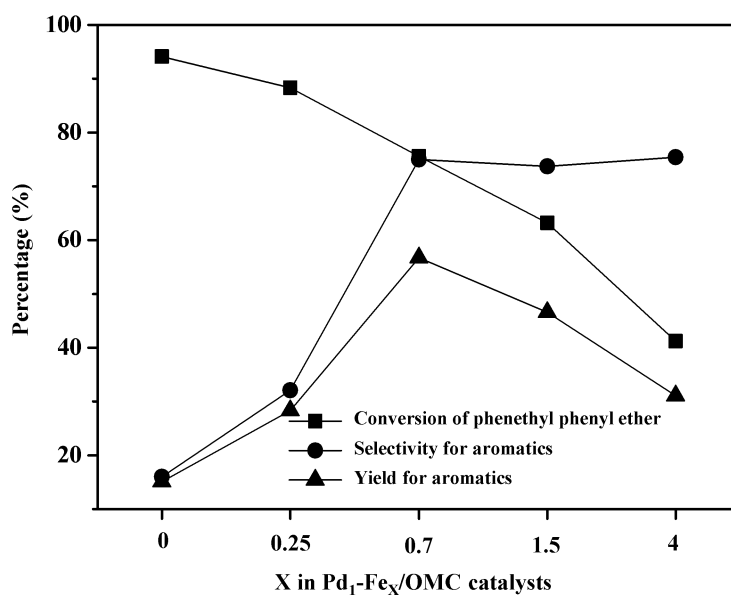


Fig. 3.29. Catalytic performance of Pd₁-Fe_X/OMC (X= 0, 0.25, 0.7, 1.5, and 4) catalysts in the decomposition of phenethyl phenyl ether, plotted as a function of Fe/Pd molar ratio (X). Reaction conditions: temperature= 250 °C, pressure= 10 bar (H₂), and time= 3 h.

Table 3.7

Catalytic performance of reduced Pd₁-Fe_x/OMC (X= 0, 0.25, 0.7, 1.5, and 4) catalysts in the catalytic decomposition of phenethyl phenyl ether (PPE) performed at 250 °C and 10 bar for 3 h

Catalyst	Conversion of PPE (%)	Aromatics					Selectivity (%)				Yield for aromatics
		Benzene		Phenol		Ethylbenzene	Total selectivity for aromatics	Aromatic ring-saturated product		By-products	
		Phenol	Benzene	Cyclohexane derivatives	Fully hydrogenated PPE						
No catalyst	3.2	2.7	40.3	34.5	77.5	2.8	2.5	17.2	2.5	2.5	
Pd ₁ -Fe ₀ /OMC	94.1	7.2	5.4	3.4	16.0	59.3	15.6	9.1	15.1	15.1	
Pd ₁ -Fe _{0.25} /OMC	88.3	13.6	6.2	12.3	32.1	48.5	9.8	9.6	28.3	28.3	
Pd ₁ -Fe _{0.7} /OMC	75.6	26.5	21.3	27.2	75.0	12.4	2.6	10.0	56.7	56.7	
Pd ₁ -Fe _{1.5} /OMC	63.2	22.8	23.3	27.6	73.7	10.8	6.1	9.4	46.6	46.6	
Pd ₁ -Fe ₄ /OMC	41.2	21.4	25.6	28.4	75.4	8.5	6.2	9.9	31.1	31.1	

3.4.6. Hydrogen adsorption study on the reduced Pd₁-Fe_x/OMC catalysts

Catalytic decomposition of lignin through hydrogenation (including hydrogenolysis) on metal sites occurs via following steps; (1) gas phase hydrogen is dissociatively adsorbed and activated on the surface of metal sites, and (2) adsorbed hydrogen on the surface of metal sites reacts with oxygen groups of reactant or C=C bond in lignin, leading to the cleavage of C-O or C=C bond in reactant, respectively. Therefore, hydrogen adsorption ability on the surface of metal sites plays an important role in the catalytic decomposition of lignin model compounds [91,92]. For this reason, H₂-TPD measurement was carried out in order to investigate the hydrogen adsorption ability of the reduced catalysts.

Fig. 3.30 shows the H₂-TPD profiles of the reduced Pd₁-Fe_x/OMC (X= 0, 0.25, 0.7, 1.5, and 4) catalysts. H₂-TPD profiles of the reduced catalysts could be deconvoluted into two hydrogen desorption peaks. According to the literature [74], the peak above 600 °C is related to the gasification of carbon support. In this work, therefore, hydrogen desorption peak below 600 °C, which was related to the desorption of hydrogen from the reduced palladium and iron species, was only considered for quantification. The amount of desorbed hydrogen was calculated from the deconvoluted peak area of H₂-TPD profile (< 600 °C), as listed in Table 3.8. It was found that the amount of desorbed hydrogen was greatly affected by Fe/Pd molar ratio. The amount of hydrogen desorbed from the reduced catalysts decreased in the order of Pd₁-Fe₀/OMC > Pd₁-Fe_{0.25}/OMC > Pd₁-Fe_{0.7}/OMC > Pd₁-Fe_{1.5}/OMC > Pd₁-Fe₄/OMC. This trend was well

consistent with the trend of conversion of phenethyl phenyl ether (Fig. 3.29). It is known that the enhancement in the amount of chemisorbed hydrogen is beneficial to improve the catalytic activity. However, it was observed that Pd₁-Fe₀/OMC catalyst had a strong tendency to saturate aromatic ring in the reaction. This is because the surface of Pd with strong hydrogen adsorption ability stabilizes the π -bonded complex with aromatic rings and participates in hydrogenation, resulting in cleavage of C=C bond in aromatic ring [40]. With increasing Fe/Pd molar ratio, on the other hand, conversion of phenethyl phenyl ether was monotonically decreased (Fig. 3.29). This trend can be explained by the dilution effect of inactive Fe onto Pd, which decreases the total number of available active sites for hydrogen adsorption. Therefore, it is believed that moderate hydrogen adsorption ability was required for enhanced aromatic production. However, no correlation between hydrogen adsorption ability and aromatic selectivity was found. Therefore, our next investigation was focused on the effect chemical state of metal species on the aromatic selectivity. For this purpose, XPS analyses of the reduced Pd₁-Fe_X/OMC (X= 0, 0.25, 0.7, 1.5, and 4) catalysts were carried out.

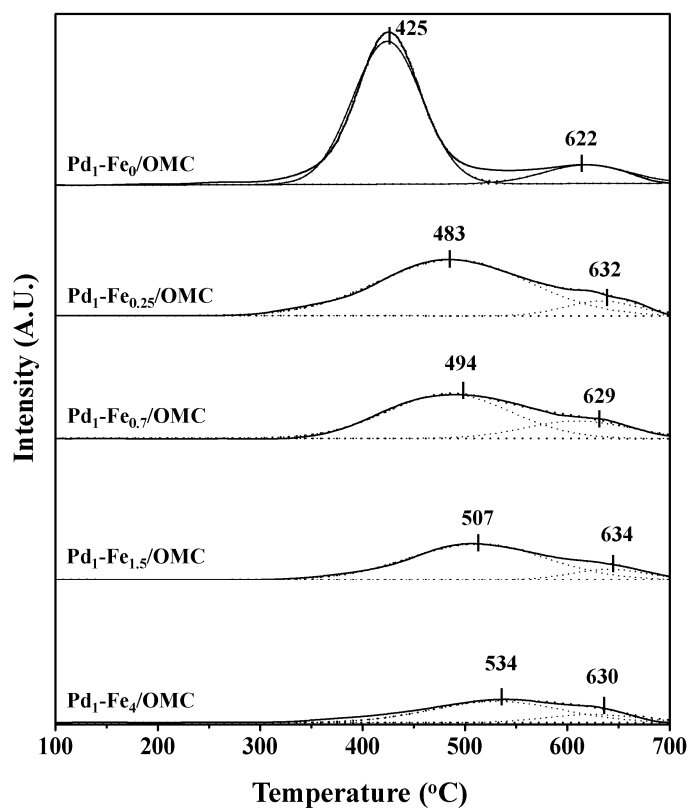


Fig. 3.30. H₂-TPD profiles of reduced Pd₁-Fe_X/OMC (X= 0, 0.25, 0.7, 1.5, and 4) catalysts.

Table 3.8

H₂-TPD results of reduced Pd₁-Fe_x/OMC (X= 0, 0.25, 0.7, 1.5, and 4) catalysts

Catalyst	Amount of desorbed hydrogen ($\mu\text{mol-H}_2/\text{g-cat.}$) ^a
Pd ₁ -Fe ₀ /OMC	128.2
Pd ₁ -Fe _{0.25} /OMC	92.9
Pd ₁ -Fe _{0.7} /OMC	79.1
Pd ₁ -Fe _{1.5} /OMC	52.8
Pd ₁ -Fe ₄ /OMC	37.8

^a Calculated from peak area of H₂-TPD profile (< 600 °C) in Fig. 3.30

3.4.7. XPS study of reduced Pd₁-Fe_X/OMC catalysts

Fig. 3.31 shows the XPS spectra of Pd 3d (Fig. 3.31 (a)) and Fe 2p_{3/2} (Fig. 3.31 (b)) levels of the reduced Pd₁-Fe_X/OMC (X= 0, 0.25, 0.7, 1.5, and 4) catalysts. The Pd 3d spectra were deconvoluted into Pd_{5/2} (solid line) and Pd_{3/2} (dashed line) peaks, and then Pd 3d spectra were divided into Pd⁰ (335.2 eV and 340.5 eV for 3d_{5/2} and 3d_{3/2}, respectively) and Pd²⁺ (337.1 eV and 341.9 eV for 3d_{5/2} and 3d_{3/2}, respectively) species [60,61]. The Fe 2p_{3/2} spectra were assigned to metallic Fe⁰ (707.6 eV), Fe²⁺ (709.6 eV), and Fe³⁺ (710.9 eV) species [69]. Interestingly, the binding energy of Pd 3d level in the Pd₁-Fe_X/OMC (X= 0.25, 0.7, 1.5, and 4) catalysts slightly shifted toward low value with increasing Fe/Pd molar ratio (Fig. 3.31 (a)). On the other hand, the binding energy of Fe 2p_{3/2} level in the Pd₁-Fe_X/OMC (X= 0.25, 0.7, 1.5, and 4) catalysts shifted toward high value with increasing Fe/Pd molar ratio (Fig 3.31 (b)). The change of electronic properties was attributed to charge transfer from Fe to Pd, which was related to the relative electronegativity of each metal (1.8 and 2.2 for Fe and Pd, respectively, according to the Pauling's scale) [80,81]. The charge transfer between two metal species induces polarity on bimetallic phase. In the case of Pd on the Pd-Fe surface, electron-rich palladium atoms decreased the stability of π-bonded complex with aromatic ring, resulting in the suppressed rate of hydrogenation of C=C bond in aromatics. In the case of Fe on the Pd-Fe surface, on the other hand, electron-deficient Fe atoms acted as adsorption sites for activating oxygenated group and facilitating hydrogenation of C-O bond in phenethyl phenyl ether. For this reason, bimetallic Pd₁-Fe_X/OMC (X= 0.25, 0.7,

1.5, and 4) catalysts were more efficient in the selective cleavage of C-O bond in phenethyl phenyl ether to aromatics than Pd₁-Fe₀/OMC catalyst. Judging from XPS results, it can be inferred that electron-deficient iron atoms (Fe^{δ+}) was in contact with metallic palladium atoms (Pd⁰), forming a bimetallic phase on the catalyst surface [77,93]. In order to confirm the chemical state of bimetallic phase in the Pd₁-Fe_x/OMC catalysts, the chemical state ratios of Pd and Fe were quantified as summarized in Table 3.9. Chemical state of each metal species was obtained by integrating each deconvoluted XPS peak area for Pd and Fe species. It was found that Pd⁰/Pd_{total} increased with increasing Fe/Pd molar ratio, and Fe^{δ+}/Fe_{total} also increased with increasing Fe/Pd molar ratio. Interestingly, Fe^{δ+}/Pd showed no significant difference at high Fe/Pd molar ratio above 0.7. This result suggests that Pd and Fe are in contact with each other in the same molar ratio at high Fe/Pd molar ratio above 0.7. In addition, the result of Fe^{δ+}/(Pd⁰+Fe^{δ+}) molar ratios of Pd₁-Fe_x/OMC (X= 0.7, 1.5, and 4) catalysts revealed that the bimetallic catalysts were mainly composed of bimetallic structure of Pd₁Fe_{0.7} composition at high Fe/Pd molar ratio above 0.7; the remaining fraction of metal species existed as a metallic state on the carbon support, as evidenced by STEM-EDX, XRD and TPR results. This result was well consistent with the previous work [80] (Section 3.3), reporting that metallic Fe alone was catalytically inactive for the hydrogenation C=C bond in aromatics. Thus, it is inferred that the bimetallic structure of Pd₁Fe_{0.7} composition of the catalysts was mainly responsible for high and constant selectivity for aromatics at Fe/Pd ≥ 0.7 in the selective cleavage of C-O bond in phenethyl phenyl ether (Table 3.9 and Fig. 3.31). Another noticeable point is that binding energy of metallic Fe in the Pd₁-Fe_{0.25}/OMC was 707.2 eV.

This binding energy value of metallic Fe in the Pd₁-Fe_{0.25}/OMC catalyst was slightly higher than 2p_{3/2} binding energy of metallic iron which was reported to be 706.8 eV [94]. Considering that the binding energy shift was closely related to the binding strength of two metals [95,96], it is expected that the interaction does not lead to the complete formation of bimetallic phase due to low concentration of Fe. Therefore, it is concluded that saturation of aromatics ring was not effectively suppressed over the bimetallic catalyst with low Fe content (Pd₁-Fe_{0.25}/OMC).

On the basis of H₂-TPD and XPS results, it is believed that an optimal Fe/Pd molar ratio was required for the formation of bimetallic structure of Pd₁Fe_{0.7} composition and for the moderate hydrogen adsorption ability, and in turn, for the highest yield for aromatics over Pd₁-Fe_X/OMC (X= 0, 0.25, 0.7, 1.5, and 4) catalysts. Schemes of the proposed model for the promotion C-O group in bimetallic Pd₁-Fe_X/OMC (X= 0, 0.7, and 4) catalysts was presented in Fig. 3.32.

Table 3.9
XPS analyses results of reduced Pd₁-Fe_x/OMC (X= 0, 0.25, 0.7, 1.5, and 4) catalysts

Catalyst	Ratio of Pd species ^a		Ratio of Fe species ^a		Fe ^{δ+} /Pd ^b	Fe ^{δ+} /(Pd ⁰ +Fe ^{δ+}) ^b	Composition of bimetallic structure
	Pd ⁰ /Pd _{total}		Fe ^{δ+} /Fe _{total} ^b				
Pd ₁ -Fe ₀ /OMC	0.52	-	-	-	-	-	-
Pd ₁ -Fe _{0.25} /OMC	0.59	0.28	0.49	0.29	0.49	0.29	Pd ₁ Fe _{0.4}
Pd ₁ -Fe _{0.7} /OMC	0.68	0.45	0.65	0.40	0.65	0.40	Pd ₁ Fe _{0.7}
Pd ₁ -Fe _{1.5} /OMC	0.73	0.47	0.66	0.39	0.66	0.39	Pd ₁ Fe _{0.7}
Pd ₁ -Fe ₄ /OMC	0.74	0.49	0.65	0.40	0.65	0.40	Pd ₁ Fe _{0.7}

^a Calculated from deconvoluted peak area of XPS spectra in Fig. 3.31

^b $2 \leq \delta \leq 3$

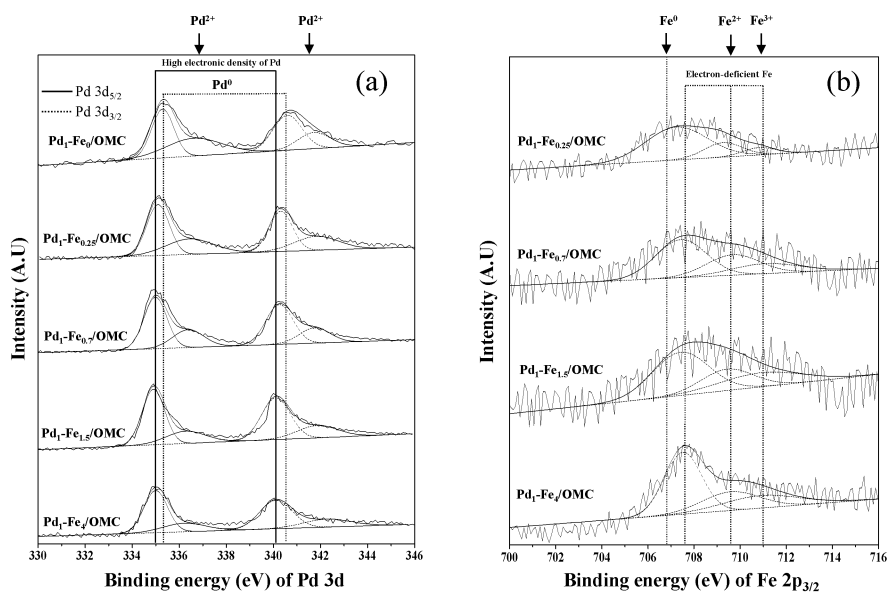


Fig. 3.31. XPS spectra of (a) Pd 3d and (b) Fe 2P_{3/2} levels in the reduced Pd₁-Fe_X/OMC (X= 0, 0.25 ,0.7, 1.5, and 4) catalysts.

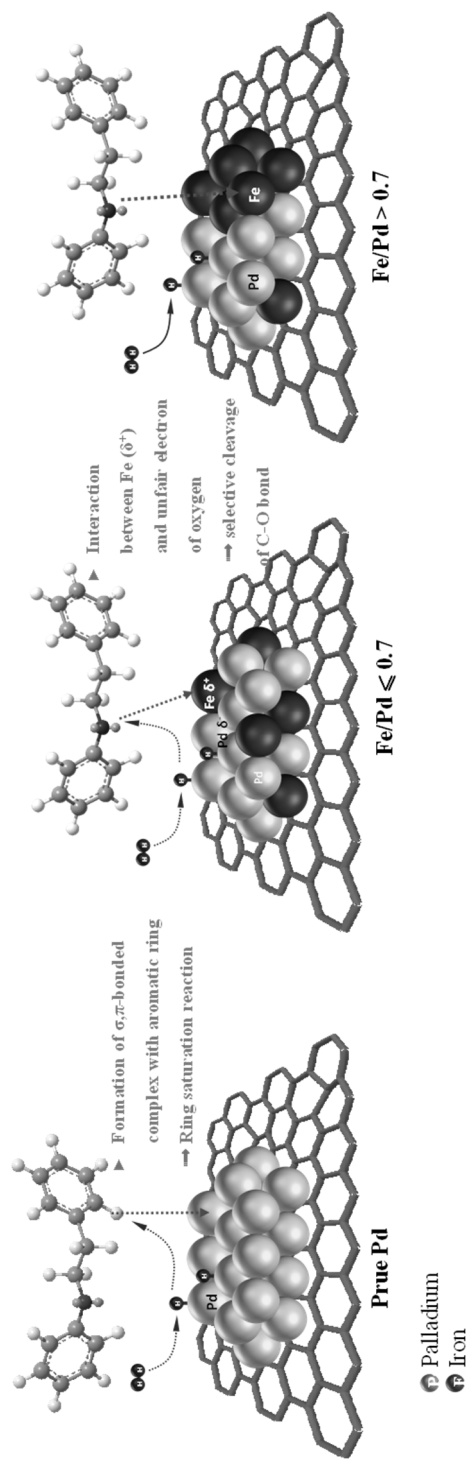


Fig. 3.32. Schemes of the proposed model for the promotion C-O group in bimetallic Pd₁-Fe_x/OMC (X= 0, 0.7, and 4) catalysts.

Chapter 4. Conclusions

In this work, several series of palladium catalysts based supported on ordered mesoporous carbon were prepared for the cleavage of C-O bond in lignin model compounds to aromatics. 2,3-Dihydrobenzofuran, benzyl phenyl ether, and phenethyl phenyl ether were employed lignin model compounds for representing β -5, α -O-4, and β -O-4 bond in lignin inner units, respectively. The catalytic system, in this study, was divided into two parts. The first parts were bifunctional catalysts including sulfonated ordered mesoporous carbon supported palladium catalyst (Pd/OMC-SO₃H-X) and cesium-exchanged heteropolyacid impregnated ordered mesoporous carbon supported palladium catalyst (Pd/XCs_{2.5}H_{0.5}PW₁₂O₄₀/OMC). The effect of acid properties on the catalytic performance of the catalysts in the decomposition of lignin model compounds was investigated. Acid properties of the catalysts was measured by NH₃-TPD experiments. A correlation between acid properties and catalytic performance of the catalysts was then established. In second part, bimetallic Pd-Fe catalysts were characterized and evaluated for selective cleavage of C-O bond in lignin model compounds with aim of improving aromatics productivity. Interaction between Pd and Fe resulted in the modification of electronic properties of Pd by electronic transfer from Fe to Pd, which is remarkably changed the catalytic activity.

Ordered mesoporous carbon (OMC) was sulfonated at different temperature (OMC-SO₃H-X, X=125, 150, 175, 200, and 225 °C). Palladium catalysts were then supported on OMC-SO₃H-X by an incipient wetness impregnation method, and they were applied to the decomposition of 2,3-dihydrobenzofuran to aromatic compounds. 2,3-Dihydrobenzofuran was used as

a lignin model compound for representing β -5 linkage in lignin. Conversion of 2,3-dihydrobenzofuran and total yield for aromatics (2-ethylphenol, phenol, ethylbenzene) increased with increasing acidity of Pd/OMC-SO₃H-X catalysts. Among the catalysts tested, Pd/OMC-SO₃H-150 with the largest acidity showed the highest conversion (56.3%) and the highest total yield for aromatics (49.7%). It is concluded that acidity of Pd/OMC-SO₃H-X catalysts played an important role in determining the catalytic performance in the decomposition of 2,3-dihydrobenzofuran to aromatic compounds.

A series of Cs_{2.5}H_{0.5}PW₁₂O₄₀ supported on OMC (XC_{s2.5}H_{0.5}PW₁₂O₄₀/OMC) were prepared with a variation of Cs_{2.5}H_{0.5}PW₁₂O₄₀ content (X= 10-30 wt%). Palladium catalysts supported on XC_{s2.5}H_{0.5}PW₁₂O₄₀/OMC were then prepared by an incipient wetness impregnation method, and they applied to the catalytic decomposition of 2,3-dihydrobenzofuran. 2,3-Dihydrobenzofuran was used as a lignin model compounds for representing β -5 linkage of lignin. Conversion of 2,3-dihydrobenzofuran and total yield for aromatics (2-ethylphenol, phenol, ethylbenzene) increased with increasing acidity of Pd/XC_{s2.5}H_{0.5}PW₁₂O₄₀/OMC catalysts. Among the catalysts tested, Pd/20Cs_{2.5}H_{0.5}PW₁₂O₄₀/OMC with the largest acidity showed the highest conversion of 2,3-dihydrobenzofuran (87.5%) and the highest total yield for aromatics (67.3%). Thus, acidity of the catalysts played an important role in determining the catalytic performance in the decomposition of 2,3-dihydrobenzofuran over Pd/XC_{s2.5}H_{0.5}PW₁₂O₄₀/OMC catalysts.

Bimetallic Pd-Fe/OMC and monometallic Pd/OMC and Fe/OMC catalysts were characterized and evaluated for selective cleavage C-O bond in benzyl phenyl ether with an aim of improving aromatics productivity. It was found that

Pd/OMC catalyst showed the highest conversion of benzyl phenyl ether. However, significant hydrogenation of aromatics occurred over Pd/OMC catalyst, leading to low selectivity for aromatics. On the other hand, Fe/OMC catalyst showed lower conversion of benzyl phenyl ether than Pd/OMC, but Fe/OMC exhibited higher selectivity for aromatics than Pd/OMC without hydrogenation of aromatic ring. Among the catalysts, bimetallic Pd-Fe/OMC catalyst with moderate hydrogen adsorption ability showed the highest yield for aromatics. The enhanced catalytic performance of Pd-Fe/OMC catalyst in the selective cleavage of benzyl phenyl ether to aromatics was attributed to the modification of electronic properties of surface Pd-Fe, which caused electron transfer from Fe to Pd.

A series of bimetallic Pd-Fe catalysts supported on ordered mesoporous carbon ($\text{Pd}_1\text{-Fe}_x/\text{OMC}$, $X=0, 0.25, 0.7, 1.5, 4$) were characterized and evaluated in order to find optimum Fe/Pd molar ratio for maximum production of aromatics through catalytic decomposition of phenethyl phenyl ether (a model compound for representing β -O-4 bond in lignin). It was found that physicochemical properties of bimetallic catalysts were greatly affected by Fe/Pd molar ratio. In particular, interaction between Pd and Fe resulted in the modification of electronic properties of Pd by electronic transfer from Fe to Pd, which remarkably changed the hydrogen adsorption ability and bimetallic structure. In the catalytic decomposition of phenethyl phenyl ether to aromatics, hydrogen adsorption ability and bimetallic structure of the catalysts were closely related to conversion of phenethyl phenyl ether and selectivity for aromatics, respectively. Conversion of phenethyl phenyl ether decreased with increasing hydrogen adsorption ability, while maximum selectivity for aromatics was obtained when

the bimetallic structure of Pd₁Fe_{0.7} was formed. Among the catalysts tested, Pd₁-Fe_{0.7}/OMC catalyst with moderate hydrogen adsorption ability and with bimetallic structure of Pd₁Fe_{0.7} composition showed the best catalytic performance in terms of yield for aromatics.

In summary, in order to enhance aromatic productivity through the selective cleavage of C-O bond in lignin model compounds, physicochemical properties of palladium-based catalysts were modified by various co-catalysts addition. Catalytic activity of the catalysts were closely related to several physicochemical properties such as acidity, surface area, porosity, crystalline structure, hydrogen adsorption ability, and adsorption geometry of reactant. In bifunctional catalysts, it was found that acidity of the catalyst served as an important factor determining overall catalytic activity in the catalytic decomposition of lignin model compound. On the other hand, in case of bimetallic Pd-Fe catalysts, hydrogen adsorption and bimetallic structure of the catalysts played as an important factor determining overall catalytic activity in the selective cleavage of lignin model compounds to aromatics.

Bibliography

- [1] C.E. Wyman, “Ethanol from lignocellulosic biomass: Technology, economics, and opportunities”, *Bioresour. Technol.* 50 (1994) 3.
- [2] M. Stöcker, “Biofuels and biomass-to-liquid fuels in the biorefinery: catalytic conversion of lignocellulosic biomass using porous materials”, *Angew. Chem. Int. Ed.* 47 (2008) 9200.
- [3] H.L. Chum, R.P. Overend, “Biomass and renewable fuels”, *Fuel Process. Technol.* 71 (2001) 187.
- [4] D. Stewart, “Lignin as a base material for materials applications: Chemistry, application and economics”, *Ind. Corp. Prod.* 27 (2008) 202.
- [5] R.J.A. Grosselink, E. de Jong, D. Guran, A. Aächerli, “Co-ordination network for lignin—standardisation, production and applications adapted to market requirements (EUROLIGNIN)”, *Ind. Corp. Prod.* 27 (2008) 202.
- [6] J. Zakzeski, P.C.A. Bruijninx, A.L. Jongerius, B.M. Weckhuysen, “The catalytic valorization of lignin for the production of renewable chemicals”, *Chem. Rev.* 110 (2010) 3552.
- [7] P. Gallezot, “Catalytic routes from renewables to fine chemicals”, *Catal. Today* 121 (2007) 76.
- [8] C. Xu, R.A.D. Arancon, J. Labidi, R. Luque, “Lignin depolymerisation strategies: towards valuable chemicals and fuels”, *Chem. Soc. Rev.* 43 (2014) 7485.
- [9] L.P. Fernando, A.F. Stephanie, M.J. Berger, P.E. Savage, “Noncatalytic gasification of lignin in supercritical water” *Energy Fuels*, 22 (2008) 1328.
- [10] M.P. Pandey, C.S. Kim, “Lignin depolymerization and conversion: A

- review of thermochemical methods” *Chem. Eng. Technol.* 34 (2011) 29.
- [11] S. Kang, X. Li, J. Fan, J. Chang, “Hydrothermal conversion of lignin: A review”, *Renew. Sust. Energ. Rev.* 27 (2013) 546.
- [12] A.P.S. Chouhan, A.K. Sarma, “Modern heterogeneous catalysts for biodiesel production: A comprehensive review”, *Renew. Sust. Energy Rev.* 15 (2011) 4378.
- [13] M. Zabeti, W.M.A.W. Daud, M.K. Aroua, “Activity of solid catalysts for biodiesel production: A review”, *Fuel Process. Technol.* 90 (2009) 770.
- [14] M.A. Jackson, D.L. Compton, A.A. Boateng, “Screening heterogeneous catalysts for the pyrolysis of lignin”, *J. Anal. Appl. Pyrol.* 85 (2009) 226.
- [15] Y. Izumi, K. Matsuo, K. Urabe, “Efficient homogeneous acid catalysis of heteropoly acid and its characterization through ether cleavage reactions”, *J. Mol. Catal. A-Chem.* 18 (1983) 299.
- [16] M.R. Sturgeon, S. Kim, K. Lawrence, R.S. Paton, S.C. Chmely, M. Nimlos, T.D. Foust, G.T. Beckham, “A mechanistic investigation of acid-catalyzed cleavage of aryl-ether linkages: implications for lignin depolymerization in acidic environments”, *ACS Sustainable Chem. Eng.* 2 (2014) 472.
- [17] D.J. Goldsmith, E. Kennedy, R.G. Campbell, “Cleavage of cyclic ethers by magnesium bromide-acetic anhydride. SN₂ substitution at a secondary site”, *J. Org. Chem.* 40 (1975) 3571.
- [18] A. Mustafa, *The Chemistry of Heterocyclic Compounds Benzofuran*, John Wiley & Sons, New York (2009).
- [19] F. Peng, L. Zhang, H. Wang, P. Lv, H. Yu, “Sulfonated carbon nanotubes as a strong protonic acid catalyst”, *Carbon*, 43 (2005) 2405.
- [20] J. Pang, A. Wang, M. Zheng, T. Zhang, “Hydrolysis of cellulose into

- glucose over carbons sulfonated at elevated temperatures”, *Chem. Commun.*, 46 (2010) 6935.
- [21] X. Mo, D.E. López, K. Suwannakarn, Y. Liu, E. Lotero, J.G. Goodwin, C. Lu, “Activation and deactivation characteristics of sulfonated carbon catalysts”, *J. Catal.* 254 (2008) 332.
- [22] K. Hou, A. Zhang, L. Gu, M. Liu, X. Guo, “Efficient synthesis and sulfonation of ordered mesoporous carbon materials”, *J. Colloid Interface Sci.* 377 (2012) 18.
- [23] M. Zhang, A. Sun, Y. Meng, L. Wang, H. Jiang, G. Li, “High activity ordered mesoporous carbon-based solid acid catalyst for the esterification of free fatty acids”, *Micropor. Mesopor. Mat.* 204 (2015) 210.
- [24] H.W. Park, J.K. Kim, U.G. Hong, Y.J. Lee, J.H. Song, I.K. Song, “Catalytic decomposition of lignin Model compounds to aromatics over acidic catalysts”, *Catal. Surv. Asia* 17 (2013) 119.
- [25] M. Misono, “Heterogeneous catalysis by heteropoly compounds of molybdenum and tungsten”, *Catal. Rev. Sci. Eng.* 29 (1987) 269.
- [26] Y. Onoue, Y. Mizutani, S. Akiyama, Y. Izumi, “Isopropanol alcohol by direct hydration”, *ChemTech* (1978) 432.
- [27] Y. Izumi, M. Ogawa, K. Urabe, “Alkali metal salts and ammonium salts of Keggin-type heteropolyacids as solid acid catalysts for liquid-phase Friedel-Crafts reactions”, *Appl. Catal. A-Gen.* 132 (1995) 127.
- [28] S. Shikata, S.I. Nakata, T. Okuhara, M. Misono, “Catalysis by Heteropoly Compounds. 32. Synthesis of Methyl tert-Butyl Ether Catalyzed by Heteropolyacids Supported on Silica”, *J. Catal.* 166 (1997) 263.
- [29] A. Bielański, A. Lubańska, A. Micek-Ilnicka, J. Poźniczek,

- “Polyoxometalates as the catalysts for tertiary ethers MTBE and ETBE synthesis”, *Coord. Chem. Rev.* 249 (2005) 2222.
- [30] J.K. Kim, J.H. Choi, J.H. Song, I.K. Song, “Etherification of n-butanol to di-n-butyl ether over $H_nXW_{12}O_{40}$ ($X = Co^{2+}$, B^{3+} , Si^{4+} , and P^{5+}) Keggin heteropolyacid catalysts”, *Catal. Commun.* 27 (2012) 5.
- [31] I.V. Kozhevnikov, “Catalysis by heteropoly acids and multicomponent polyoxometalates in liquid-phase reactions”, *Chem. Rev.* 98 (1998) 171.
- [32] T. Okuhara, N. Mizuno, M. Misono, “Catalytic chemistry of heteropoly compounds”, *Adv. Catal.* 41 (1996) 113.
- [33] N. Yan, C. Zhao, P.J. Dyson, C. Wang, L.-T. Liu, Y. Kou, “Selective degradation of wood lignin over noble-metal catalysts in a two-step process”, *ChemSusChem*, 1 (2008) 626.
- [34] K. Yoon, A. Vannice, “Benzene hydrogenation over iron. II. Reaction model over unsupported and supported catalysts”, *J. Catal.* 82 (1983) 457.
- [35] T. Mochizuki, S-Y. Chen, M. Toba, Y. Yoshimura, “Deoxygenation of guaiacol and woody tar over reduced catalysts”, *Appl. Catal. B-Environ.* 146 (2014) 237.
- [36] R.N. Olcese, M. Bettahar, B. Malaman, J. Ghanbaja, L. Tibavizco, D. Petitjean, A. Dufour, “Gas-phase hydrodeoxygenation of guaiacol over iron-based catalysts. Effect of gases composition, iron load and supports (silica and activated carbon)”, *Appl. Catal. B-Environ.* 129 (2013) 528.
- [38] A.K. Singh, Q. Xu, “Synergistic catalysis over bimetallic alloy nanoparticles”, *ChemCatChem*, 5 (2013) 652.
- [39] J. Zhang, J. Teo, X. Chen, H. Asakura, T. Tenaka, K. Teramura, N. Yan, “A series of NiM (M = Ru, Rh, and Pd) bimetallic catalysts for effective lignin

- hydrogenolysis in water”, *ACS Catal.* 4 (2014) 1574.
- [40] J. Sun, A.M. Karim, H. Zhang, L. Kovarik, X.S. Li, A.J. Hensley, J-S. McEwen, Y. Wang, “Carbon-supported bimetallic Pd-Fe catalysts for vapor-phase hydrodeoxygenation of guaiacol”, *J. Catal.* 306 (2013) 47.
- [41] Q. Wang, H. Li, L. Chen, X. Huang, “Monodispersed hard carbon spherules with uniform nanopores” *Carbon*, 39 (2001) 2211.
- [42] J.L. Zimmerman, R. Williams, V.N. Khabashesku, J.L. Margrave, “Synthesis of spherical carbon nitride nanostructures”, *Nano Lett.* 1 (2001) 731.
- [43] M. Kruk, M. Jaroniec, T.W. Kim, R. Ryoo, “Synthesis and characterization of hexagonally ordered carbon nanopipes”, *Chem. Mater.* 15 (2003) 2815.
- [44] E.J. Zanto, S.A. Al-Muhtaseb, J.A. Ritter, “Sol–Gel-derived carbon aerogels and xerogels: design of experiments approach to materials synthesis”, *Ind. Eng. Chem. Res.* 41 (2002) 3151.
- [45] S. Che, S. Kamiya, O. Terasaki, T. Tatsumi, “The formation of cubic $Pm\bar{3}n$ mesostructure by an epitaxial phase transformation from hexagonal $p6mm$ mesophase”, *J. Am. Chem. Soc.* 123 (2001) 12089.
- [46] C.C. Ting, H.Y. Wu, S. Vetrivel, D. Saikia, Y.C. Pan, G.T.K. Fey, H.M. Kao, “A one-pot route to synthesize highly ordered mesoporous carbons and silicas through organic-inorganic self-assembly of triblock copolymer, sucrose and silica”, *Micropor. Mesopor. Mater.* 128 (2010) 1.
- [47] S. Brunauer, P.H. Emmett, E. Teller, “Adsorption of gases in multimolecular layers”, *J. Am. Chem. Soc.* 60 (1938) 309.
- [48] E.P. Barrett, L.G. Joyner, P.P. Halenda, “The determination of pore volume and area distributions in porous substances. I. Computations from nitrogen

- isotherms”, *J. Am. Chem. Soc.* 73 (1951) 373.
- [49] L. Peng, A. Philippaerts, X. Ke, J. V. Noyen, F. D. Clippel, G. V. Tendeloo, P. A. Jacobs, and B. F. Sels, “Preparation of sulfonated ordered mesoporous carbon and its use for the esterification of fatty acids”, *Catal. Today* 150 (2010) 140.
- [50] J. Janaun and N. Ellis, “Role of silica template in the preparation of sulfonated mesoporous carbon catalysts”, *Appl. Catal. A-Gen.* 394, (2011) 25.
- [51] A. Y. Bunch, X. Wang, and U. S. Ozkan, “Adsorption characteristics of reduced Mo and Ni–Mo catalysts in the hydrodeoxygenation of benzofuran”, *Appl. Catal. A-Gen.* 346, (2008) 96.
- [52] Y. Romero, F. Richard, Y. Reneme, S. Brunet, “Hydrodeoxygenation of benzofuran and its oxygenated derivatives (2,3-dihydrobenzofuran and 2-ethylphenol) over NiMoP/Al₂O₃ catalyst”, *Appl. Catal. A-Gen.* 353 (2009) 46.
- [53] R. Gao, H. Chen, Y. Le, W.L. Dai, K. Fan, “Highly active and selective Cs_{2.5}H_{0.5}PW₁₂O₄₀/SBA-15 composite material in the oxidation of cyclopentane-1,2-diol to glutaric acid by aqueous H₂O₂”, *Appl. Catal. A-Gen.* 352 (2009) 61.
- [54] S. Park, J.H. Choi, T.J. Kim, Y.M. Chung, S.H. Oh, I.K. Song, “Direct synthesis of hydrogen peroxide from hydrogen and oxygen over Pd/CsXH₃-xPW₁₂O₄₀/MCF (X = 1.7, 2.0, 2.2, 2.5, and 2.7) catalysts”, *J. Mol. Catal. A-Chem.* 353 (2012) 37.
- [55] K.H. Kang, U.G. Hong, J.O. Jun, J.H. Song, Y. Bang, J.H. Choi, S.J. Han, I.K. Song, “Hydrogenation of succinic acid to γ -butyrolactone and 1,4-

- butanediol over mesoporous rhenium-copper-carbon composite catalyst”, *J. Mol. Catal. A-Chem.* 395 (2014) 234.
- [56] Z.Q. Li, C.J. Lu, Z.P. Xia, Y. Zhou, Z. Luo, “X-ray diffraction patterns of graphite and turbostratic carbon”, *Carbon* 45 (2007) 1686.
- [57] T. Maiyalagan, A.B.A. Nassr, T.O. Alaje, M. Bron, K. Scott, “Three-dimensional cubic ordered mesoporous carbon (CMK-8) as highly efficient stable Pd electro-catalyst support for formic acid oxidation”, *J. Power Sources* 211 (2012) 147.
- [58] J. Zieliński, I. Zglinicka, L. Znak, Z. Kaszukur, “Reduction of Fe₂O₃ with hydrogen”, *Appl. Catal. A-Gen.* 381 (2010) 191.
- [59] W. Chen, Z. Fan, X. Pan, X. Bao, “Effect of confinement in carbon nanotubes on the activity of Fischer-Tropsch iron catalyst”, *J. Am. Chem. Soc.* 130 (2008) 9414.
- [60] Y. Tang, S. Cao, Y. Chen, T. Lu, Y. Zhou, L. Lu, J. Bao, “Effect of Fe state on electrocatalytic activity of Pd-Fe/C catalyst for oxygen reduction”, *Appl. Surf. Sci.* 256 (2010) 4196.
- [61] Y. Pan, F. Zhang, K. Wu, Z. Lu, Y. Chen, Y. Zhou, Y. Tang, T. Lu, “Carbon supported Palladium-Iron nanoparticles with uniform alloy structure as methanol-tolerant electrocatalyst for oxygen reduction reaction”, *Int. J. Hydrogen Energ.* 37 (2012) 2993.
- [62] N.S. Babu, N. Lingaiah, J.V. Kumar, P.S.S. Prasad, “Studies on alumina supported Pd-Fe bimetallic catalysts prepared by deposition-precipitation method for hydrodechlorination of chlorobenzene”, *Appl. Catal. A-Gen.* 367 (2009) 70.
- [63] C. Tu, S. Cheng, “Ceria-modified palladium/activated carbon as a high-

- performance catalyst for crude caprolactam hydrogenation purification”, *ACS Sustainable Chem. Eng.* 2 (2014) 629.
- [64] H. Choi, S.R. Al-Aled, S. Agarwal, D.D. Dionysiou, “Synthesis of reactive nano-Fe/Pd bimetallic system-impregnated activated carbon for the simultaneous adsorption and dechlorination of PCBs”, *Chem. Mater.* 20 (2008) 3649.
- [65] R. Burch, M.J. Hayes, “The preparation and characterization of Fe-promoted Al₂O₃-supported Rh catalysts for the selective production of ethanol from syngas”, *J. Catal.* 165 (1997) 249.
- [66] A. Guerrero-Ruiz, A. Sepúlveda-Escribano, I. Rodríguez-Ramos, “Carbon supported bimetallic catalysts containing iron. I. Preparation and characterization”, *Appl. Catal. A-Gen.* 30 (1992) 81.
- [67] A.J.R. Hensley, Y. Hong, R. Zhang, H. Zhang, J. Sun, Y. Wang, J.-S. McEwen, “Enhanced Fe₂O₃ reducibility via surface modification with Pd: characterizing the synergy within Pd/Fe catalysts for hydrodeoxygenation reactions”, *ACS Catal.* 4 (2014) 3381.
- [68] J. He, L. Lu, C. Zhao, D. Mei, J.A. Lercher, “Mechanisms of catalytic cleavage of benzyl phenyl ether in aqueous and apolar phases”, *J. Catal.* 311 (2014) 41.
- [69] J. Leveneur, G.I.N. Waterhouse, J. Kennedy, J.B. Metson, D.R.G. Mitchell, “Nucleation and growth of Fe nanoparticles in SiO₂: A TEM, XPS, and Fe L-Edge XANES investigation”, *J. Phys. Chem. C*, 115 (2011) 20978.
- [70] B. Han, C. Xu, “Nanoporous PdFe alloy as highly active and durable electrocatalyst for oxygen reduction reaction”, *Int. J. Hydrogen Energ.* 39 (2014) 18247.

- [71] J. Mao, D. Wang, G. Zhao, W. Jia, Y. Li, "Preparation of bimetallic nanocrystals by coreduction of mixed metal ions in a liquid-solid-solution synthetic system according to the electronegativity of alloy", *Cryst. Eng. Commun.* 15 (2013) 4806.
- [72] M.J. Mendes, O.A.A. Santos, E. Jordão, A.M. Silva, "Hydrogenation of oleic acid over ruthenium catalysts", *Appl. Catal. A-Gen.* 217 (2001) 253.
- [73] R. Pestman, R.M. Koster, J.A.Z. Pieterse, V. Ponc, "Reactions of carboxylic acids on oxides: 1. Selective hydrogenation of acetic acid to acetaldehyde", *J. Catal.* 168 (1997) 255.
- [74] X. Dong, H.-B. Zhang, G.-D. Lin, Y.-Z. Yuan, K.R. Yasi, "Highly active CNT-promoted Cu-ZnO-Al₂O₃ catalyst for methanol synthesis from H₂/CO/CO₂", *Catal. Lett.* 85 (2003) 237.
- [75] M. Johansson, O. Lytken, I. Chorkendorff, "The sticking probability for H₂ on some transition metals at a hydrogen pressure of 1bar", *J. Chem. Phys.* 128 (2008) 034706.
- [76] Y.C. Lin, C.L. Li, H.P. Wan, H.T. Lee, C.F. Liu, "Catalytic hydrodeoxygenation of guaiacol on Rh-based and sulfided CoMo and NiMo catalysts", *Energy Fuel* 25 (2011) 890.
- [77] D. Richard, P. Gallzot, D. Neiberker, I. Tkatcheno, "Characterization and selectivity in cinnamaldehyde hydrogenation of graphite-supported platinum catalysts prepared from a zero-valent platinum complex", *Catal. Today*, 6 (1989) 171.
- [78] A. Borgna, B.G. Anderson, A.M. Saib, H. Bluhm, M. Hävecker, A.K. Gericke, A.E.T. Kuiper, Y. Tamminga, J.W. Niemantsverdriet, "Pt-Co/SiO₂ bimetallic planar model catalysts for selective hydrogenation of

- crotonaldehyde”, *J. Phys. Chem. B* 108 (2004) 17905.
- [79] I. Matos, S. Fernandes, L. Guerreiro, S. Barata, A.M. Ramos, J. Vital, I.M. Fonseca, “The effect of surfactants on the porosity of carbon xerogels”, *Micropor. Mesopor. Mater.* 92 (2006) 38.
- [80] M. Liao, Q. Hu, J. Zheng, Y. Li, H. Zhou, C.-J. Zhong, B.H. Chen, “Pd decorated Fe/C nanocatalyst for formic acid electrooxidation”, *Electrochim. Acta* 111 (2013) 504.
- [81] W. Wang, D. Zheng, C. Du, Z. Zou, X. Zhang, B. Xia, H. Yang, D.L. Akins, “Carbon-supported Pd-Co bimetallic nanoparticles as electrocatalysts for the oxygen reduction reaction”, *J. Power Sources* 167 (2007) 243.
- [82] D. Sun, G. Zhang, X. Jiang, J. Huang, X. Jing, Y. Zheng, J. He, Q. Li, “Biogenic flower-shaped Au–Pd nanoparticles: synthesis, SERS detection and catalysis towards benzyl alcohol oxidation”, *J. Mater. Chem. A* 2 (2014) 1767.
- [83] J. Li, J. Gu, H. Li, Y. Liang, Y. Hao, X. Sun, L. Wang, “Synthesis of highly ordered Fe-containing mesoporous carbon materials using soft templating routes”, *Micropor. Mesopor. Mater.* 128 (2010) 144.
- [84] J.K. Kim, J.K. Lee, K.H. Kang, J.C. Song, I.K. Song, “Selective cleavage of C-O bond in benzyl phenyl ether to aromatics over Pd-Fe bimetallic catalyst supported on ordered mesoporous carbon”, *Appl. Catal. A-Gen.* 498 (2015) 142.
- [85] F. Pinna, M. Selva, M. Signoretto, G. Strukul, F. Boccuzzi, A. Benedetti, P. Canton, G. Fagherazzi, “Pd-Fe/SiO₂ Catalysts in the Hydrogenation of 2,4-Dinitrotoluene”, *J. Catal.* 150 (1994) 356.
- [86] A. Benedetti, G. Fagherazzi, F. Pinna, G. Rampazzo, M. Selva, G. Strukul,

- “The influence of a second metal component (Cu, Sn, Fe) on Pd/SiO₂ activity in the hydrogenation of 2,4-dinitrotoluene”, *Catal. Lett.* 10 (1991) 215.
- [87] Y. Hong, H. Zhang, J. Sun, K.M. Ayman, A.J.R. Hensley, M. Gu, M.H. Engelhard, J.-S. McEwen, Y. Wang, “Synergistic catalysis between Pd and Fe in gas phase hydrodeoxygenation of m-cresol”, *ACS Catal.* 4 (2014) 3335.
- [88] O.E. Lebedeva, W.M.H. Sachtler, “Enhanced reduction of Fe₂O₃ caused by migration of TM ions out of zeolite channels” *J. Catal.* 191 (2000) 364.
- [89] Q. Song, J. Cai, J. Zhang, W. Yu, F. Wang, J. Xu, “Hydrogenation and cleavage of the C-O bonds in the lignin model compound phenethyl phenyl ether over a nickel-based catalyst”, *Chin. J. Catal.* 34 (2013) 651.
- [90] M.W. Jarvis, J.W. Daily, H.-H. Carstensen, A.M. Dean, S. Sharma, D.C. Dayton, D.J. Robichaud, M.R. Nimlos, “Direct detection of products from the pyrolysis of 2-phenethyl phenyl ether”, *J. Phys. Chem. A* 115 (2011) 428.
- [91] H.Y. Zhao, D. Li, P. Bui, S.T. Oyama, “Hydrodeoxygenation of guaiacol as model compound for pyrolysis oil on transition metal phosphide hydroprocessing catalysts”, *Appl. Catal. A-Gen.* 391 (2011) 305.
- [92] M. Nagai, “Transition-metal nitrides for hydrotreating catalyst-Synthesis, surface properties, and reactivities” *Appl. Catal. A-Gen.* 322 (2007) 178.
- [93] M.A. Aramendía, V. Borau, C. Jiménez, J.M. Marinas, A. Porras, F.J. Ubrano, “Selective liquid-phase hydrogenation of citral over supported palladium”, *J. Catal.* 172 (1997) 46.
- [94] P.C.J. Graat, M.A.J. Somers, “Simultaneous determination of composition and thickness of thin iron-oxide films from XPS Fe 2p spectra” *Appl. Surf.*

Sci. 100–101 (1996) 36.

- [95] Z. Lui, X. Tan, J. Li, C. Lv, “Easy synthesis of bimetal PtFe-containing ordered mesoporous carbons and their use as catalysts for selective cinnamaldehyde hydrogenation”, *New J. Chem.* 37 (2013) 1350.
- [96] J.A. Rodriguez, D.W. Goodman, “The nature of the metal-metal bond in bimetallic surfaces”, *Science* 257 (1992) 897.

요 약(국문초록)

점점 고조되고 있는 환경오염 문제와 화석연료의 고갈로 인해 이러한 문제점을 해결할 수 있는 바이오매스가 신재생 에너지원으로 주목 받고 있다. 리그노섬유소 기반의 바이오매스는 1세대 바이오매스와 달리 식량자원을 기반으로 하고 있지 않기 때문에, 원료 수급이 용이하다는 장점이 있다. 2세대 바이오매스인 리그노섬유소는 셀룰로오스, 헤미셀룰로오스, 그리고 리그닌으로 구성되어있다. 현재 많은 연구들은 그 구조가 규칙적이고 간단한 셀룰로오스, 헤미셀룰로오스에 치우쳐져 있으며, 리그닌 전환에 관한 연구는 제한적이다. 리그닌은 펄프산업에서의 부산물로서 생산되며 대략 2% 만이 고분자, 시멘트, 그리고 아스팔트의 첨가제로 상업적으로 활용되고, 나머지는 대부분 저가형 연료로 연소되고 있는 실정이다. 그럼에도 불구하고, 리그닌은 다량의 방향족 구조로 이루어진 무정형 고분자로서, 연료와 화학물질의 생산에 지속 가능한 자원으로 대단한 잠재력이 있다. 리그닌의 구조를 살펴보면 다음과 같다. 다량의 방향족이 탄소-산소 혹은 탄소-산소 결합에 의해 β -O-4, α -O-4, 4-O-5, β -1, β - β , 그리고 5-5 결합을 하고 있다. 대다수가 β -O-4 (40-60%), α -O-4 (3-5%), 그리고 4-O-5 (4-7%) 결합에 의해 탄소-산소 결합을 이루고 있으며, β -1 (7-9%), β - β (2-4%), 그리고 5-5 (19-22%) 결합인 탄소-탄소 결합보다 더 많은 형태를 띤다. 그러므로 리그닌 내부의 선택적인 탄소-산소 결합의 해리는 리그닌 전환을 가능하게

하는 핵심기술로 간주되며, 리그닌 고부가가치화를 완성시킬 것으로 기대된다.

열분해, 촉매분해공정, 그리고 효소 분해 공정 등 리그닌 전환을 통해 고부가가치 화합물 생산을 위한 많은 연구가 진행되어 왔다. 그 중에서도 촉매 분해 공정은 적절한 촉매의 선택을 통해 선택적인 반응이 가능하기 때문에, 리그닌 전환공정에서 많은 관심을 받고 있다. 촉매를 통한 리그닌 분해는 일반적으로 다음과 같은 촉매계를 사용한다. 무기산, 제올라이트, 헤테로폴리산 같은 산촉매는 β -O-4, α -O-4, 그리고 β -5 결합등의 리그닌 내부의 탄소-산소 결합의 해리에 용이한 촉매로 잘 알려져 있다. 다양한 금속촉매들도 리그닌 내부의 탄소-산소 결합을 선택적으로 해리하는 촉매로 많이 연구가 되고 있다.

리그닌의 구조적 복잡성으로 인해, 리그닌 고부가가치화 연구는 보다 간단하고 분자량이 작은 몇가지 모델화합물로 추진하는 것이 유리하다. 리그닌 모델화합물은 리그닌에서 발견되는 것과 비슷한 결합을 함유하고 있어 그 반응성을 통해 리그닌 전체의 분해와 반응을 통찰할 수 있다. 특히 α -O-4, β -O-4, 그리고 β -5 결합과 같은 탄소-산 결합으로 이루어진 리그닌 이합체의 모델화합물이 일반적으로 리그닌 연구에 많이 사용된다. 본 연구에서는 다양한 모델화합물 중, 2,3-다이하이드로벤조퓨란, 벤질 페닐 에테르, 그리고 페네틸 페닐 에테르를 각각 β -5, α -O-4, 그리고 β -O-4의 모델화합물로 사용하였다.

기공성 탄소물질은 열적, 기계적 안정성으로 인해 촉매의 지지체로 많이 사용되어 왔다. 특히, 정렬된 구조의 중형기공성 탄소지지체는 균일한 기공특성, 용이한 물질전달 및 물리적특성을 조절할 수 있기에 촉매지지체로서 큰 장점이 있다. 더불어 표면의 비극성 특성으로 인해 지지체의 상호작용을 최소화하여 리그닌 분해반응에 있어 효과적이다. 이러한 특성으로 인해 정렬된 구조의 중형 기공성 탄소 지지체는 촉매 지지체로서의 큰 장점이 있다.

본 연구에서는 높은 리그닌 내부의 탄소-산소 결합의 적절한 해리를 통한 방향족생산성을 높이기 위해 정렬된 구조의 중형기공성 탄소 지지체에 담지된 팔라듐 촉매를 기반으로 촉매의 개발 및 반응실험에 적용하여 반응활성과 촉매특성간의 상관관계를 모색하였다.

우선적으로 지지체에 산점을 도입하기 위해 계면활성주형법으로 제조한 중형기공성 탄소 지지체에 술폰화 반응을 통해 술폰화 탄소지지체를 제조하였다. 이후 팔라듐 촉매를 습윤침침법을 통해 담지하고 2,3-다이하이드로벤조퓨란의 분해반응에 적용시켰다. 본 연구에서 사용한 2,3-다이하이드로벤조퓨란은 β -5를 대표하는 리그닌 모델화합물로 사용하였다. 황 함량과 촉매의 산점은 술폰화반응온도에 따라 화산형 그래프의 개형을 보인다. 또한 촉매반응의 전환율 및 방향족 수율은 제조된 촉매의 산점의 증가에 따라 증가하는 경향을 보인다. 제조된 촉매들 중에서 가장 많은 Pd/OMC-SO₃H-150 촉매가 가장 높은 반응물의 전환율 및 방향족의

수율을 보인다. 그러므로 숄폰산기가 도입된 중형기공성 탄소 지지체에 팔라듐을 담지한 촉매에서는 촉매 표면의 산점이 리그닌 분해 반응중 방향족 생산에 있어서 반응 활성을 결정하는 주요 인자라고 할 수 있다.

산특성을 증가시키기 위해, 고체산 촉매인 세슘이온이 치환된 헤테로폴리산 촉매를 중형기공성 탄소지지체에 도입하였다. 이후 팔라듐 촉매를 상기 지지체에 습윤함침법을 통해 도입하고, 2,3-다이하이드로벤조퓨란의 분해반응에 적용하였다. 상기 연구와 마찬가지로 본 연구에서 사용한 2,3-다이하이드로벤조퓨란은 β -5를 대표하는 리그닌 모델화합물로 사용하였다. 세슘이온이 치환된 헤테로폴리산 촉매의 함량에 따라 촉매의 산량이 화산형 경향성을 보이는 것을 확인하였다. 2,3-다이하이드로벤조퓨란의 전환율 및 방향족의 수율도 역시 동일한 경향성을 나타내었다. 따라서 촉매의 표면 산성도가 증가할수록 방향족의 수율이 향상되는 것을 확인할 수 있었다. 이는 숄폰산기가 도입된 중형기공성 탄소 지지체를 산성 담체로 사용한 경우와 유사한 결과이며, Pd/XC_{S2.5}H_{0.5}PW₁₂O₄₀/OMC는 촉매의 표면 산성도가 리그닌 모델화합물 내부의 탄소-산소 결합을 해리하는데 큰 역할을 한다고 할 수 있었다.

상기 산점을 포함한 이원기능촉매 (Bifunctional Catalysts)들은 리그닌 모델화합물내부의 탄소-산소 결합을 효과적으로 해리하여 분해능력을 증진시키는데 큰 효과가 있지만, 산점은 클라이센(Claissen) 재배열 및 알킬화 반응등의 부반응 또한 일으켜 차르(Char)를

형성한다. 또한 귀금속 촉매인 팔라듐 역시 온화한 조건에서의 탄소-산소 결합의 해리에 효과적인 촉매이지만, 그 촉매 자체의 특성으로 인해 방향족을 포화시켜 가스생성물의 부생성물을 생성하는 단점이 있다. Ni, Co, 그리고 Fe 등의 전이금속계열의 촉매 (Base Catalyst)는 이러한 방향족의 포화를 최소화하는 촉매로서 리그닌 분해반응에 많이 사용된다. 하지만 몇몇 연구결과들에 따르면 상기 전이금속계열의 촉매는 낮은 수소 흡착량으로 인해 전이금속촉매 홀로는 높은 방향족 수율을 얻지 못한다고 보고되고 있다. 따라서 높은 방향족 수율을 얻기 위해서 귀금속 촉매와 전이금속 촉매가 혼합된 이중금속 촉매에 대한 연구 결과들이 보고되고 있다. 이중금속 촉매는 구조 및 전자적 특성을 변화시켜 선택적인 반응을 유도할 수 있기 때문이다. 그러므로, 본 연구에서는 팔라듐 기반 촉매에 철을 첨가한 이중금속 촉매를 제조하고, 리그닌 모델화합물의 선택적인 탄소-산소 결합의 해리를 유도하였다. 더불어 그에 따른 특성 분석을 통해 촉매와 반응활성간의 특성관계를 규명하였다.

정렬된 구조의 중형기공성 탄소지지체에 담지된 팔라듐-철 이중금속 촉매는 계면활성 주형법으로 제조된 중형기공성 탄소지지체에 습윤침투법을 통해 철과 팔라듐을 담지하였다. 제조된 촉매는 리그닌 내부 결합중 α -O-4 결합을 대표하는 벤질 페닐 에테르의 분해반응에 적용하였다. 이중금속 촉매반응의 활성 비교를 위해 중형기공성 탄소 지지체에 담지된 각각의 단일 금속 팔라듐 및 철 촉매 결과도 함께 연구하였다. 본 연구에서는 두가지 금속이 혼합

되었을때의 물리·화학적 특성과 촉매반응의 활성간의 상관관계에 대해서 규명하였다. 그 결과, 중형기공성 탄소 지지체에 팔라듐이 담지된 촉매가 벤질 페닐 에테르의 가장 높은 전환율을 보이지만, 대다수의 생성물은 방향족이 포화된 탄화수소가 형성되었다. 한편, 중형기공성 탄소 지지체에 철이 담지된 촉매는 낮은 반응물의 전환을 보이지만 선택적인 탄소-산소 결합의 해리를 통해 대다수의 생성물이 방향족임을 확인하였다. 이중금속촉매는 단일금속 촉매보다 높은 방향족 수율을 보였다. 철 금속이 팔라듐에 도입됨으로써 팔라듐의 전자적인 특성이 변화되었고 그 결과로 높은 방향족 수율을 얻는 결과를 나타냈다.

추가적으로 철/팔라듐 간의 최적화된 비율을 통해 높은 방향족 수율을 얻기위해 일련의 철과 팔라듐의 몰비를 변경한 촉매를 제조하고, 리그닌 모델화합물의 분해반응에 적용하여 그 상관관계에 대해서 연구하여 보았다. 본 연구에서 사용된 리그닌 모델화합물은 리그닌 내부 결합중 β -O-4 결합을 대표하는 모델화합물인 페네틸 페닐 에테르를 사용하였다. 그 결과 촉매의 물리·화학적 특성은 이중금속 촉매상의 철과 팔라듐의 비율에 따라 크게 달라짐을 확인하였다. 특히 종전 연구에서 보였던 철을 도입함으로써 변형되는 팔라듐의 전자적 특성은 촉매 전체의 수소흡착능력 및 이중금속 촉매구조를 바꾸는 것이 확인되었다. 본 연구를 통해 페네틸 페닐 에테르의 분해반응에서 제조된 촉매의 수소 흡착능력 및 이중금속의 촉매 구조는 각각 반응물의 전환율과 선택도에 밀접한 관련이 있음을

알 수 있었다. 페네틸 페닐 에테르의 전환율은 수소흡착능력이 감소함에 따라 감소하는 경향을 보이는 반면, 높은 선택도는 이중금속 촉매상에서 $\text{Pd}_1\text{Fe}_{0.7}$ 의 조성에서 발생하는 것을 확인하였다. 본 연구를 통해 철과 팔라듐의 최적화된 비율을 확인하였으며, 그에 해당하는 $\text{Pd}_1\text{-Fe}_{0.7}/\text{OMC}$ 촉매상에서 적절한 수소흡착능력 및 최적화된 이중금속 조성을 통해 가장 높은 방향족 수율을 보임을 확인 할 수 있었다. 따라서 이중금속 촉매에서는 촉매의 수소흡착능력 및 구조가 반응 활성을 결정하는 주요 인자라고 할 수 있다.

본 연구에서는 정렬된 구조의 중형기공성 탄소 지지체에 담지된 팔라듐 기반의 이원기능 촉매 그리고 이중금속 촉매를 제조하고 리그닌 모델 화합물 내부의 탄소-산소 결합의 해리를 통해 방향족을 생산하는 연구를 수행하였다. 제조된 촉매의 리그닌 모델화합물의 분해반응에서의 활성도를 설명하기 위해 질소 흡탈착 분석 TPR, TEM, STEM-EDX, XRD, XPS, NH_3 -TPD, H_2 -TPD, 및 XPS 등의 다양한 특성 분석 기법이 수행되었다. 이원기능 촉매에서는 촉매의 산량이 리그닌 모델화합물의 분해반응에 있어서 중요한 인자임을 확인할 수 있었다. 한편, 이중금속 촉매에서는 철의 도입을 통해 팔라듐의 전자적인 특성을 변화시킬 수 있었으며, 그 결과 리그닌 모델화합물 내부의 선택적인 탄소-산소 결합의 해리를 통해 방향족 수율을 향상시킨 결과를 얻을 수 있었다.

주요어: 리그닌, 방향족, 선택적 분해, 팔라듐 촉매,
헤테로폴리산, 이원기능 촉매, 전자구조, 이중금속 촉매,

학 번: 2011-21024

List of publications

Papers

International papers published (First author)

1. **J.K. Kim**, J.K. Lee, K.H. Kang, J.W. Lee, I.K. Song, "Catalytic Decomposition of Phenethyl Phenyl Ether to Aromatics over Pd-Fe Bimetallic Catalysts Supported on Ordered Mesoporous Carbon", *Journal of Molecular Catalysis A: Chemical*, 410, pp.184-192 (2015).
2. **J.K. Kim**, J.K. Lee, K.H. Kang, J.C. Song, I.K. Song, "Selective Cleavage of C-O Bond in Benzyl Phenyl Ether to Aromatics over Pd-Fe Bimetallic Catalyst Supported on Ordered Mesoporous Carbon", *Applied Catalysis A: General*, 498, pp.142-149 (2015).
3. **J.K. Kim**, H.W. Park, U.G. Hong, Y.J. Lee, I.K. Song, "Catalytic Decomposition of 2,3-Dihydrobenzofuran to Monocyclic Compounds over Palladium Catalysts Supported on Sulfonated Ordered Mesoporous Carbon", *Journal of Nanoscience and Nanotechnology*, 15(11), pp.9139-9144 (2015).
4. **J.K. Kim**, H.W. Park, U.G. Hong, J.H. Choi, I.K. Song, " $\text{Cs}_x\text{H}_{3.0-x}\text{PW}_{12}\text{O}_{40}$ (X=2.0-3.0) Heteropolyacid Nano-catalysts for Catalytic Decomposition of 2,3-Dihydrobenzofuran to Aromatics", *Journal of Nanoscience and Nanotechnology*, 14(11), pp.8884-8890 (2014).
5. **J.K. Kim**, H.W. Park, U.G. Hong, Y.J. Lee, J.H. Song, I.K. Song, "Catalytic Decomposition of 2,3-Dihydrobenzofuran to Monomeric Cyclic Compounds over Pd/XCs_{2.5}H_{0.5}PW₁₂O₄₀/OMC (Ordered Mesoporous Carbon) (X=10-30 wt%) Catalysts", *Catalysis Communications*, 49, pp.68-72 (2014).

6. **J.K. Kim**, J.H. Choi, D.R. Park, I.K. Song, “Etherification of n-Butanol to Di-n-butyl Ether over Keggin-, Wells-Dawson-, and Preyssler-type Heteropolyacid Catalysts”, *Journal of Nanoscience and Nanotechnology*, 13(12), pp.8121-8126 (2013).
7. **J.K. Kim**, J.H. Choi, J.H. Song, J. Yi, I.K. Song, “Etherification of n-Butanol to Di-n-butyl Ether over $H_nXW_{12}O_{40}$ ($X = Co^{2+}$, B^{3+} , Si^{4+} , and P^{5+}) Keggin Heteropolyacid Catalysts”, *Catalysis Communications*, 27, pp.5-8 (2012).

International papers published (Co-author)

1. J.K. Lee, H. Seo, **J.K. Kim**, H. Seo, H.-R. Cho, J. Lee, H. Chang, I.K. Song, “Direct Dehydrogenation of n-Butane over Pt/Sn/Zn-K/ Al_2O_3 Catalyst: Effect of Hydrogen in the Feed”, *Journal of Nanoscience and Nanotechnology* (In Press).
2. J.-Y. Kim, J.H. Lee, J. Park, **J.K. Kim**, D. Ahn, I.K. Song, J.W. Choi, “Catalytic Pyrolysis of Lignin over HZSM-5 Catalysts: Effect of Various Parameters in the Production of Aromatic Hydrocarbon”, *Journal of Analytical and Applied Pyrolysis*, 114, pp.273-280 (2015).
3. E.J. Lee, Y.J. Lee, **J.K. Kim**, M. Lee, J. Yi, J.R. Yoon, J.C. Song, I.K. Song, “Oxygen Group-containing Activated Carbon Aerogel as an Electrode Material for Supercapacitor”, *Materials Research Bulletin*, 70, pp.209-214 (2015).
4. E.J. Lee, Y.J. Lee, **J.K. Kim**, U.G. Hong, J. Yi, J.R. Yoon, I.K. Song, “ CO_2 Activated Carbon Aerogel with Enhanced Electrochemical Performance as a Supercapacitor Electrode Material”, *Journal of Nanoscience and Nanotechnology*, 15(11), pp.8917-8921 (2015).
5. J.-Y. Kim, J. Park, H. Hwang, **J.K. Kim**, I.K. Song, J.W. Choi, “Catalytic

Depolymerization of Lignin Macromolecule to Alkylated Phenols over Various Metal Catalysts in Supercritical tert-Butanol”, *Journal of Analytical and Applied Pyrolysis*, 113, pp.99-106 (2015).

6. K.H. Kang, U.G. Hong, Y. Bang, J.H. Choi, **J.K. Kim**, J.K. Lee, S.J. Han, I.K. Song, “Hydrogenation of Succinic Acid to 1,4-Butanediol over Re-Ru Bimetallic Catalysts Supported on Mesoporous Carbon”, *Applied Catalysis A: General*, 490, pp.153-162 (2015).
7. U.G. Hong, **J.K. Kim**, J. Lee, J.K. Lee, J. Yi, I.K. Song, “Conversion of Succinic Acid to 1,4-Butanediol via Dimethyl Succinate over Rhenium Nano-catalyst Supported on Copper-containing Mesoporous Carbon”, *Journal of Nanoscience and Nanotechnology*, 14(11), pp.8867-8872 (2014).
8. U.G. Hong, **J.K. Kim**, J. Lee, J.K. Lee, J.H. Song, J. Yi, I.K. Song, “Hydrogenation of Succinic Acid to Tetrahydrofuran over Ruthenium-carbon Composite Catalysts: Effect of HCl Concentration in the Preparation of the Catalysts”, *Journal of Industrial and Engineering Chemistry*, 20(5), pp.3834-3840 (2014).
9. U.G. Hong, **J.K. Kim**, J. Lee, J.K. Lee, J.H. Song, J. Yi, I.K. Song, “Hydrogenation of Succinic Acid to Tetrahydrofuran (THF) over Ruthenium-carbon Composite (Ru-C) Catalyst”, *Applied Catalysis A: General*, 469, pp.466-471 (2014).
10. H.W. Park, **J.K. Kim**, U.G. Hong, Y.J. Lee, J.H. Song, I.K. Song, “Catalytic Decomposition of Lignin Model Compounds to Aromatics over Acidic Catalysts”, *Catalysis Surveys from Asia*, 17, pp.119-131 (2013).
11. H.W. Park, **J.K. Kim**, U.G. Hong, Y.J. Lee, J.H. Choi, Y. Bang, I.K. Song, “Catalytic Decomposition of 1,3-Diphenoxybenzene to Monomeric Cyclic Compounds over Palladium Catalysts Supported on Acidic Activated Carbon

Aerogels”, *Applied Catalysis A: General*, 456, pp.59-66 (2013).

12. J.H. Choi, **J.K. Kim**, D.R. Park, T.H. Kang, J.H. Song, I.K. Song, “Redox Properties and Oxidation Catalysis of Transition Metal-substituted α - $K_5PW_{11}O_{39}(M^?OH_2)$ ($M = Mn^{II}, Co^{II}, Ni^{II},$ and Zn^{II}) Keggin Heteropolyacid Catalysts for Liquid-phase Oxidation of 2-Propanol”, *Journal of Molecular Catalysis A: Chemical*, 371, pp.111-117 (2013).
13. H.W. Park, **J.K. Kim**, U.G. Hong, Y.J. Lee, J.H. Song, I.K. Song, “Catalytic Decomposition of 4-Phenoxyphenol over Pd/XC_{S2.5}H_{0.5}PW₁₂O₄₀/ACA (Activated Carbon Aerogel)-SO₃H (X=10-30 wt%) Catalysts”, *Applied Catalysis A: General*, 453, pp.287-294 (2013).
14. J.H. Choi, **J.K. Kim**, S. Park, J.H. Song, I.K. Song, “Redox Properties and Oxidation Catalysis of Potassium Salts of Transition Metal-substituted α_2 - $K_8P_2W_{17}O_{61}(M\cdot OH_2)$ ($M = Mn^{II}, Zn^{II}, Fe^{II}, Co^{II}, Cu^{II},$ and Ni^{II}) Wells-Dawson Heteropolyacids”, *Applied Catalysis A: General*, 427-428, pp.79-84 (2012).
15. J.H. Choi, **J.K. Kim**, D.R. Park, S. Park, J. Yi, I.K. Song, “Etherification of n-Butanol to Di-n-butyl Ether over $H_3PMo_{12-x}W_xO_{40}$ ($x=0, 3, 6, 9, 12$) Keggin and $H_6P_2Mo_{18-x}W_xO_{62}$ ($x=0, 3, 9, 15, 18$) Wells-Dawson Heteropolyacid Catalysts”, *Catalysis Communications*, 14(1), pp.48-51 (2011).

Domestic papers published (First-author)

1. 김정권, **최정호**, 이종협, 송인규, “Keggin형 $H_{3+x}PW_{12-x}Nb_xO_{40}$ ($x=0, 1, 2, 3$) 및 Wells-Dawson형 $H_{6+x}P_2W_{18-x}Nb_xO_{62}$ ($x=0, 1, 2, 3$) 헤테로폴리산 촉매를 이용한 n-Butanol로부터 Di-n-Butyl Ether의 제조”, *화학공학*, 50(2), pp.251-256 (2012).

Patents

Registered patents

1. 송인규, 김정권, 홍웅기, 강기혁, 이종권, “술폰산기 (-SO₃H) 가 도입된 산점을 포함한 정렬된 구조의 중형기공성탄소에 담지된 귀금속 촉매, 그 제조방법 및 상기 촉매를 이용한 리그닌 모델 화합물 분해 방법”, 대한민국특허 제 1,536,623호 (2015).
2. 송인규, 김정권, 홍웅기, 최정호, “중형기공성 탄소에 담지된 양이온 치환 헥테로폴리산 및 귀금속 담지촉매, 그 제조방법 및 상기 촉매를 이용한 리그닌 화합물 분해 방법”, 대한민국 특허출원 10-2013-0128048 (2013), 대한민국특허 제 1,466,882호 (2014).

Applied patents

1. 조혜란, 서한욱, 이진석, 장호식, 송인규, 이종권, 서현, 김정권, “다양한 결정상을 갖는 노르말-부탄의 탈수소화 반응 촉매용 알루미늄 담체의 제조방법, 그에 의해 제조된 알루미늄 담체에 담지된 주석을 포함하는 백금 촉매 및 상기 촉매를 이용한 노르말-부텐과 1,3-부타디엔 제조방법”, 대한민국 특허출원 10-2014-0095885 (2014).
2. 송인규, 이종협, 홍웅기, 김정권, 이종권, “중형 기공성 탄소에 담지된 귀금속 담지촉매, 그 제조방법 및 상기 촉매를 이용하여 숙신산으로부터 사수소화퓨란을 제조하는 방법”, 대한민국 특허출원 10-2014-0064910 (2014).
3. 송인규, 김정권, 홍웅기, 강기혁, 이종권, “술폰산기 (-SO₃H) 가 도입된 산점을 포함한 정렬된 구조의 중형기공성탄소에 담지된 귀금속 촉매,

그 제조방법 및 상기 촉매를 이용한 리그닌 모델 화합물 분해 방법”,
대한민국 특허출원 10-2014-0057290 (2014).

4. 송인규, 김정권, 홍웅기, 최정호, “중형기공성 탄소에 담지된 양이온 치환 헥테로폴리산 및 귀금속 담지촉매, 그 제조방법 및 상기 촉매를 이용한 리그닌 화합물 분해 방법”, 대한민국 특허출원 10-2013-0128048 (2013).
5. 송인규, 박해웅, 김정권, 홍웅기, 이윤재, “양이온 치환 헥테로폴리산이 함침된 술폰산 포함 활성 카본에어로젤에 담지된 귀금속 촉매 및 상기 촉매를 이용한 리그닌 화합물 분해 방법”, 대한민국 특허출원 10-2012-0130314 (2012).

Conferences

International conferences (First author)

1. **J.K. Kim**, K.H. Kang, J.K. Lee, J.W. Lee, I.K. Song, "Catalytic Decomposition of Phenethyl Phenyl Ether to Aromatics over Pd-Fe Bimetallic Catalysts Supported on Ordered Mesoporous Carbon", *NANO KOREA 2015*, P1506_104, COEX, Seoul, Korea (2015/7/1-3).
2. **J.K. Kim**, J.H. Choi, D.R. Park, I.K. Song, "Etherification of n-Butanol to Di-n-butyl Ether over Heteroatom-substituted Keggin Heteropolyacid Catalysts", *The 14th Korea-Japan Symposium on Catalysis*, GP09, Nagoya, Japan (2013/7/1-3).
3. **J.K. Kim**, H.W. Park, U.G. Hong, J.H. Choi, I.K. Song, " $\text{Cs}_x\text{H}_{3.0-x}\text{PW}_{12}\text{O}_{40}$ (X=2.0-3.0) Heteropolyacid Nano-catalysts for Catalytic Decomposition of 2,3-Dihydrobenzofuran to Aromatics", *NANO Korea 2013 Symposium*, P1303_009, Coex, Seoul, Korea (2013/7/10-12).
4. **J.K. Kim**, J.H. Choi, D.R. Park, J. Yi, I.K. Song, "Etherification of n-Butanol to Di-n-butyl Ether over Heteropolyacid Catalysts with Different Structure", *The 10th NANO KOREA 2012 Symposium*, P1208_022, COEX, Korea (2012/8/16-18).

International conferences (Co-author)

1. J.W. Lee, **J.K. Kim**, T.H. Kang, I.K. Song, "Direct Synthesis of Hydrogen Peroxide from Hydrogen and Oxygen over Shape-controlled Palladium Catalysts", *NANO KOREA 2015*, P1506_124, COEX, Seoul, Korea (2015/7/1-3).
2. J.K. Lee, **J.K. Kim**, K.H. Kang, I.K. Song, "Direct Dehydrogenation of n-Butane over Platinum-tin Catalysts Supported on Alumina", *NANO KOREA*

2015, P1503_099, COEX, Seoul, Korea (2015/7/1-3).

3. E.J. Lee, Y.J. Lee, **J.K. Kim**, M. Lee, J. Yi, J.R. Yoon, I.K. Song, "Preparation and Characterization of Nitrogen-enriched Carbon Aerogel as a Supercapacitor Electrode Material", *NANO KOREA 2015*, P1503_100, COEX, Seoul, Korea (2015/7/1-3).
4. K.H. Kang, **J.K. Kim**, J.K. Lee, S.J. Han, I.K. Song, "Re-Ru Bimetallic Catalysts for Hydrogenation of Succinic Acid to 1,4-Butanediol", *The 15th Korea-Japan Symposium on Catalysis*, GP59, Busan, Korea (2015/05/26-28).
5. E.J. Lee, Y.J. Lee, **J.K. Kim**, U.G. Hong, J. Yi, J.R. Yoon, I.K. Song, "CO₂ Activated Carbon Aerogel with Enhanced Electrochemical Performance as a Supercapacitor Electrode Material", *NANO KOREA 2014*, P1406_003, COEX, Seoul, Korea (2014/7/2-4).
6. J.H. Choi, **J.K. Kim**, S. Park, I.K. Song, "Redox Properties of Potassium Salts of Transition Metal-substituted Wells-Dawson Heteropolyacids Probed by Scanning Tunneling Microscopy", *The 10th NANO KOREA 2012 Symposium*, P1202_007, COEX, Korea (2012/8/16-18).
7. J.H. Choi, D.R. Park, S. Park, **J.K. Kim**, I.K. Song, "Scanning Tunneling Microscopy and Tunneling Spectroscopy Study of H₆P₂Mo_xW_{18-x}O₆₂ (x=0, 3, 9, 15, 18) Wells-Dawson Heteropolyacids", *The 15th International Congress on Catalysis*, 6608, Munich, Germany (2012/07/1-7).

Domestic conferences (First author)

1. 김정권, 이종권, 강기혁, 이종원, 송인규, “중형기공성 탄소에 담지된 Pd-Fe 촉매를 통한 리그닌 내부의 선택적인 탄소-산소 분해반응 및 리그닌 모델 화합물의 분해경로 규명”, 2015년 한국화학공학회 추계학술회의, O촉매D목-2, 일산 KINTEX (2015/10/21-23).
2. 김정권, 강기혁, 이종권, 송인규, “전이금속 복합 촉매상에서 리그닌 내부의 선택적인 탄소-산소 분해반응을 통한방향족 생성 및 리그닌 모델 화합물의 분해경로 규명”, 2015년 한국화학공학회 춘계학술회의, P촉매목-7, 제주 ICC (2015/4/22-24).
3. 김정권, 박해웅, 이종권, 이어진, 송인규, “전이금속 및 귀금속이 담지된 중형기공성 탄소 담체를 이용한 리그닌 모델화합물의 분해반응 및 분해경로 규명”, 2014년 한국화학공학회 추계학술회의, P촉매금-9, 대전 DCC (2014/10/22-24).
4. 김정권, 박해웅, 홍웅기, 이윤재, 송인규, “리그닌 모델화합물의 분해반응에서 숄폰기가 도입된 중형기공탄소 담체에 담지된 금속 촉매의 반응활성”, 2014년 한국공업화학회 춘계학술회의, 1P-258, 제주 ICC (2014/4/30-5/2).
5. 김정권, 박해웅, 홍웅기, 이윤재, 송인규, “숄폰산이 도입된 중형기공성탄소에 담지된 금속촉매를 이용한 리그닌 모델화합물 분해반응”, 2014년 한국화학공학회 춘계학술회의, P촉매금-52, 창원 컨벤션센터 (2014/4/23-25).
6. 김정권, 박해웅, 홍웅기, 송인규, “리그닌의 분해반응에서 균일한 기공구조를 갖는 중형기공 탄소 담체에 담지된 고체산 및 금속 촉매의

반응활성”, 2013년 한국공업화학회 추계학술회의, 2P-176, 대전 컨벤션센터 (2013/10/30-11/1).

7. 김정권, 박해웅, 홍웅기, 송인규, “직접합성법에 의해 제조된 중형기공탄소에 담지된 고체산 및 금속촉매를 이용한 리그닌 모델화합물 분해반응”, 2013년 한국화학공학회 추계학술회의, P촉매목-4, 대구 EXCO (2013/10/23-25).
8. 김정권, 홍웅기, 최정호, 송인규, “ $C_{5x}H_{3.0-x}PW_{12}O_{40}$ ($X=2.0-3.0$) 헤테로폴리산 촉매를 이용한 리그닌 모델화합물로부터 방향족 생성에 관한 연구”, 2013년 한국공업화학회 춘계학술회의, 1P-442, 제주 국제컨벤션센터 (2013/5/1-3).
9. 김정권, 홍웅기, 최정호, 송인규, “양이온이 치환된 헤테로폴리산 촉매를 이용한 리그닌 모델 화합물 분해”, 2013년 한국화학공학회 춘계학술회의, P촉매금-4, 광주 김대중컨벤션센터 (2013/4/24-26).
10. 김정권, 최정호, 박동률, 송인규, “헤테로폴리산 촉매를 이용한 n-butanol의 탈수화반응을 통한 di-n-butyl ether의 합성”, 2012년 한국공업화학회 추계학술회의, 2P-184, 대전컨벤션센터 (2012/10/31-11/2).
11. 김정권, 최정호, 박동률, 송인규, “다양한 구조의 헤테로폴리산을 이용한 Di-n-Butyl Ether의 합성에 관한 연구”, 2012년 한국화학공학회 추계학술회의, P촉매수-8, 부산 BEXCO (2012/10/24-26).
12. 김정권, 최정호, 이종협, 송인규, “Keggin형 헤테로폴리산 $H_8-nX^{n+}W_{12}O_{40}$ ($X^{n+}=Co^{2+}, B^{3+}, Si^{4+},$ and P^{5+})를 이용한 butanol로부터 di-n-butyl ether의 탈수화 반응”, 2012년 한국공업화학회 춘계학술회의, 2P-167,

김대중컨벤션센터 (2012/5/9-11).

13. 김정권, 최정호, 이종협, 송인규, “중심원소가 치환된 Keggin형 헤테로폴리산을 이용한 di-n-butyl ether의 합성에 관한 연구”, 2012년 한국화학공학회 춘계학술회의, P축매금-28, 제주ICC (2012/4/25-27).
14. 김정권, 최정호, 이종협, 송인규, “헤테로폴리산 촉매를 이용한 n-butanol로부터 di-n-butyl ether 합성에 관한 연구”, 2011년 한국공업화학회 추계학술회의, 1P-266, 경원대학교 (2011/11/2-4).
15. 김정권, 최정호, 이종협, 송인규, “전이금속이 배워된 헤테로폴리산 촉매를 이용한 di-n-butyl ether 합성에 관한 연구”, 2011년 한국화학공학회 추계학술회의, P축매목-13, 송도컨벤시아 (2011/10/26-28).

Domestic conferences (Co-author)

1. 이종원, 김정권, 강태훈, 송인규, “팔라듐 나노입자의 미세구조 조절이 과산화수소 직접 합성 반응에 미치는 영향에 대한 연구”, 2015년 한국화학공학회 추계학술회의, P축매금-13, 일산 KINTEX (2015/10/21-23).
2. 이종권, 김정권, 강기혁, 이진석, 장호식, 송인규, “노르말-부탄의 직접 탈수소화 반응에서 소성온도가 다른 알루미늄에 담지된 백금-주석 촉매가 노르말-부텐과 1,3-부타디엔 생성에 미치는 영향”, 2015년 한국화학공학회 춘계학술회의, P축매목-2, 제주 ICC (2015/4/22-24).
3. 강기혁, 김정권, 이종권, 한승주, 김태협, 송인규, “레늄-루세늄 이중금속 촉매 상에서 숙신산의 수소화를 통한 1,4-부탄디올의 제조”, 2015년 한국화학공학회 춘계학술회의, P축매목-6, 제주 ICC (2015/4/22-24).

4. 이어진, 이윤재, 김정권, 윤중락, 이종협, 송인규, “멜라민을 이용한 슈퍼커패시터 전극용 질소 도핑 카본 에어로젤의 제조에서 카본 표면에 도입된 질소 원자와 커패시턴스의 관계 고찰”, 2015년 한국화학공학회 춘계학술회의, P축매목-8, 제주 ICC (2015/4/22-24).
5. 이종원, 김정권, 강태훈, 송인규, “촉매의 미세구조 및 산특성 조절이 과산화수소 직접 합성 반응에 미치는 영향에 대한 연구”, 2015년 한국화학공학회 춘계학술회의, P축매목-9, 제주 ICC (2015/4/22-24).
6. 이종권, 김정권, 서한욱, 조혜란, 이진석, 장호식, 송인규, “알루미나 담체에 담지된 백금-주석 촉매의 제조 및 이를 활용한 노르말-부탄의 직접 탈수소화 반응을 통한 부텐과 부타디엔 생성”, 2014년 한국화학공학회 추계학술회의, P축매금-3, 대전 DCC (2014/10/22-24).
7. 이어진, 이윤재, 김정권, 윤중락, 송인규, “카본 에어로젤의 표면 개질반응을 통한 슈퍼커패시터 전극용 활성 카본 에어로젤의 제조에서 카본 표면에 도입된 기능기와 커패시턴스의 관계 고찰”, 2014년 한국화학공학회 추계학술회의, P축매금-10, 대전 DCC (2014/10/22-24).
8. 이윤재, 이어진, 김정권, 홍용기, 이종협, 윤중락, 송인규, “PEI(polyethyleneimine) 처리된 산화 그래핀을 사용하여 제조된 카본 에어로젤-그래핀 화합물의 합성 및 슈퍼커패시터 전극으로 응용: PEI 처리된 산화 그래핀의 양이 전기화학적 물성에 미치는 영향”, 2014년 한국공업화학회 춘계학술회의, 1P-261, 제주 ICC (2014/4/30-5/2).
9. 홍용기, 강기혁, 김정권, 이종원, 이종권, 이종협, 송인규, “염산을 조절한 단일공정 계면활성-주형법으로 제조된 귀금속-탄소 복합체 촉매의 숙신산 수소화 반응활성”, 2014년 한국공업화학회

춘계학술회의, 1P-266, 제주 ICC (2014/4/30-5/2).

10. 이윤재, 이어진, 김정권, 홍웅기, 이종협, 윤중락, 송인규, “화학적 활성화법을 이용하여 제조된 활성 카본 에어로젤-그래핀 화합물의 물리화학적 특성 및 슈퍼커패시터 전극으로서의 전기화학적 특성에 관한 연구”, 2014년 한국화학공학회 춘계학술회의, P축매금-91, 창원 컨벤션센터 (2014/4/23-25).
11. 홍웅기, 강기혁, 김정권, 이중원, 이종권, 이종협, 송인규, “숙신산으로부터 사수소화퓨란 생성 반응에서 촉매 표면 형태에 따른 루테튬-탄소 복합체 촉매의 반응 활성”, 2014년 한국화학공학회 춘계학술회의, P축매금-53, 창원 컨벤션센터 (2014/4/23-25).
12. 홍웅기, 김정권, 이중원, 이종권, 이종협, 송인규, “단일공정 계면활성 주형법으로 제조된 루테튬-탄소 복합체 촉매의 숙신산 수소화 반응활성”, 2013년 한국공업화학회 추계학술회의, 2P-254, 대전 컨벤션센터 (2013/10/30-11/1).
13. 홍웅기, 김정권, 이중원, 이종권, 이종협, 송인규, “숙신산으로부터 사수소화퓨란 생성 반응에서 귀금속-지지체 결합 온도에 따른 루테튬-탄소 복합체 촉매의 반응 활성”, 2013년 한국화학공학회 추계학술회의, P축매목-1, 대구 EXCO (2013/10/23-25).
14. 홍웅기, 김정권, 이중원, 이종권, 이종협, 송인규, “구리를 포함한 중형기공 탄소담체에 담지된 레늄 담지촉매를 이용한 숙신산의 수소화 반응에서 구리의 포함량에 따른 반응 활성”, 2013년 한국공업화학회 춘계학술회의, 1P-414, 제주 국제컨벤션센터 (2013/5/1-3).
15. 홍웅기, 김정권, 이중원, 이종권, 이종협, 송인규, “레늄-구리 촉매를

이용하여 숙신산으로부터 디메틸숙시네이트를 통해 1,4-부탄디올을 생산하는 촉매공정에서 구리 비율에 따른 반응 활성”, 2013년 한국화학공학회 춘계학술회의, P촉매금-2, 광주 김대중컨벤션센터 (2013/4/24-26).

16. 최정호, 김정권, 박동률, 송인규, “STM 분석을 통한 Keggin형 $H_4PW_{11}M_1O_{40}$ 및 Wells-Dawson형 $H_7P_2W_{17}M_1O_{62}$ ($M=Nb, Ta$) 헤테로폴리산의 산화환원 특성연구”, 2012년 한국공업화학회 추계학술회의, 2P-181, 대전컨벤션센터 (2012/10/31-11/2).
17. 최정호, 김정권, 박동률, 송인규, “5족 전이금속(Nb, Ta)이 단일 치환된 Keggin형 및 Wells-Dawson형 헤테로폴리산의 STM 연구”, 2012년 한국화학공학회 추계학술회의, P촉매수-9, 부산 BEXCO (2012/10/24-26).
18. 최정호, 송인규, 김정권, 박선영, “4주기 전이금속이 단일 치환된 Wells-Dawson형 헤테로폴리산의 STM 연구”, 2012년 한국공업화학회 춘계학술회의, 2P-200, 김대중컨벤션센터 (2012/5/9-11).
19. 최정호, 송인규, 김정권, 박선영, “STM 분석을 통한 Wells-Dawson형 $K_8P_2W_{17}O_{61}(M-OH_2)$ ($M=Mn^{II}, Fe^{II}, Co^{II}, Ni^{II}, Cu^{II}, \text{ and } Zn^{II}$) 헤테로폴리산의 산화환원 특성연구”, 2012년 한국화학공학회 춘계학술회의, P촉매금-27, 제주ICC (2012/4/25-27).
20. 최정호, 박동률, 김정권, 송인규, “STM 분석을 통한 니오븀이 배워된 Keggin형 헤테로폴리산의 산화환원 특성연구”, 2011년 한국공업화학회 추계학술회의, 1P-261, 경원대학교 (2011/11/2-4).
21. 최정호, 박동률, 김정권, 송인규, “니오븀이 배워된 $H_{6+x}P_2W_{18-x}Nb_xO_{62}$ Wells-Dawson형 헤테로폴리산의 STM 연구”, 2011년

한국화학공학회 추계학술회의, P축매목-10, 송도컨벤시아 (2011/10/26-28).

22. 이증원, 송인규, 황선환, 홍웅기, 김정권, 윤민혜, “C5 유분의 분해 반응을 통한 경질 올레핀 제조에서 ZSM-5 촉매의 Si/Al 비가 반응활성에 미치는 영향”, 2011년 한국화학공학회 춘계학술회의, P축매목-5, 창원컨벤션센터 (2011/4/27-29).

